THE UNIVERSITY *of* EDINBURGH

This thesis has been submitted in fulfilment of the requirements for a postgraduate degree (e.g. PhD, MPhil, DClinPsychol) at the University of Edinburgh. Please note the following terms and conditions of use:

This work is protected by copyright and other intellectual property rights, which are retained by the thesis author, unless otherwise stated.
A copy can be downloaded for personal non-commercial research or study, without prior permission or charge.
This thesis cannot be reproduced or quoted extensively from without first obtaining permission in writing from the author.
The content must not be changed in any way or sold commercially in any format or medium without the formal permission of the author.
When referring to this work, full bibliographic details including the author, title, awarding institution and date of the thesis must be given.

Experimental and Theoretical Studies of Electronic and Mechanical Properties of two-dimensional (2D) WSe_2

Rui Zhang

A thesis submitted for the degree of Doctor of Philosophy.

The University of Edinburgh

2018

Abstract

Two-dimensional (2D) transition metal dichalcogenides (TMDs) with intrinsic band gaps are considered to be prospective alternatives for graphene in the applications of emerging nano-semiconductor devices. As a significant member of the TMDs family, WSe_2 with superior optical properties attracts increasing attention, especially in the optoelectronics. In this thesis, the electronic and mechanical properties of 2D WSe_2 have been studied experimentally and theoretically. Firstly, the fabrication of substrate-supported and suspended pre-patterned WSe_2 FETs with the low-cost optical lithography and vapour HF etching technology have been realised. The subsequent electrical measurement of the fabricated WSe_2 FETs indicates that the WSe_2/dielectric interface can affect the electrical performance of 2D WSe_2 negatively. To gain more insights on the impact of field-effect on 2D WSe_2, first-principle calculations have been conducted in this research to study the evolutions of the crystal structure, electronic band structure, conductive channel size, and electrical transport property of WSe_2 under various levels of field-effect. Furthermore, a layer thinning and chemical doping method of 2D WSe_2 by vapour XeF_2 exposure featured with good air-stability, scalability, and controllability has been developed to enable the layer engineering of 2D WSe_2 and integration of 2D WSe_2 to logic circuits, solar cells, and light-emitting diodes (LED). The thinning and doping mechanism has been investigated with a combination of Raman spectroscopy, photoluminescence (PL) spectroscopy, and X-ray photoelectron spectroscopy (XPS) characterization techniques. Afterwards, the in-plane elastic properties (including the Young's modulus, breaking strain, and etc.) of 2D WSe_2 have been measured with nanoindentation experiments implemented by atomic force microscopy (AFM). The results prove the suitability of 2D WSe_2 in the applications of flexible devices and nanoelectromechanical systems (NEMS) operating in the audio resonance frequency, such as acoustic sensors and loudspeakers. To provide a comprehensive understanding of the strain engineering of 2D WSe_2, the strain induced variations of the crystal structure, electronic band structure, and electrical transport property of 2D WSe_2 have been further studied with first-principle calculations, which paves the way for the performance tuning of 2D WSe_2 devices via strain and applications of 2D WSe_2 in strain sensors.

Lay summary

Two-dimensional (2D) transition metal dichalcogenides (TMDs) with intrinsic band gaps are prospective alternatives for graphene in the applications of emerging nano-semiconductor devices, which has attracted tremendous attention recently. In this work, some fundamental studies have been conducted on 2D WSe_2 being a significant member of the TMDs family. Firstly, the impact of the field-effect on 2D WSe_2 has been investigated with electrical measurements of the WSe_2-based field-effect transistors (FETs) together with first-principle calculations. The calculation results predict that novel gate-controlled spintronics and nanogenerators could be built from 2D WSe_2. Then a chemical doping method of 2D WSe_2 with good air stability and controllability has been developed, which enables the future applications of 2D WSe_2 in complex logic circuits, solar cells, and light-emitting diodes (LEDs). Afterwards, the in-plane elastic properties of 2D WSe_2 have been measured experimentally. The results show that 2D WSe_2 is more suitable for building flexible devices and acoustic sensors/loudspeakers, due to its lower Young's modulus compared to other 2D materials. At last, first-principle calculations have been performed to study the influence of strain on the electronic property of 2D WSe_2 aiming to pave the way for the future application of 2D WSe_2-based strain sensor.

Acknowledgement

First of all, I would like to thank my primary supervisor Professor Rebecca Cheung for her guidance through my whole doctoral programme. Her great passion for scientific research always inspires me to keep pursuing further goals in my PhD study. I will always be grateful for the in-depth knowledge she has provided for me. Also, I would like to thank my secondary supervisor Professor Vasileios Koutsos for sharing his research experience and providing me with valuable feedbacks to advance my work. My acknowledge to Dr Enrico Mastropaolo for introducing the Scottish Microelectronics Centre (SMC) cleanroom to me and his efforts on reviewing my experimental workflows.

My sincere gratitude goes to Dr Andrew Bunting, Dr Camelia Dunare, and Dr Peter Lomax who have given me the training and advice on using the facilities in the cleanroom safely and efficiently. I also would like to thank the technical staffs in the SMC cleanroom, Mr Richard Blair, Mr Stewart Ramsay, Mr Ewan Macdonald, and Mr Brian Neilson (retired) for their responsibility, patience, and tolerance in solving plenty of issues I met and created in the cleanroom. I had the great opportunity to collaborate with the MEMSSTAR Ltd. My deeply gratitude goes to Dr Daniel Drysdale for offering me technological supports for using their vapour XeF_2 and HF etching systems. I also would like to thank Dr Andrey Gromov and Dr Oleg Nerushev for their assistance in setting up the Raman/PL spectroscopy and Dr Ron Brown for enabling me to conduct the XPS measurements. Also, I want to thank Atif Syed and Asaad Al-mashaal who have demonstrated the operations of atomic force microscope (AFM) and laser Doppler vibrometer (LDV) to me. Also, my appreciation goes to my 3-year officemates, Asaad Al-mashaal, Chandrasekaran Gunasekaran, Hanning Mai, Nadira Jamil for bringing fun and happiness to the office constantly.

Last but not least, I can never be grateful enough to my beloved wife, Xue Li, for her standing by me, especially when I was in frustration and depression. Her understanding and optimism always give me the courage to embrace the challenges and overcome the difficulties in my life positively. Also, I want to express my genuine gratitude to my father, mother, grandparents, and relatives for giving their numerous support to me for finishing my PhD study.

Declaration

I hereby declare that the research recorded in this thesis is my own work, produced without the prohibited assistance of third parties and without making use of aids other than those specified. The thesis has been written entirely by myself and the work presented has been conducted at the University of Edinburgh from 2014–2018 under the supervision of Prof. Rebecca Cheung. This work has not been submitted for any other degree or professional qualification.

Rui Zhang

Signature Date

Contents

List of Figures

List of Tables

Chapter 1 Introduction

This chapter first gives an overall introduction to the unique characteristics of two-dimensional (2D) materials especially transition metal dichalcogenides (TMDs) in Section 1.1. Then current experimental research progress relating to the mechanical properties of 2D materials and their potential applications in the future will be reviewed in Section 1.2 and Section 1.3, respectively. Afterwards, Section 1.4 will present the subject of this research, and Section 1.5 will provide the outline of this thesis.

1.1 Introduction to 2D transition metal dichalcogenides (TMDs)

Since the first successful preparation of graphene (a single layer of carbon atoms arranged in a hexagonal lattice as shown in Figure 1-1a) by mechanical exfoliation from graphite crystals in 2004 [1], two-dimensional (2D) materials have attracted dramatic attention due to their extraordinary physical properties (high Young's modulus and high ultimate tensile strength) [2-7] and outstanding electrical properties [1] compared with conventional bulk materials. In the past few years, graphene, with the highest measured Young's modulus (≈1 TPa) [3], is the most widely studied 2D material. Studies have shown that graphene filled into the polymer matrixes can reinforce the mechanical properties of the composites significantly [8]. However, pristine graphene does not have a band gap [9], which limits its applications in the fields requiring a semiconducting material. Distinct from graphene, the transition metal dichalcogenides (TMDs) with the formula MX_2 in the 2H phase (one layer of transition metal M atoms sandwiched between two layers of oxygen family X atoms with the hexagonal symmetry as shown in Figure 1-1b) possess intrinsic band gaps [10, 11]. Figure 1-2 compares the transfer characteristics of field-effect transistors (FETs) made from graphene and monolayer MoS_2. The current on/off ratio of the graphene FET is below 10 (Figure 1-2a), while the MoS_2 FET can reach as high as

1×10^6 (Figure 1-2b), showing the great advantages and suitability of TMDs in semiconductor applications, including logic circuits and optoelectronics [12-15].

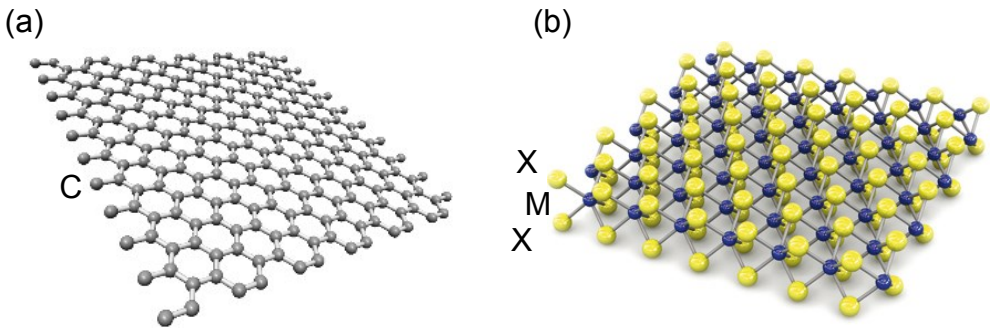

Figure 1-1. The schematic structures of graphene (a) and monolayer TMD (b) with the formula of MX_2 [11].

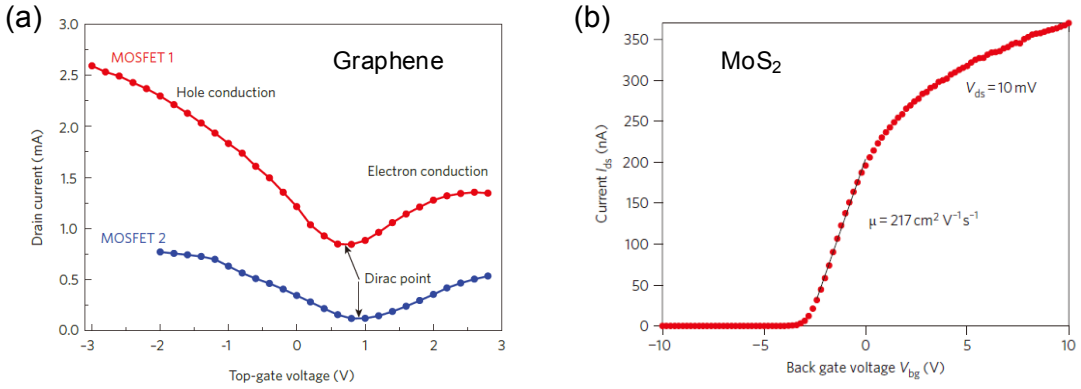

Figure 1-2. (a) Typical transfer characteristics for two top-gated graphene FETs. The current on/off ratios are about 3 (MOSFET 1) and 7 (MOSFET 2), far below what is needed for applications in logic circuits. [16] (b) Transfer characteristic for a back-gated monolayer MoS_2 FET with the current on/off ratio higher than 1×10^6 for the ±10 V range of gate voltage V_{bg}. [17]

In addition, as the gate length of metal-oxide-semiconductor field-effect transistors (MOSFETs) rapidly approaches sub-10 nm scale, the short-channel effect is becoming a key factor for limiting the miniaturization of conventional Si-based transistor [18]. The layered 2H-TMDs, such as MoS_2, WS_2, and WSe_2, with promising carrier transport properties, high on/off ratio, and most importantly, scalable thickness down to monolayer, have triggered tremendous interest in the application of future scaled

devices [17, 19]. Figure 1-3 demonstrates a prototype of MoS_2 FET with only 1 nm gate length using carbon nanotube (CNT) as the gate electrode, which exhibits excellent switching characteristics with near ideal subthreshold swing of ≈65 mV per decade and an on/off current ratio of $\approx 10^6$. Furthermore, by using the dependence of TMD-based FETs' electrical performance on different operating conditions, TMD-based FETs have been demonstrated widely for sensing applications, such as strain/pressure/motion sensor [20-22], gas sensor [23-26], and biosensor [27, 28]. Moreover, the existence of piezoelectrical and more sensitive piezoresistive effects in TMDs compared to graphene makes them more attractive for innovative applications including tactile strain sensors [29] and nanogenerators [30].

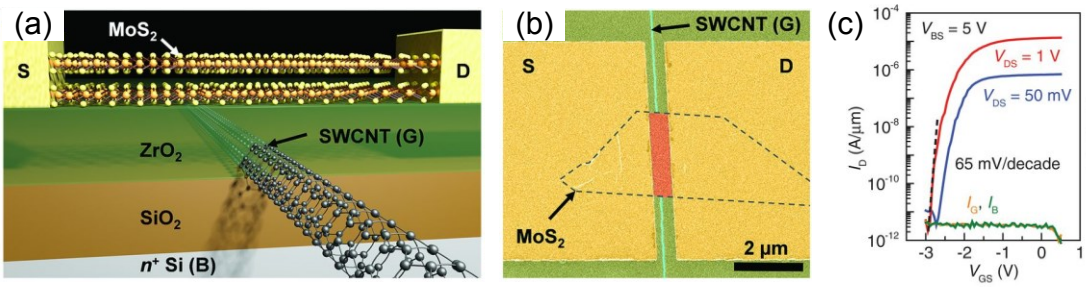

Figure 1-3. (a) Schematic of 1D2D-FET with a MoS_2 channel and CNT gate. (b) Optical image of a representative device shows the MoS_2 flake, gate (G), source (S), and drain (D) electrodes. (c) Transfer characteristics of a bilayer MoS_2 channel CNT gated FET at V_{BS} = 5 V and V_{DS} = 50 mV and 1 V. [19]

Meanwhile, the properties of TMDs are layer-dependent which has attracted dramatic attention recently. A transition from an indirect band gap in the bulk TMDs to a direct gap in the monolayer TMDs has been reported [10, 31]. For WSe_2 the indirect band gap of 1.1 eV in the bulk crystal increases to a direct band gap of 1.6 eV in monolayer form [32]. The direct band gap also results in enhanced photoluminescence efficiency from monolayer TMDs. Particularly, the 2D WSe_2, reported to own high optical quality, including strong photoluminescence intensity (100 to 1000 times stronger than the bulk materials) [10] along with high electroluminescence (photon emission rate of ≈16 million s^{-1} at the applied current of 35 nA) [33] and photo-conversion efficiency

(up to 6.7% under 532 nm illumination) [34], is a promising 2D material for applications in optoelectronic devices.

1.2 Mechanical properties of 2D materials

So far no plastic deformation has been observed from 2D materials, therefore 2D materials are generally considered to be brittle materials. In this section, the experimentally measured elastic properties and strain induced band gap change of various 2D materials from previous reports will be presented and compared.

1.2.1 Elastic properties

In layered 2D materials, the nearby atoms in the same plane are bonded covalently with low defect densities resulting in strong in-plane mechanical properties, while the interlayers are stacked together via weak van der Waals interaction, allowing layers to slide easily when shear stress is applied, the effect of which can give rise to lubrication properties. The above features result in possession of high anisotropy between in-plane and out-of-plane mechanical properties of 2D materials. Table 1-1 summarizes the reported in-plane mechanical properties of 2D material families ranging from conductor (graphene), semiconductor (TMDs and black phosphorus (BP)) to dielectric (graphene oxide (GO), mica, and h-BN) under application of tension. Overall, the Young's moduli of 2D materials are generally larger than the corresponding bulk crystals, due to lower crystal defects and interlayer stacking faults in 2D materials [6].

Pristine monolayer graphene (prepared by mechanical exfoliation from bulk graphite) is reported to be the 2D material with the highest Young's modulus ≈1 TPa [3, 35, 36] so far, because of the strong in-plane covalent carbon-carbon bonds. Meanwhile, the Young's moduli of some 2D materials (e.g., MoS_2, BP and h-BN) [2, 7, 37, 38] have been found to decrease with an increase in their thickness (number of layers), which is possibly caused by interlayer sliding in multilayer 2D materials during measurement [7]. Furthermore, the 2D materials with highly anisotropic in-plane atomic structure, such as BP, present anisotropic in-plane Young's moduli along different crystal orientations [39].

Table 1-1. Summary of the in-plane mechanical properties of 2D materials measured from experiments.

Material	**Number of layers**	**Young's modulus (GPa)**	**Pretension (mN/m)**	**Breaking stress (GPa)**	**Breaking strain (%)**	**Ref.**
Graphene (Mechanically exfoliated)	1	1000 ± 100	70~740	130 ± 10	≈12	[3]
	23–43	≈1000	N/A	N/A	N/A	[40]
	4	930 ± 48	N/A	N/A	N/A	[41]
	1–5	1000 ± 31	N/A	N/A	N/A	[36]
	3–14	≈800	N/A	N/A	N/A	[42]
Graphene (Mechanically exfoliated plus Ar plasma irradiated)	1	≈1550	200~800	80~94	N/A	[43]
Graphene (GO reduced)	1	250 ± 150	N/A	N/A	N/A	[4]
Graphene (CVD grown)	1	≈157	≈85	≈35	N/A	[44]
	1	≈1000	N/A	≈121 (small grain) ≈140 (large grain)	N/A	[45]
	1	≈800	≈100	≈55	N/A	[46]
MoS_2 (Mechanically exfoliated)	1	270 ± 100	20~100	22 ± 4	6~11	[7]
	2	200 ± 60		21 ± 6		
	5–25	330 ± 70	50 ± 20	N/A	N/A	[6]
MoS_2 (CVD grown)	1	260 ± 18	110 ± 40	N/A	N/A	[37]
	2	231 ± 10	N/A			
WS_2 (CVD grown)	1	272 ± 18	150 ± 30	N/A	N/A	[37]
BP (Mechanically exfoliated)	17–35	27 ± 4 (armchair direction)	N/A	2.2 (armchair direction)	7.2 (armchair direction)	[39]

		59 ± 12 (zigzag direction)		4.2 (zigzag direction)	6.5 (zigzag direction)	
	17	276 ± 32	180~1200	>25	>8	[38]
	37	90 ± 6.4				
GO (Solution-based deposited)	1	208 ± 23	54 ± 14	N/A	N/A	[47]
	2	224 ± 18	32 ± 6			
	3	230 ± 27	28 ± 4			
Mica (Mechanically exfoliated)	2–14	202 ± 22	140 ± 80	4~9	2~4.5	[48]
h-BN (CVD grown)	2	279 ± 20	8.8 ± 1.2	≈9	2.2	[2]
	4	269 ± 13	12.8 ± 1.3			
	5	252 ± 15	15.7 ± 1.5			

In addition, the mechanical property of 2D materials largely depend on the density of crystal defects and thus is related to the preparation method. For instance, the larger number of vacancy defects and the existence of wrinkles in the 2D materials can contribute to weaker mechanical properties [4, 44]. Research has shown that the mechanical properties can be recovered by flattening the wrinkles in chemical vapour deposition (CVD) graphene with a small pre-stretch [46]. In addition, the presence of a greater number of grain boundaries can affect the Young's modulus of 2D materials negatively [45]. More interestingly, the mechanical properties of 2D materials can also be improved by introducing certain level of defects, such as Ar^+ plasma irradiation [43].

The factors that can affect the pretension in the measured 2D materials are quite complicated. The pretension not only depends on the intrinsic mechanical properties of 2D materials but also the approach of transferring 2D materials onto the substrates. Therefore, the pretension values of the measured 2D materials in Table 1-1 vary significantly. Generally speaking, the dry transfer process with Scotch tape or viscoelastic stamp introduces higher pretension compared with wet transfer process

such as solution-based deposition [47]. Annealing, as a common method to remove the fabrication residues on 2D materials, can introduce thermal stress due to the different thermal expansion coefficients between 2D materials and substrates.

In addition, the 2D materials with higher Young's moduli usually possess higher breaking stress (the maximum stress a material can withstand before breaking), as presented in Table 1-1. Many reports have found that the breaking stress of 2D materials can reach the theoretical upper limit ($E_Y/9$) [7], where E_Y is the Young's modulus, due to low disorders and impurities in the characterized 2D materials. The existence of anisotropic breaking stress along armchair and zigzag directions has been found in black phosphorus (BP), possibly contributing from its anisotropic Young's modulus [39]. Except for the 2D dielectrics (mica and h-BN), the breaking strain (the amount of strain which can cause materials to break) of most 2D materials is above 7%, which is comparable to the common materials used for substrates of flexible devices, namely polyimide (PI) or polydimethylsiloxane (PDMS) [49].

1.2.2 Strain engineering of band gap

Recent experimental studies have shown that the strain in 2D materials can modify the band gaps of TMDs. The evolution of band gaps of 2D materials under strains have been investigated widely so far through photoluminescence (PL) spectroscopy [50-53]. The working mechanism of PL spectroscopy for detecting the band gap of semiconductors will be introduced in Section 2.2. So far, the theoretically predicted band gap opening in graphene by strain has not been achieved in experiments. Most of the studies with respect to the band gap engineering with strain focus on the semiconducting 2D materials, especially 2D 2H-TMDs.

Taking 2D MoS_2 for example [50], the PL spectrum of unstrained monolayer MoS_2 mainly comprises of an A peak at ≈1.82 eV originating from the direct transition at the K point of the Brillouin zone (Figure 1-4a). Whereas, apart from the A peak, the PL spectrum of bilayer MoS_2 features an additional I peak located at ≈1.53 eV due to the transition across the indirect band gap between the Γ and K points (Figure 1-4c). When the tensile strain is applied, the A peak of monolayer MoS_2 redshifts approximately linearly with strain at a rate of 45 ± 7 meV/% (Figure 1-4b). For bilayer MoS_2, the A and I peaks are redshifted with rates of 53 ± 10 and 129 ± 20 meV/% under strain,

respectively (Figure 1-4d). The observed redshifts of the PL peaks are indicative of tensile strain induced band gap reductions of MoS_2. In addition, a transition from an optically direct to indirect material under tensile strain has been observed from monolayer MoS_2 [50], while multilayer WSe_2 has been reported to undergo strain-induced indirect to direct band gap transitions [51].

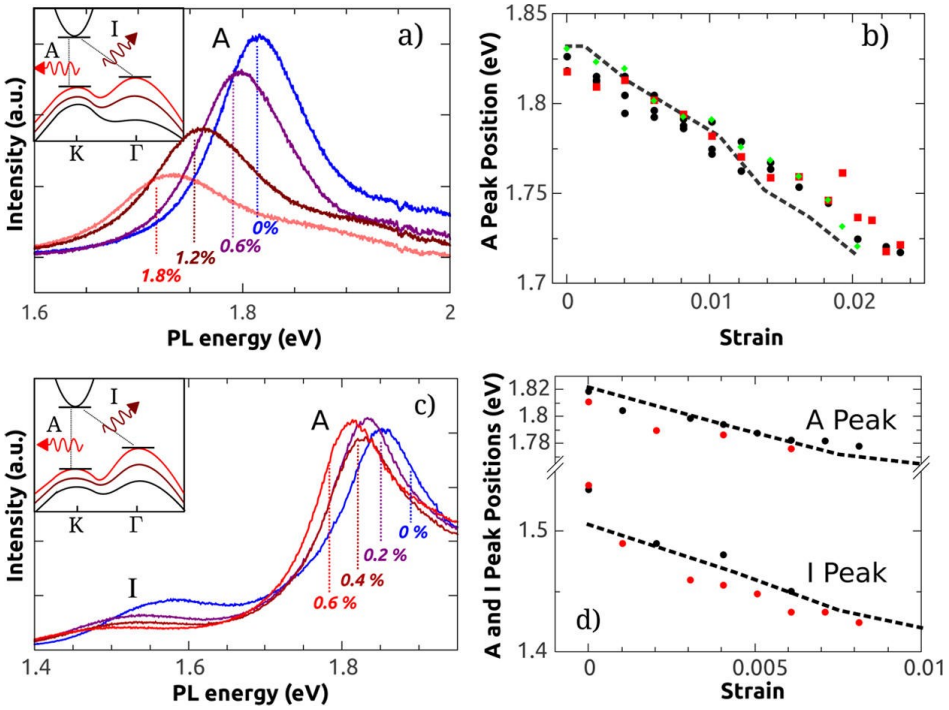

Figure 1-4. Photoluminescence (PL) spectra of strained MoS_2. (a) PL spectra of a monolayer MoS_2 strained from 0 to 1.8%. (b) Evolution of the A peak position of the PL spectrum under strain for several monolayer MoS_2. (c) PL spectra of a bilayer MoS_2 as strain increases from 0 to 0.6%. (d) PL peak positions for the A and I peaks of several bilayer MoS_2 as a function of strain. Insets in (a) and (c) present schematic band structures of monolayer and bilayer MoS_2 under 0% (black), ≈5% (brown), and ≈8% (red) strains. [50]

Table 1-2 lists the experimentally measured shift rates of the PL peaks under strain for various TMDs. The consistently negative shift rates obtained from the listed TMDs indicate that the band gaps of the TMDs can be reduced (increased) as the tensile (compressive) strain increases. However, the sensitivities of band gaps to strain might be distinct depending on the preparation method of 2D TMDs (mechanical exfoliation

or CVD growth), the composition of 2D TMDs, and the type of applied strain (uniaxial or biaxial).

Table 1-2. Summary of the PL peak shift rates of semiconducting 2D TMDs under strains.

Material	**Number of layers**	**Peak shift rates (meV/%)**		**Strain type**	**Approach of applying strain**	**Ref.**
		A peak (Direct transition)	**I peak (Indirect transition)**			
MoS_2 (Mechanically exfoliated)	1	−45 ± 7	N/A	Uniaxial tension	Four-point bending (embedded)	[50]
	2	−53 ± 10	−129 ± 20			
	3–5	−36	N/A	Uniaxial tension	Release of pre-stretched substrate (supported)	[54]
	1	−64 ± 5	N/A	Uniaxial tension	Cantilever-flexure (supported)	[52]
	2	−48 ± 5	−77 ± 5			
	1	−48	N/A	Uniaxial tension	Three-point bending (supported)	[53]
	2	−46	−86			
MoS_2 (CVD grown)	3	−300	N/A	Biaxial compression	Piezoelectric substrate (supported)	[55]
WS_2 (CVD grown)	1	−11.3	−18.7	Uniaxial tension	Stretching the PET (supported)	[56]
ReS_2 (Mechanically exfoliated)	1	−42.7	N/A	Uniaxial tension	Release of pre-stretched substrate (supported)	[57]
$MoSe_2$ (Mechanically exfoliated)	1	−27 ± 2	N/A	Uniaxial tension	Two-point bending (embedded)	[58]

1.3 Applications of 2D materials

By taking advantage of the extraordinary mechanical properties (high breaking strain as listed in Table 1-1) as well as mechano-electric transduction properties

(piezoresistivity and piezoelectricity), 2D materials have been demonstrated to be promising for novel applications of flexible electronics, strain sensor, nanogenerator, and resonator. In this section, some examples of such applications of 2D materials will be given.

1.3.1 Flexible FET

The combination of high breaking strain, low thickness and versatile electronic properties of 2D materials makes them competitive contenders for flexible electronic applications. The semiconducting properties of TMDs can be used as channel materials in flexible transistors while pristine graphene with relatively high conductivity is suitable as an electrode material. Mica and h-BN with large band gaps can be used for 2D gate dielectrics [59, 60]. Figure 1-5a shows a flexible and transparent FET fabricated from all-2D materials on a polyethene terephthalate (PET) flexible substrate [61]. The structure of the FET is depicted in the inset of Figure 1-5b. As shown in Figure 1-5b, the device has been found to exhibit a p-type FET characteristic with slight alternations within 2%. strain. Figure 1-5c shows the output characteristics of the flexible transistor with the feature of current saturation similar to conventional Si-based transistors.

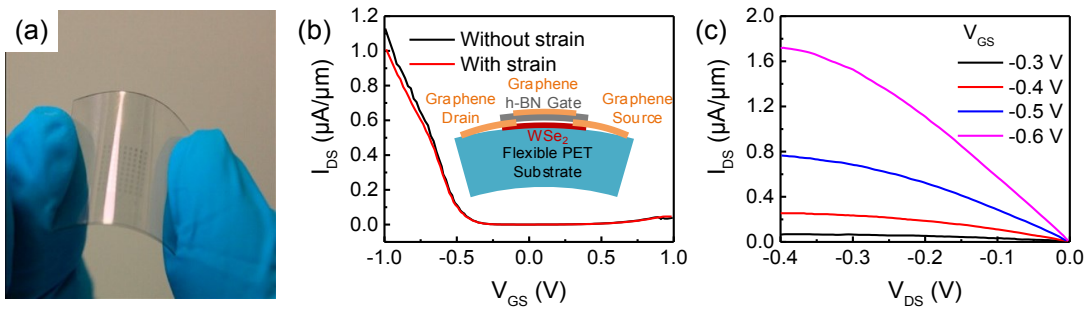

Figure 1-5. (a) All-2D materials-based FETs on a flexible PET substrate. (b) Transfer characteristics of the FET without (black) and with (red) 2% strain. Inset: side view schematic of the flexible FET. (c) Output characteristics of the FET. Adapted from [61].

1.3.2 Strain sensor

As mentioned in Section 1.2.2, 2D materials undergo band gap change when external strain is applied [56, 62]. In addition, the distortion of 2D materials may result in additional carriers scattering thus reducing the carrier mobility [63]. The above factors contribute to the piezoresistive effect, in which the resistivity of 2D materials is modulated by mechanical deformation. Thus, 2D materials can be used as strain or pressure sensor [64, 65] by taking advantage of the piezoresistive effects. The sensitivity of a strain sensor is usually characterized by its gauge factor (GF), defined as $(\Delta R(\varepsilon)/R_0)/\varepsilon$, where R_0 is the total resistance of the unstrained device and $\Delta R(\varepsilon)$ is the resistance change under strain ε. The GF of pristine graphene has been characterized to be as low as ≈2 [65-69] due to the zero band gap and large strain required to open the band gap, which can be a significant disadvantage for strain sensors. On the other hand, the GF of monolayer MoS_2 can reach approximately −200 [30, 70] resulting from the higher sensitivity of the decreasing band gap along with the direct-indirect band gap transition under tensile strain, which makes MoS_2 more suitable for strain sensing applications. The sensing performances of 2D strain sensors can also be enhanced by optimizing the structure design, such as the piezopotential-gated graphene matrix sensor arrays (GF = 389, Figure 1-6a) [29], quasi-continuous nanographene film sensor (GF = 507, Figure 1-6b) [71, 72], and graphene woven fabric sensor (GF = 1000) [73, 74].

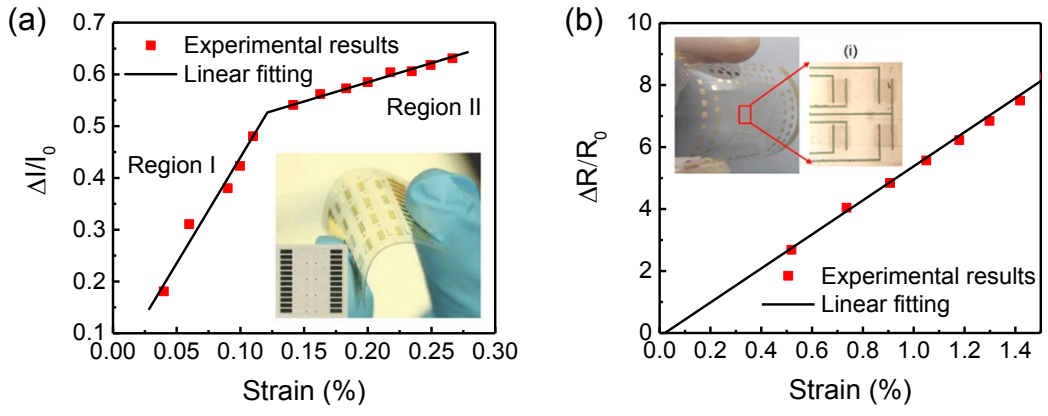

Figure 1-6. Sensing characteristics of (a) piezopotential-gated graphene matrix strain sensor (adapted from [29]) and (b) quasi-continuous nanographene film strain sensor (adapted from [71]).

Moreover, the piezoresistive effect, combined with the high breaking strain of 2D materials enable the design of wearable strain sensors for human motion detection. Figure 1-7(a) shows a prototype of a tactile sensor fabricated with graphene films on a PDMS substrate attached onto a human wrist. As shown in Figure 1-7(b), the motions of the test subject can be captured clearly with the fabricated strain sensor by outputting varying current responses under different motions [29].

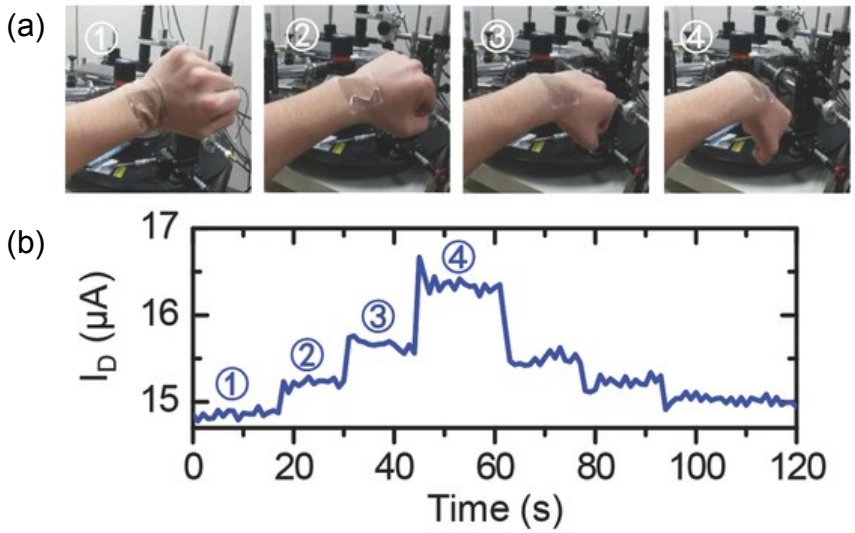

Figure 1-7. (a) A graphene tactile strain sensor attached onto the wrist detecting the hand motion. (b) The electrical response of the tactile strain sensor in the different hand motions shown in (a). [29]

1.3.3 Nanogenerator

Research has shown that TMDs with an odd number of layers possess the piezoelectric property due to the absence of inversion symmetry [30, 75]. Figure 1-8a shows a flexible device made of a monolayer MoS_2 flake outlined with black dashed lines. When the substrate is bent from the two ends mechanically, the MoS_2 flake will be stretched, and hence piezoelectric polarization charges will be induced at the zigzag edges of the MoS_2 flake which can drive the flow of electrons in an external circuit as depicted in Figure 1-8e. When the substrate is released, electrons flow back in the opposite direction as shown in Figure 1-8f. Figure 1-8b-c show that the periodic stretching and releasing of the substrate can generate piezoelectric outputs in the

external circuit with varying polarity which converts mechanical energy into electricity. A maximum mechanical-to-electrical energy conversion efficiency of 5.08% has been achieved from the device [30]. The existence of piezoelectricity, together with the mechanical flexibility of some 2D materials demonstrate their potential applications in wearable power generated nanodevices.

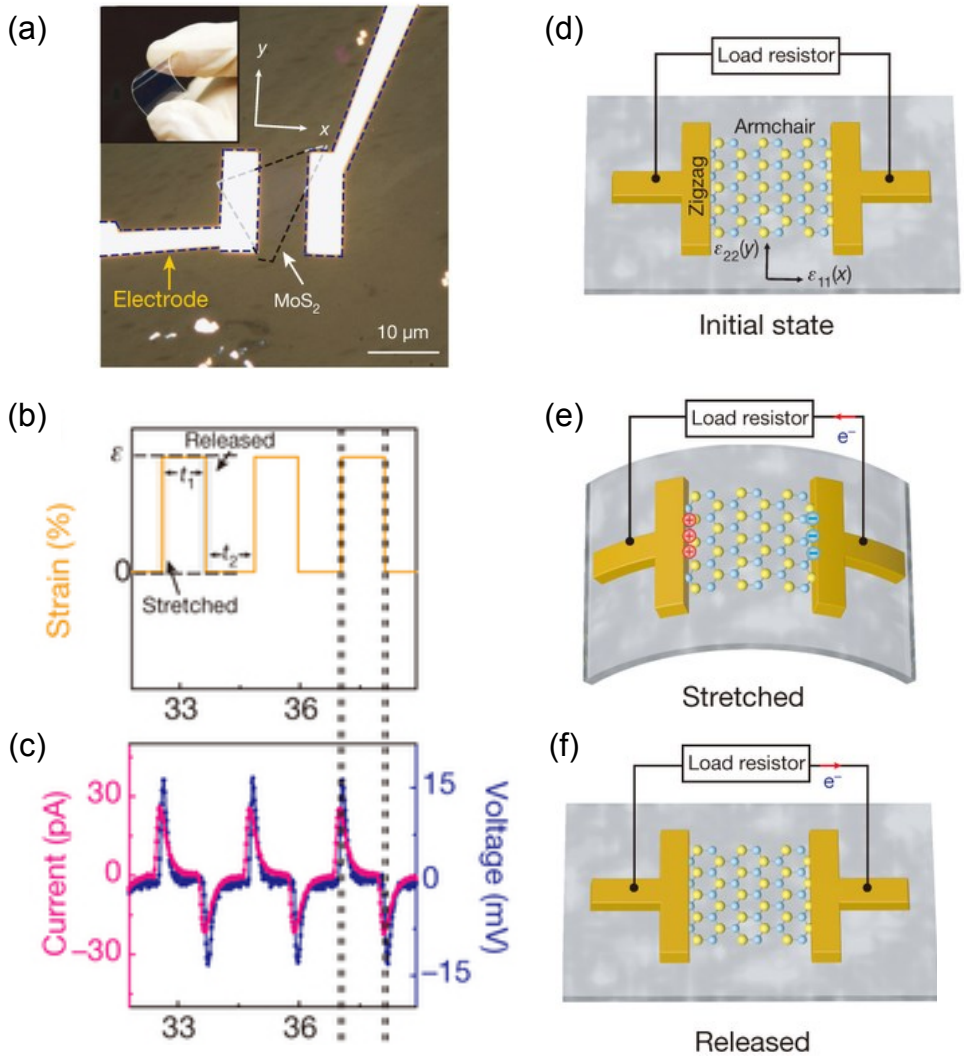

Figure 1-8. (a) A flexible device made from a monolayer MoS_2 flake and metal electrodes at its zigzag edges. (b) Applied periodic strain via bending of the substrate versus time. (c) Corresponding piezoelectric outputs when strain is applied along the armchair direction. Operation of the MoS_2-based piezoelectric device in the initial state (d), bent state (e), and released state (f). [30]

1.3.4 Resonator

Nanoelectromechanical systems (NEMS) resonator, a kind of resonator with the suspended structure on the nanoscale, offering the potential for extreme mass and force sensitivity [76, 77], has triggered intense interest in recent years. The resonant frequency of the resonators depends greatly on their geometry and mechanical properties of the vibrational materials (such as Young's modulus and mass density) [78]. As the sensitivity of resonators improves with increasing resonant frequency, graphene is promising for highly sensitive NEMS applications due to its ultrahigh Young's modulus. Figure 1-9a shows a schematic (left) and an SEM image (right) of a graphene resonator. The electrical actuation and detection of the mechanical vibrations of the graphene resonator are presented in Figure 1-9b. A DC voltage V_g applied to the gate causes static deflection of the graphene towards the gate. The resonant motion is actuated by an AC voltage with an amplitude of V_a and frequency of ω_a applied to the drain electrode and read out by current mixing method [76] using a lock-in amplifier. As shown in Figure 1-9c, when V_g = 0 V and V_a = 250 mV, the fundamental resonance frequency (Peak A) is ≈1 MHz and the second vibration mode (Peak B) is measured to be ≈2 MHz. The amplitude of vibrational modes increases with increasing V_a. However, the resonant frequency decreases as V_a increases due to nonlinear damping effects at higher resonance amplitudes [79]. By operating the graphene resonant sensors in the second mode regime, the detection sensitivity can be improved significantly [80].

NEMS with low resonant frequency can be used for acoustic electronics, such as acoustic sensors [81] and loudspeakers [82]. Since the resonant frequency of resonators can be tuned inversely by increasing the lateral dimension or reducing the thickness of the vibrational structures, resonators with lower resonant frequency can be realised by using thin 2D membranes in a larger lateral dimension. Figure 1-10 shows the response of a graphene resonator working in the low resonant frequency regime [81]. The resonator has been actuated with a piezoelectric disc driven with a sinusoidal signal and detected using a laser Doppler vibrometer (LDV). The fundamental resonant frequency has been measured to be ≈16 kHz for a 3 × 3 mm^2 CVD graphene membrane, which lies in the audio range (20Hz~20kHz).

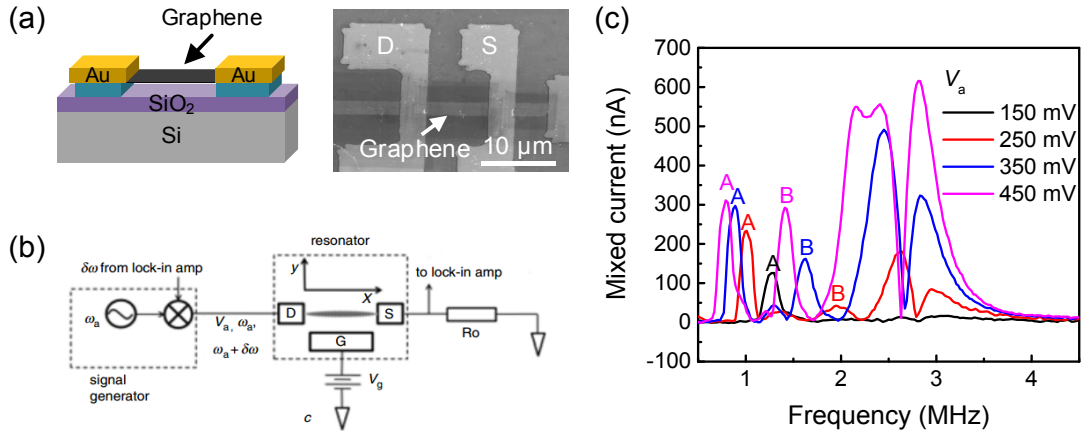

Figure 1-9. (a) Schematic and SEM image of a graphene resonator. (b) Circuit diagram of the current mixing characterization setup. (c) The mixed current versus driving frequency under different amplitudes of actuation voltages V_a. Adapted from [80].

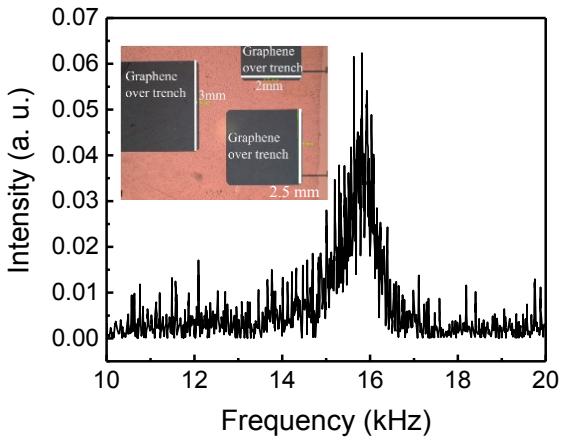

Figure 1-10. Resonant response for a 3×3 mm^2 CVD graphene membrane obtained with a laser Doppler vibrometer (LDV). Adapted from [81].

1.4 Goal of this research

In one aspect, this research aims to deepen the understanding of the influence of the field-effect on the fundamental properties (including the crystal structure, band structure, and electrical transport property) of 2D semiconducting 2H-WSe_2 to pave the way for the practical applications of 2D WSe_2 in versatile field-effect devices. In addition, as the study on suspended WSe_2 is still absent, a comparison of the electrical transport properties of substrate-supported and suspended WSe_2 is in demand.

Furthermore, to realize tailoring of the performance of 2D WSe_2 via thickness engineering and applications of 2D WSe_2 in complex logic circuits and optoelectronics (e.g., solar cells and light-emitting diodes), a thinning and chemical doping method of WSe_2 with good controllability, air stability, easy scalability yet to be developed. On the other hand, the elastic property of 2D WSe_2 remains to be characterized experimentally to examine the suitability of 2D WSe_2 in flexible device applications. Meanwhile, the strain engineering of electrical transport properties of 2D WSe_2 is still unknown. Therefore, the relevant study is essential to explore the feasibility of the application of 2D WSe_2 in strain sensors.

1.5 Thesis arrangement

Figure 1-11 illustrates the skeleton of this thesis. The wide blue arrows indicate the sequence of the chapters, while the narrow orange arrows indicate the relationships of each chapter with the primary research contents included in this thesis. Following on the introduction of the research methods adopted in this research in Chapter 2, the fabrication processes of back-gated 2D WSe_2-based FETs that enable the experimental studies of the field-effect and chemical doping will be detailed in the first part of Chapter 3. Apart from that, the successful fabrication of a suspended 2D WSe_2 FET will also be demonstrated. The second part of Chapter 3 will comparatively present the experimental results of electrical characterization of substrate-supported and suspended 2D WSe_2-based FETs. Meanwhile, how the field-effect, metal contact resistance, and substrate support affect the electrical performance of the WSe_2 FETs will be analysed. Move on to the Chapter 4, a controllable layer thinning and air-stable chemical doping of WSe_2 by the approach of vapour XeF_2 will be elaborated. The mechanism of the layer thinning and chemical doping of WSe_2 by vapour XeF_2 will also be elucidated with the assistance of the Raman, photoluminescence (PL) and X-ray photoelectron spectroscopy (XPS) analysis. In Chapter 5, the in-plane elastic properties of 2D WSe_2 obtained from indentation experiments implemented with an atomic force microscope (AFM) will be presented. A comparison of the elastic properties of 2D WSe_2 to other 2D materials will be provided. The suitability of 2D WSe_2 for flexible device applications will also be discussed. After the experimental studies conducted in the previous chapters, theoretical calculations based on the

density functional theory (DFT) will be given in Chapter 6 to gain more insights on the influence of strain and field-effect on the crystal structure, band structure, density of states (DOS), and electrical transport property of 2D WSe_2 for future practical applications of WSe_2-based strain sensors and novel field-effect devices. In the last chapter (Chapter 7), the main achievements of this thesis will be summarized, and some follow-up work worth to be done in the future will also be proposed.

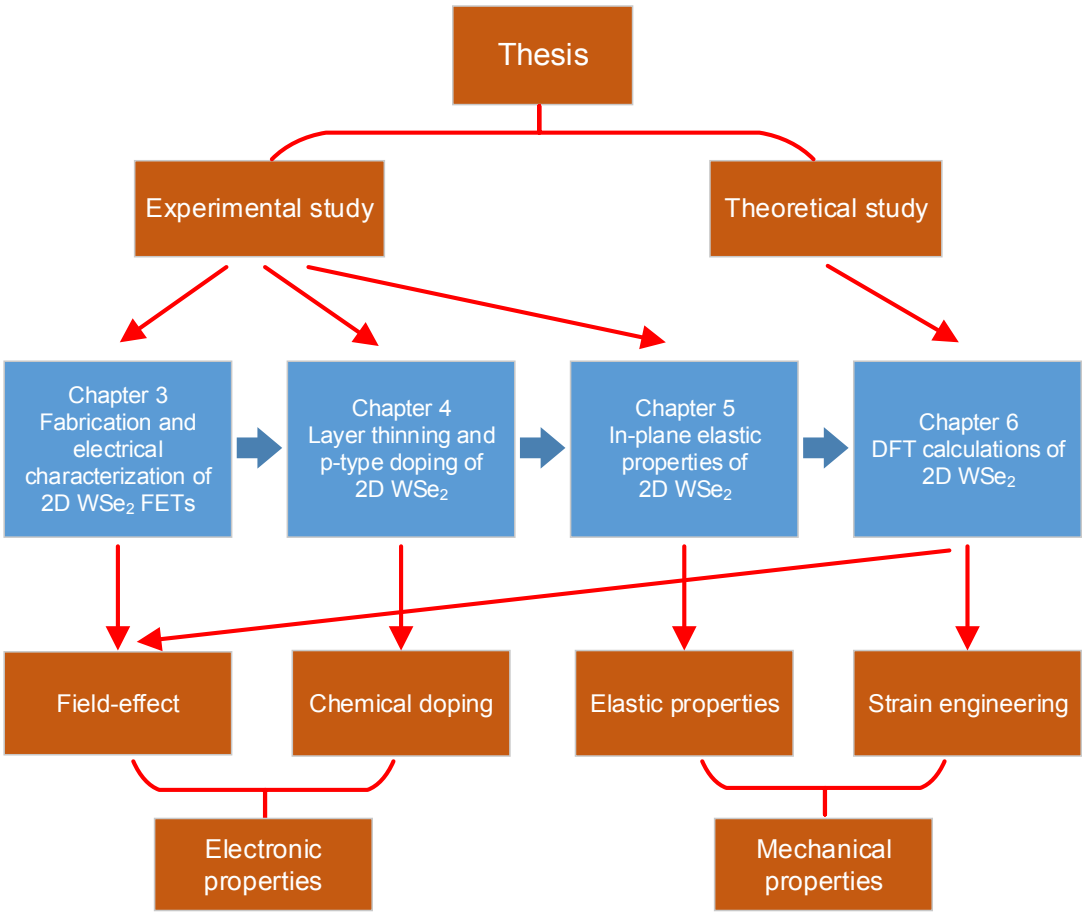

Figure 1-11. The diagram of the structure of this thesis.

Chapter 2 The methodology

This chapter firstly introduces the preparation method of 2D WSe_2 employed in this research (Section 2.1). Then the working principles and characterization parameters of Raman/photoluminescence spectrometer, X-ray photoelectron spectrometer and atomic force microscope are described in Section 2.2, Section 2.3, and Section 2.4, respectively. The last section (Section 2.5) provides a brief introduction to the density functional theory (DFT) and the DFT calculation parameters used.

2.1 Preparation and transfer of 2D WSe_2

During the experiments in this thesis, 2D semiconducting 2H-WSe_2 have been prepared and transferred onto thermal grown SiO_2 (300 nm)/Si substrates, which gives optimal colour contrast between 2D WSe_2 and substrates [83, 84], via a polydimethylsiloxane (PDMS) stamp. The schematics in Figure 2-1 show how a PDMS stamp has been made. A glass slide has been first treated with trichlorosilane in a vacuum environment (Figure 2-1a) to reduce the surface energy which enables the subsequent release of the PDMS stamp. Then two flat spacers (200 μm thick) have been positioned at the two ends of the glass slide, and uncured PDMS (well mixed in the elastomer to curing agent ratio of 10:1 and subsequently degassed) has been manually poured onto the middle area of the glass slide (Figure 2-1b). Afterwards, another piece of glass slide has been laid on top of the bottom glass slide to squeeze out the extra uncured PDMS by applying pressure to the two opposite ends of the glass slides. After this, the sample has been clamped at the two ends and baked in an oven at 100 °C for 35 min to cure the PDMS (Figure 2-1c). At the last step, the two glass slides have been separated slowly, and the PDMS has remained on the top glass slide that has not been treated with trichlorosilane previously (Figure 2-1d). As the glass slides are rigid with low surface roughness, a PDMS stamp with flat and smooth top surface can be made by this approach. Figure 2-1e shows an optical image of a fabricated PDMS stamp.

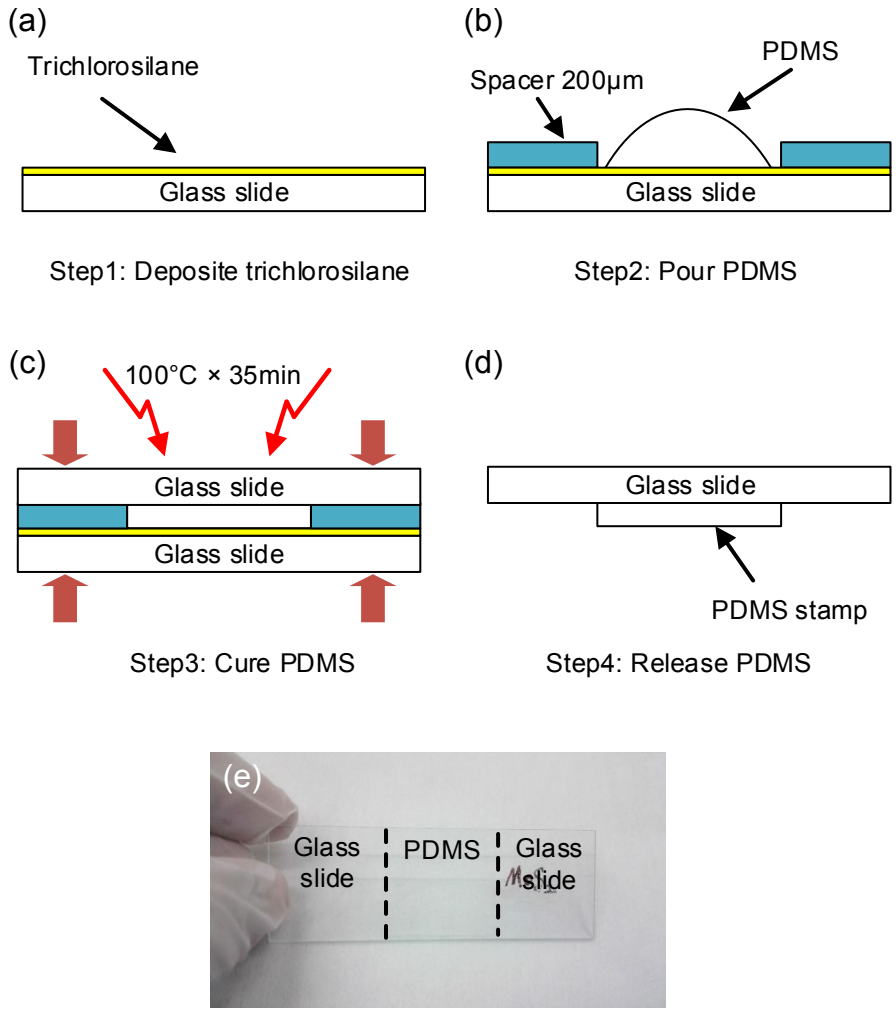

Figure 2-1. Schematics (a-d) showing the fabrication processes of a PDMS stamp and the optical image (e) of the fabricated PDMS stamp.

Then the PDMS stamp has been used for exfoliation and transfer of 2D WSe_2 onto SiO_2/Si substrates, as shown in Figure 2-2. Firstly, 2D flakes have been transferred onto the PDMS stamp by mechanical exfoliation of a bulk 2H-WSe_2 crystal (supplied by 2D Semiconductors Ltd. with the purity of 99.9999%) with Scotch tapes (Figure 2-2a, b). Afterwards, the PDMS stamp has been pressed against the top surface of an acceptor substrate (Figure 2-2c) and then peeled off very slowly to release the 2D flakes to the acceptor substrate (Figure 2-2d). Since the PDMS stamp behaves as an elastic solid over short timescales while it can flow slowly over long timescales [85], fast peeling off the Scotch tape from the PDMS stamp will transfer the 2D flakes onto the PDMS stamp (Figure 2-2b) while slowly peeling off the stamp from the SiO_2/Si

substrate can release the 2D flakes to the acceptor substrate (Figure 2-2d). In addition, the pre-treatment of the SiO_2 surface with O_2 plasma has been found to increase the transfer yield in Step 3 (Figure 2-2c), due to the enhanced bonding between 2D materials and SiO_2 surface [86]. After the transfer, the acceptor substrates have been immersed in acetone for 2 hours and subsequently rinsed with isopropyl alcohol (IPA) and deionized (DI) water to remove as many tape residues as possible. Figure 2-3 gives an example of optical and atomic force microscope (AFM) images of 2D WSe_2 flakes transferred on a SiO_2/Si substrate.

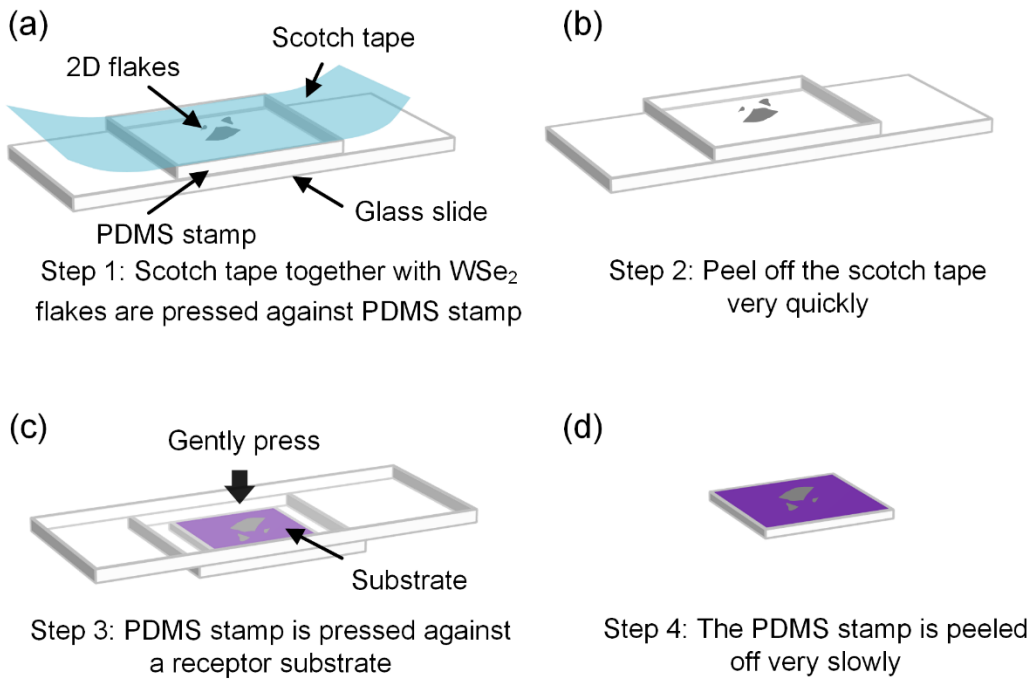

Figure 2-2. Schematics of exfoliation and transfer of 2D WSe_2 flakes onto a SiO_2/Si substrate with a PDMS stamp.

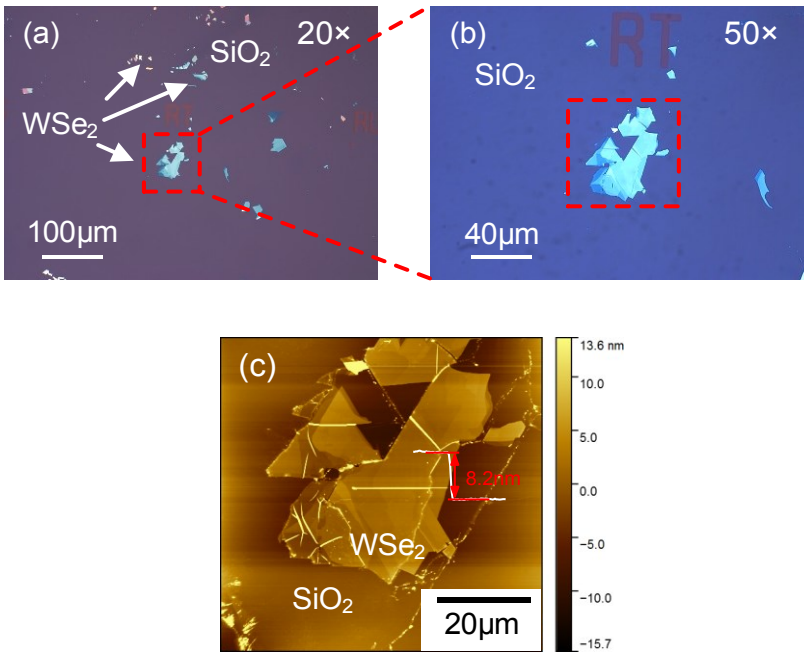

Figure 2-3. Optical images of mechanically exfoliated WSe_2 on a SiO_2/Si substrate under 20× (a) and 50× (b) magnifications. (c) AFM image of the WSe_2 flake highlighted in (b).

2.2 Raman and photoluminescence spectroscopy

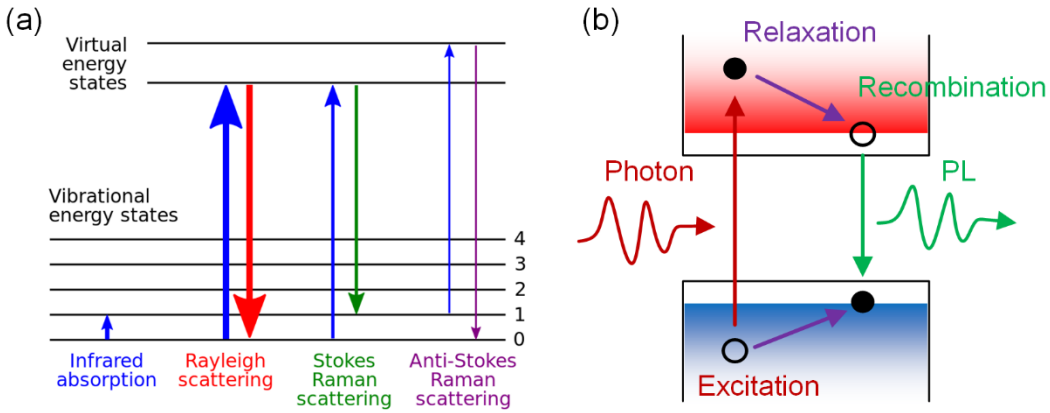

Figure 2-4. (a) Energy-level diagram showing the states involved in Raman spectra [87]. (b) Schematic band diagrams for the photoluminescence (PL) processes.

Raman spectroscopy is a spectroscopic technique used to observe vibrational, rotational modes in a sample, which relies on inelastic scattering or Raman scattering of incident radiation (typically from a monochromatic laser beam). The laser light

interacts with molecular vibrations, phonons or other excitations in the system, resulting in the upshift (anti-Stokes shift) or downshift (Stokes shift) of the energy of the laser photons, as depicted in Figure 2-4a. The shift in energy gives information about the vibrational modes in the system. Raman spectroscopy can identify the number of layers of 2D materials [88-90], determine the amount of doping [91-95], the presence of defects [96], and the thermal conductivity [97, 98].

On the other hand, photoluminescence (PL) spectroscopy is a method of probing the electronic structure of materials. In a typical PL experiment, a semiconductor is excited with a light source that provides photons with an energy larger than the band gap energy. Once the photons are absorbed, electrons and holes are formed with finite momenta in the conduction and valence bands (dark red arrow in Figure 2-4b), respectively. The excitations then undergo energy and momentum relaxation towards the band edges (purple arrow in Figure 2-4b). Finally, the excited electrons recombine with holes under emission of photons (green arrow in Figure 2-4b). The signatures of PL of 2D materials can be modified by the carriers doping [99, 100] and crystal defects [99, 101, 102].

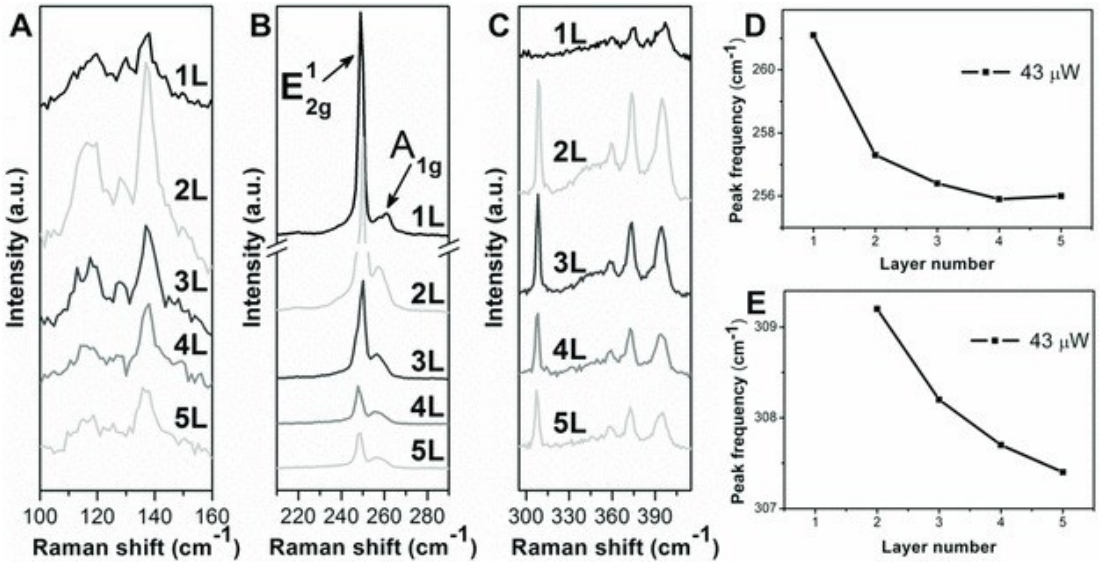

Figure 2-5. Raman spectra of 1- to 5-layer WSe_2 at the excitation power of 43 μW in the range of 100–160 cm^{-1} (A), 210–290 cm^{-1} (B), and 295–415 cm^{-1} (C), respectively. (D–E) Peak frequencies of A_{1g} mode (D) and the Raman peak near 308 cm^{-1} (E) as a function of the layer number of WSe_2. [103]

Figure 2-5 gives an example of Raman spectra of 1- to 5-layer WSe_2. For all samples, two strong peaks observed in the range of 245–265 cm^{-1} can be assigned to E^1_{2g} and A_{1g} modes, respectively (Figure 2-5 b). The strongest Raman spectrum arose from the bilayer (2L) WSe_2. Distinct from multilayer WSe_2, there is no notable peak around 308 cm^{-1} for monolayer (1L) WSe_2 (Figure 2-5 c). As the layer number of WSe_2 increased from 1- to 5-layer, the spectra became weaker, and a redshift of the A_{1g} mode and Raman peak around 308 cm^{-1} was observed (Figure 2-5 d, e), reflecting the presence of additional interlayer interaction modes.

Figure 2-6 shows the typical PL spectra of WSe_2 with different numbers of layers. The monolayer WSe_2 owing a direct band gap exhibits a prominent PL peak centred at 1.64 eV. Compared to monolayer WSe_2, the PL signal for bilayer and trilayer WSe_2 is broader and weaker, which can be described by at least two Lorentzian peaks due to the presence of indirect band gap. As the number of layers further increases (7- to 11-layer), WSe_2 displays two distinct PL peaks located at 1.39 and 1.59 eV, where the former probes the indirect band gap (Γ to K) and the latter is associated with the direct band gap (K to K). In addition, the overall PL signal obtained from few-layer WSe_2 is orders of magnitude weaker in intensity compared to monolayer WSe_2.

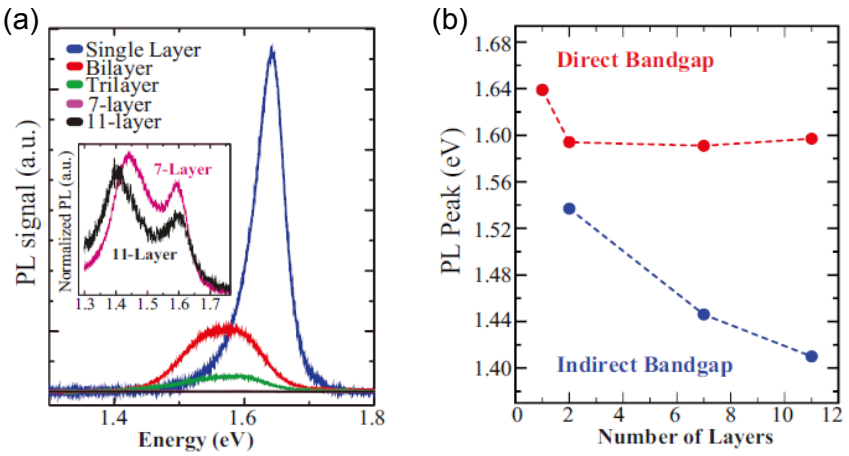

Figure 2-6. PL spectra (a) and PL peak positions (b) of WSe_2 with various layer numbers. [104]

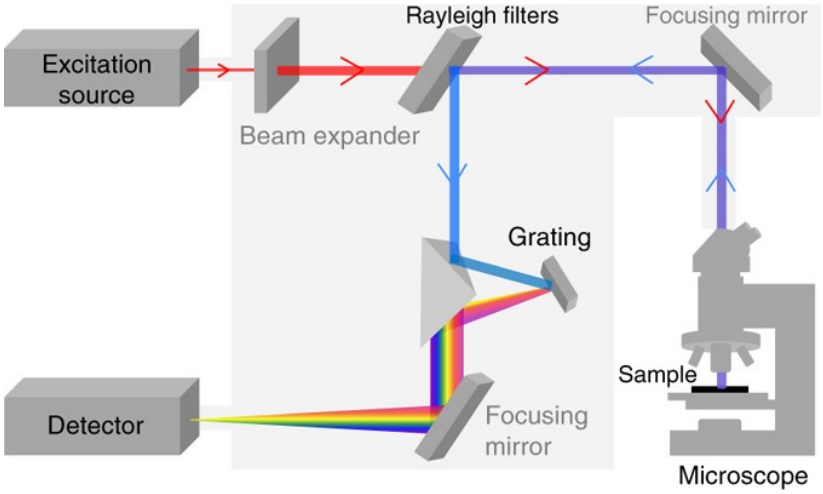

Figure 2-7. Schematic diagram of a Raman spectroscopy system [105].

During this project, the Raman and PL measurements were performed in a confocal Raman microscope (inVia Renishaw) under the ambient air condition with a 514 nm laser excitation. Figure 2-7 shows a basic composition of the Raman system. A 100× magnification objective (NA = 0.90) was used, which provided a laser spot size of ≈1.2 μm in diameter. The incident laser power was kept at ≈100 μW to avoid the sample heating effect. The Raman spectra were obtained with a 2400 lines mm^{-1} grating, resulting in a spectral resolution of ≈1 cm^{-1}. Each spectrum acquisition was accumulated for 10 times with 20 s per accumulation. Raman spectra were calibrated with the Raman band of Si substrate at 520 cm^{-1}. The PL spectra were collected using a 1200 lines mm^{-1} grating with an integration time of 50 s. Lorentzian fitting was applied to deconvolute the PL spectra.

2.3 X-ray photoelectron spectroscopy

X-ray photoelectron spectroscopy (XPS) is a surface-sensitive quantitative spectroscopic technique that can be used to analyse the surface chemistry of a material. As shown in Figure 2-8, an XPS system typically includes a focused X-ray source to irradiate the characterized sample and a hemispherical analyser to determine the number and kinetic energy of the excited photoelectrons. Then the electron binding energy of each of the emitted electrons can be determined by using the equation of

$E_{binding} = E_{photon} - (E_{kinetic} + \Phi)$, where $E_{binding}$ is the binding energy of the electron, E_{photon} is the energy of the X-ray photons being used, $E_{kinetic}$ is the kinetic energy of the photoelectron measured by the instrument and Φ is the work function dependent on both the spectrometer and the measured material.

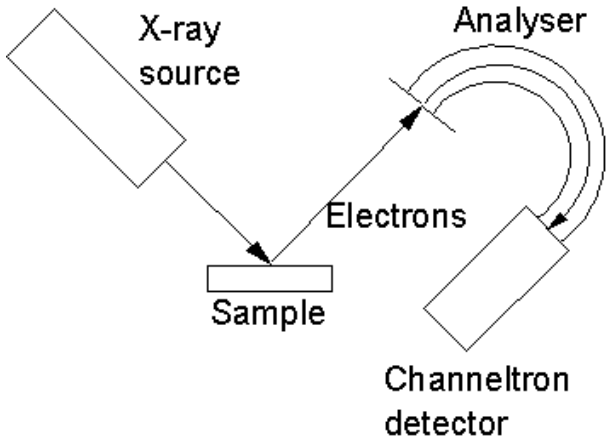

Figure 2-8. Schematic diagram of an X-ray photoelectron spectroscopy (XPS) system [106].

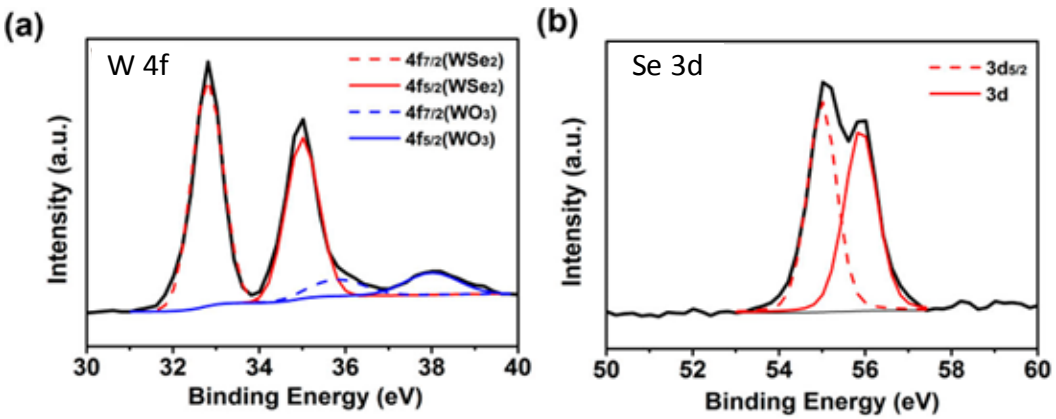

Figure 2-9. XPS spectra of the W 4f (a) and Se 3d (b) core levels of a CVD grown monolayer WSe_2. [107]

Figure 2-9 presents the XPS spectra of W 4f and Se 3d core levels obtained from a chemical vapour deposition (CVD) grown monolayer WSe_2 in Ref. [107]. The doublet peaks at 32.8 and 35.0 eV (Figure 2-9a) are attributed to the $W4f_{7/2}$ and $W4f_{5/2}$ core levels of WSe_2, while the peaks at 55 and 55.9 eV (Figure 2-9b) correspond to the Se $3d_{5/2}$ and Se $3d_{3/2}$ doublet. It is noted that a weaker doublet at 35.8 and 38.0 eV

associated with $W4f_{7/2}$ and $W4f_{5/2}$ core levels of WO_3 can also be observed in Figure 2-9a, which originates from the occasionally deposited WO_3 particles on the surface of WSe_2 during the CVD process.

In this research, XPS spectra of WSe_2 were obtained from a Theta Probe XPS system (Thermo Scientific) using a monochromated Al Kα X-ray source (hv = 1486.7 eV) with a spot size of 20 μm in radius in an ultrahigh vacuum chamber with a base pressure of $\approx 10^{-11}$ Torr. The hemispherical analyzer was operated at the Constant Analyzer Energy (CAE) mode with a 30 eV pass energy and 0.1 eV step size. The incident X-ray and the analyzer were positioned at angles of 30° and 50° with respect to the sample surface normal, respectively. The sampling depth of the XPS measurements is estimated to be 7~8 nm by the relation of 3λ, where the λ is the inelastic mean free path of an electron in WSe_2 which can be found from NIST Standard Reference Database 71 [108]. The Si 2p peak at 103.2 eV from the SiO_2 of the substrates and adventitious carbon C 1s peak at 284.8 eV were used for binding energy calibration of multilayer and bulk WSe_2, respectively. The high-resolution XPS core level spectra were analyzed by deconvolution with the least-squares fitting of the spectra with Gaussian-Lorentzian functions after the Shirley background subtraction. During the curve fitting, some constraints were applied: The spin-orbit splitting for the W $4f_{7/2}$ and W $4f_{5/2}$ components was fixed at 2.17 eV with an area ratio of 4:3 and same full width at half maximum (FWHM), while the $3d_{5/2}$–$3d_{3/2}$ components separation for Se was set into 0.86 eV with an area ratio of 3:2.

2.4 Atomic force microscopy

Atomic force microscope (AFM) installed with a cantilever with a very sharp tip (AFM probe) has been employed to scan the surface topography of 2D WSe_2 and measure the near-field force between the probe and 2D WSe_2. Figure 2-10 illustrates the working mechanism of a typical AFM system. The AFM uses a laser beam deflection system where a laser is reflected from the back of the reflective AFM probe onto a position-sensitive photodetector (photodiode). As a piezo tube scanner system controls the scanning of the tip on the sample surface in the horizontal (x, y) and vertical (z) directions with the resolution on the order of fractions of a nanometer, the deflection of the AFM probe induced by the interaction between the tip and sample can be tracked

by the displacement of the reflected laser on the photodetector. During the surface topography imaging, AFM uses a feedback loop to attempt to keep the cantilever deflection constant by adjusting the vertical movement of the piezo scanner with varying voltage, so that local height of the sample can be obtained. Also, AFM can be used for measurement of forces with piconewton resolution. In the force measurement mode, the AFM probe indents towards a fixed point of the sample by moving the piezo scanner vertically up. During the indentation, the AFM probe deflection versus piezo scanner displacement curve is recorded. Within the operation range, the cantilever of the AFM probe behaves as a linear spring. Therefore, the force applied to the sample by the AFM probe can be determined by the deflection and spring constant of the AFM probe.

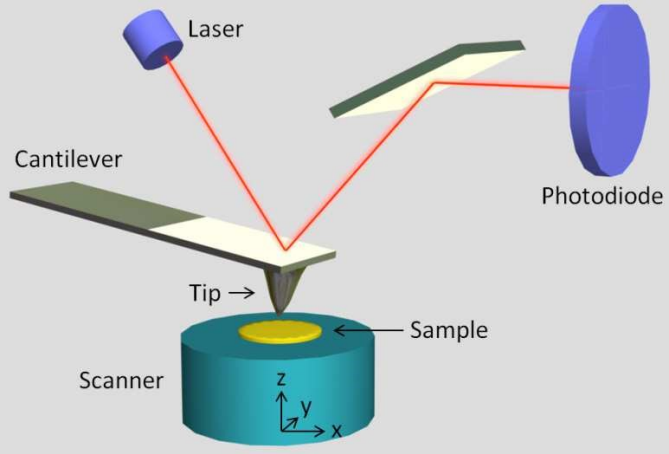

Figure 2-10. Schematic illustration of the working principle of an AFM system. [109]

In this work, AFM measurements were carried out using a Bruker MultiMode AFM and a NuNano Scout 350 LowRes Si-based AFM probe under the ambient condition. The tip radius r_{tip} of the employed AFM probe was measured to be ≈81 nm, as shown in Figure 2-11. AFM operated in contact mode with a setpoint force of ≈25 nN has been used to obtain the topography and thickness of 2D WSe_2. The reason why contact mode instead of tapping mode has been chosen is to provide accurate results for the thickness measurement [110].

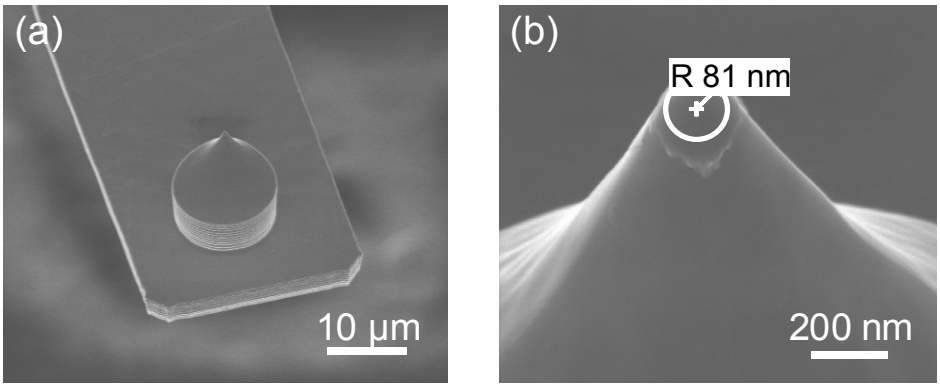

Figure 2-11. SEM images of the AFM probe used for the AFM measurement.

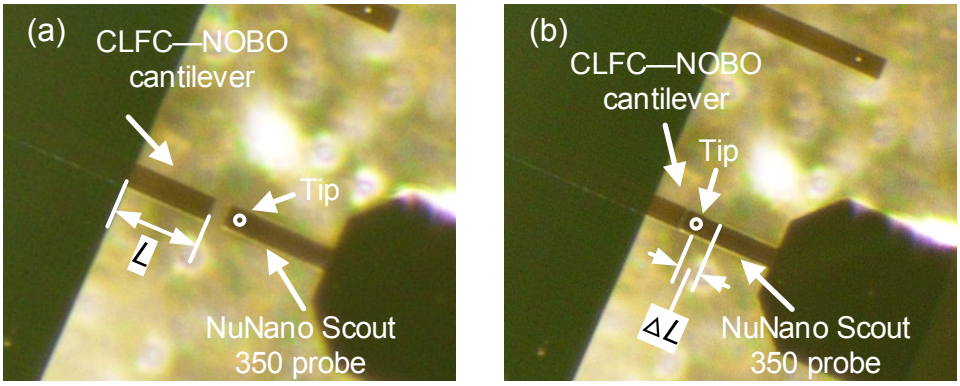

Figure 2-12. Optical images of the reference cantilever and the AFM probe to be calibrated before (a) and during (b) engagement.

The spring constant of the NuNano Scout 350 LowRes AFM probe used has been calibrated via a reference cantilever with a known spring constant (Bruker: CLFC–NOBO) using the method of Ref. [111] described briefly as below: 1) mount the CLFC–NOBO reference cantilever onto the AFM piezo scanner and measure the length L of the reference cantilever, as shown in Figure 2-12a; 2) align the probe to be calibrated (NuNano Scout 350 LowRes) close to the end of the CLFC–NOBO cantilever with certain overlap and measure the offset of the AFM probe tip from the end of the reference cantilever ΔL (Figure 2-12b); 3) engage the AFM probe to the reference cantilever in contact mode and record the AFM probe deflection d and the vertical displacement of the piezo scanner ΔZ. Then the spring constant k of the unknown AFM probe can be derived with the following expression:

$$k = k_{\text{ref}} \left(\frac{\Delta Z}{d} - 1 \right) \left(\frac{L}{L - \Delta L} \right)^3 ,$$

where k_{ref} is the spring constant of the reference cantilever.

2.5 Density functional theory

Density functional theory (DFT) is a computational quantum mechanical modelling method to investigate the ground state structural, magnetic and electronic properties of many-body systems, in particular atoms, molecules, and the condensed phases [112].

For an N-body system, it is practically impossible to solve the Schrödinger equation in which the many-body electronic wavefunction Ψ is a function of 3N variables (the coordinates of all N-atom in the system) due to the substantial computational effort. Therefore, some approximations need to be applied to tackle the problem. In the approximation given by the DFT supported by the Hohenberg-Kohn theorem [113], the electron density $n(r)$ as a function of three variables (x, y, z Cartesian directions) is treated as the central variable rather than the many-body wavefunction. Thus, the Hamiltonian and all ground state properties are determined solely by the electron density. Here the Kohn-Sham [114] formulation of DFT, one of the most successful and state-of-the-art methods in electronic structure theory, is considered. The formulation maps fully interacting system of N-electron onto a fictitious auxiliary system of N non-interacting electrons moving within an effective Kohn-Sham potential $\upsilon_{KS}\left[n(r)\right]$, transforming the N-body problem into N sets of single-body problems. Furthermore, $\upsilon_{KS}\left[n(r)\right] = \upsilon_{ext}(r) + \upsilon_{H}\left[n(r)\right] + \upsilon_{xc}\left[n(r)\right]$, where $\upsilon_{ext}(r)$ is the external potential due to positively charged nuclei, $\upsilon_{H}\left[n(r)\right]$ is the Hartree potential, and $\upsilon_{xc}\left[n(r)\right]$ is the exchange-correlation potential. Thus, electron density $n(r)$ can be obtained by solving the Kohn-Sham equations of the auxiliary noninteracting system iteratively as below:

$\left(-\frac{1}{2}\nabla^2 + \upsilon_{KS}\left[n(r)\right] \right) \varphi_i(r) = \varepsilon_i \varphi_i(r)$, where $n(r) = \sum_i^N \left|\varphi_i(r)\right|^2$.

Once the electron density $n(r)$ is calculated, the corresponding energies, potentials, electronic properties, and etc. can be further derived.

In this project, the DFT calculations implemented with the Quantum Espresso simulation package [115, 116] have been performed on a high-performance computer cluster (Eddie Mark 3). Ultrasoft pseudopotentials with nonlinear core-correction [117, 118] have been used to describe the electron-ion interaction $\upsilon_{ext}(r)$, and the electron exchange-correlation $\upsilon_{xc}\left[n(r)\right]$ has been accounted using the generalized gradient approximation (GGA) with the Perdew-Burke-Ernzerh (PBE) functional [119]. The van der Waals interaction between the atomic layers of WSe_2 has been taken into consideration by the DFT + D3 (Grimme) approach [120]. The unit cells have been employed with periodic boundary conditions in all directions, and a 20 Å vacuum spacing has been introduced in the *c*-axis direction of each 2H-WSe_2 slab to avoid the artificial coupling between adjacent imaged slabs. The cutoff energy is set to 55 Ry for wave function and 440 Ry for charge density and potential. In the self-consistent field calculation, the Brillouin zone has been sampled with Monkhorst-Pack grids [121] of 8 × 8 × 2 and 8 × 8 × 1 k-point for bulk and few-layer WSe_2, respectively. While non-self-consistent calculations have been performed with well converged denser k-point grids of 30 × 30 × 7 and 60 × 60 × 1 for bulk and few-layer WSe_2, respectively. Note that several convergences tests have been conducted (not shown here) to ensure the accuracies of the computations with the chosen cutoff energy and k-point grid. In addition, the calculated crystal structure bulk WSe_2 and band gap of monolayer WSe_2 are in agreement with the reported experimental values [10, 122, 123], confirming the validity of the calculation methods and parameters applied, whose details can be found in Section 6.2.2 and Section 6.2.3.

Chapter 3 Fabrication and electrical characterization of WSe_2 FETs

3.1 Introduction

So far, several methods have been developed to prepare 2D TMDs, which can be classified into top-down and bottom-up approaches generally. The top-down method mainly consists of mechanical and liquid-based exfoliation from bulk crystals [124, 125], while the bottom-up approach is implemented by chemical vapour deposition (CVD) [126] in principle. Although the bottom-up approach is advantageous for large-scale preparation of 2D materials [107, 127-129], the mechanical exfoliation method can produce 2D flakes with better crystal quality and purity [11, 124]. Therefore, from the perspectives of fundamental research and financial cost, the mechanical exfoliation method still prevails. However, other characteristics associated with the exfoliated 2D material sheets are the small size (typically in the micron range), random distribution of the sheets on substrates, as well as irregular shape of the sheets. Such features of exfoliated 2D sheets pose challenges to device fabrication, mainly in two aspects: patterning of the 2D materials and alignment of metal contacts to the patterned 2D sheets.

Thus far, most researchers try to avoid patterning the exfoliated 2D materials but fabricate electronic devices on as-exfoliated pristine 2D materials instead, which makes the dimension of the devices hard to control and limits the practical application of such kind of devices. In addition, currently, electron beam lithography (EBL) is the dominant patterning technique in the nanofabrication field. However, the EBL technique owns some drawbacks. For instance, EBL is a serial process that can take a long time to expose the photoresist (PR). Moreover, the electron beam irradiation can induce defects (e.g., vacancies, as shown in Figure 3-1) in the 2D sheets [130-132], which may degrade the electrical properties, including conductivity and mobility, of the 2D materials, as depicted in Figure 3-2 [133, 134].

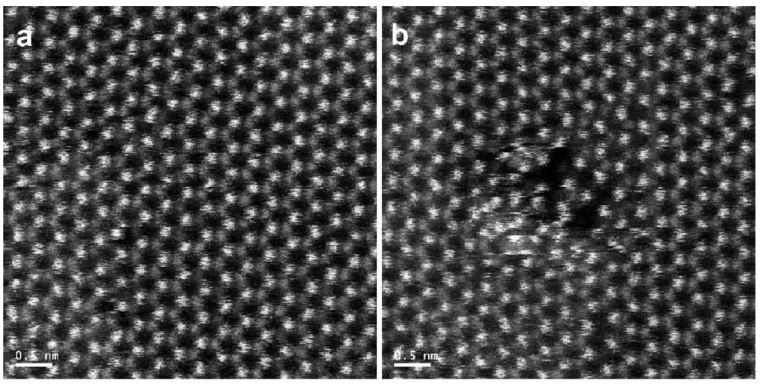

Figure 3-1. Atomic resolution high-angle annular dark field (HAADF) images of pristine monolayer MoS_2 before (a) and after (b) consecutive scans with primary beam energy of 60 keV, showing vacancy formation. [131]

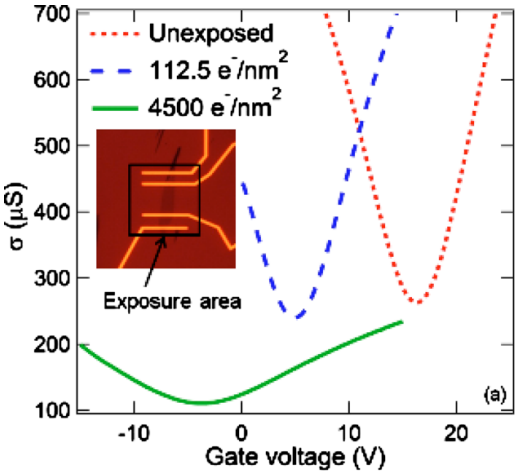

Figure 3-2. Measured graphene conductivity as a function of back gate voltage after various doses of electron-beam irradiation when the source-drain current I_{DS} is 100 nA. After electron exposure, the conductivity and field-effect mobility of graphene get degraded. [133]

In addition, some studies have found out that when some of the 2D materials are suspended, the electrical performance of the characterized 2D materials can be improved [135-137]. Upon suspension from the substrate, the mobility of graphene can be increased by a factor of 10 (from ≈25,000 to ≈230,000 $cm^2\ V^{-1}\ s^{-1}$) [135]. For monolayer MoS_2, the suspended structure has been reported to show increasing mobility from 0.1 to 0.9 $cm^2\ V^{-1}\ s^{-1}$ and an order of magnitude increase in the on/off ratio, as shown in Figure 3-3. However, thus far, the investigation of the electrical transport properties of suspended WSe_2 is still absent. Therefore, it is necessary to

conduct a comparison of the substrate-supported and suspended WSe_2 in the aspect of electrical properties.

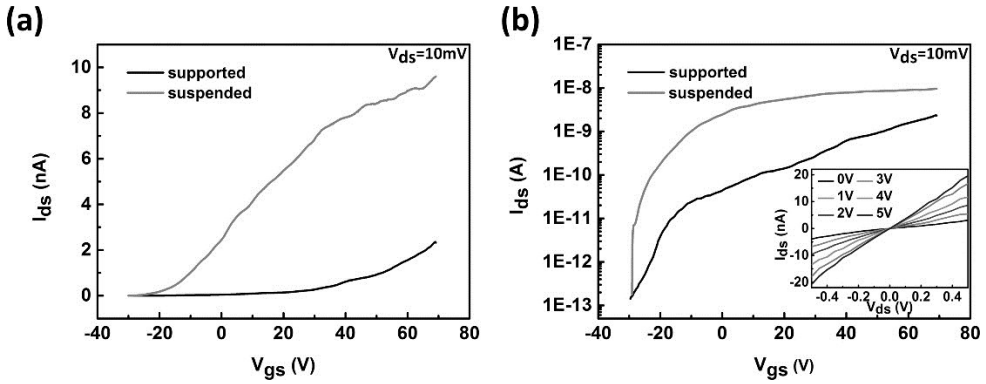

Figure 3-3. Electrical transport measurements of a monolayer MoS_2 FET before and after suspension. I_{ds}–V_{gs} curves in linear scale (a) and log scale (b). [136]

In this chapter, fabrication of field-effect electronic devices from exfoliated 2D WSe_2 using optical lithography has been developed. The advantage of employing optical lithography lies in the low cost of the process, fast speed of exposure, and ease of patterning. The detailed fabrication process of a substrate-supported 2D WSe_2 FET with optical lithography will be elaborated in Section 3.2.1. Then a suspended 2D WSe_2 FET has been successfully fabricated using the vapour HF etching method, as described in Section 3.2.2. Afterwards, two- and four-terminal electrical characterizations have been conducted on the fabricated substrate-supported and suspended WSe_2 FETs to investigate the influence of field-effect, WSe_2/metal contact resistance, and substrate support on the electrical performance of the FETs, as presented in Section 3.4.

3.2 Fabrication of 2D WSe_2 FET with optical lithography

3.2.1 Fabrication of substrate-supported WSe_2 FET

The following section demonstrates the optical lithography technique being applied to the fabrication of field-effect electronic devices with patterned 2D WSe_2 sheets as the conductive channels. Figure 3-4 shows the photomask design for the fabrication of

WSe_2-based FETs. The photomask in Figure 3-4a has been used to mark different areas of the substrates with a spacing of 320 × 320 μm so that the desired exfoliated 2D sheets can be traced via the label arrays. The irregular 2D WSe_2 flakes can be patterned into a desired shape with the photomask in Figure 3-4b. A pair of cross alignment marks in Figure 3-4b has been used to align the pattern in Figure 3-4c to Figure 3-4b. Figure 3-4d shows how the different layers of photomasks (Figure 3-4b and Figure 3-4c) are incorporated together.

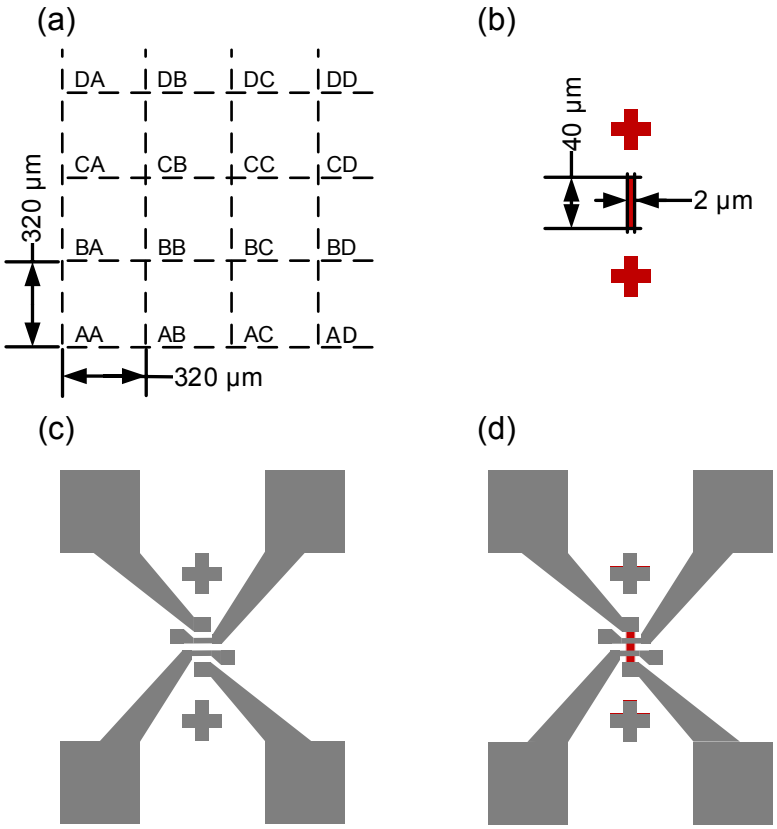

Figure 3-4. (a) Label arrays for marking different areas of the substrates. (b) Photomask design for patterning of the channels of WSe_2 FETs. (c) Photomask design for metal contacts deposition of WSe_2 FETs. (d) The photomasks in (b) and (c) aligned together for WSe_2 FETs fabrication.

The detailed fabrication processes of a WSe_2 back-gated FET (highly-doped Si substrate and SiO_2 serve as the back-gate electrode and gate dielectric, respectively) are described as below. Firstly, label arrays (Figure 3-4a) have been defined on a 3-inch SiO_2/Si wafer by 20 nm deep etching into the SiO_2 layer with the reactive ion

etching (RIE) technique. Then the wafer has been diced into 1 × 1 cm^2 squares. After cleaning of the diced substrates with acetone and O_2 plasma, 2D WSe_2 sheets have been exfoliated mechanically from bulk WSe_2 with Scotch tapes and transferred onto the diced substrates with a PDMS stamp as presented in Section 2.1. Once the 2D WSe_2 sheets have been identified by optical microscope according to their colour contrast [84, 138, 139], the locations of the 2D sheets on the substrates have been recorded by the pre-patterned labels they are close to.

Afterwards, the 2D WSe_2 channel of the FET has been patterned and defined, as follows (Figure 3-5). After a layer of positive photoresist (SPR 350) has been spin coated on the substrate, the photomask in Figure 3-4b has been aligned to the desired 2D WSe_2 flake with the help of Karl Suss MA/BA8 Mask Aligner. After the photoresist exposure and developing, the etch mask with 2 μm in width and 40 μm in length for the channel patterning has been formed (Figure 3-5a). Then, vapour XeF_2 at the pressure of 2 Torr has been used to remove the unmasked areas of the WSe_2 sheets (Figure 3-5b). Afterwards, alignments marks (a pair of crosses) have been defined in SiO_2 with the CHF_3/Ar plasma etching of ≈25 nm SiO_2 (Figure 3-5c). After this, the sample has been treated with O_2 plasma for 10 min to remove the fluorocarbon crust covering the photoresist caused by the fluorine-based plasma etching in the previous step. Then, the photoresist has been thoroughly stripped by acetone, after which the patterned channel of the WSe_2 FET has been formed, and alignment marks have been transferred into SiO_2, as shown in Figure 3-5d.

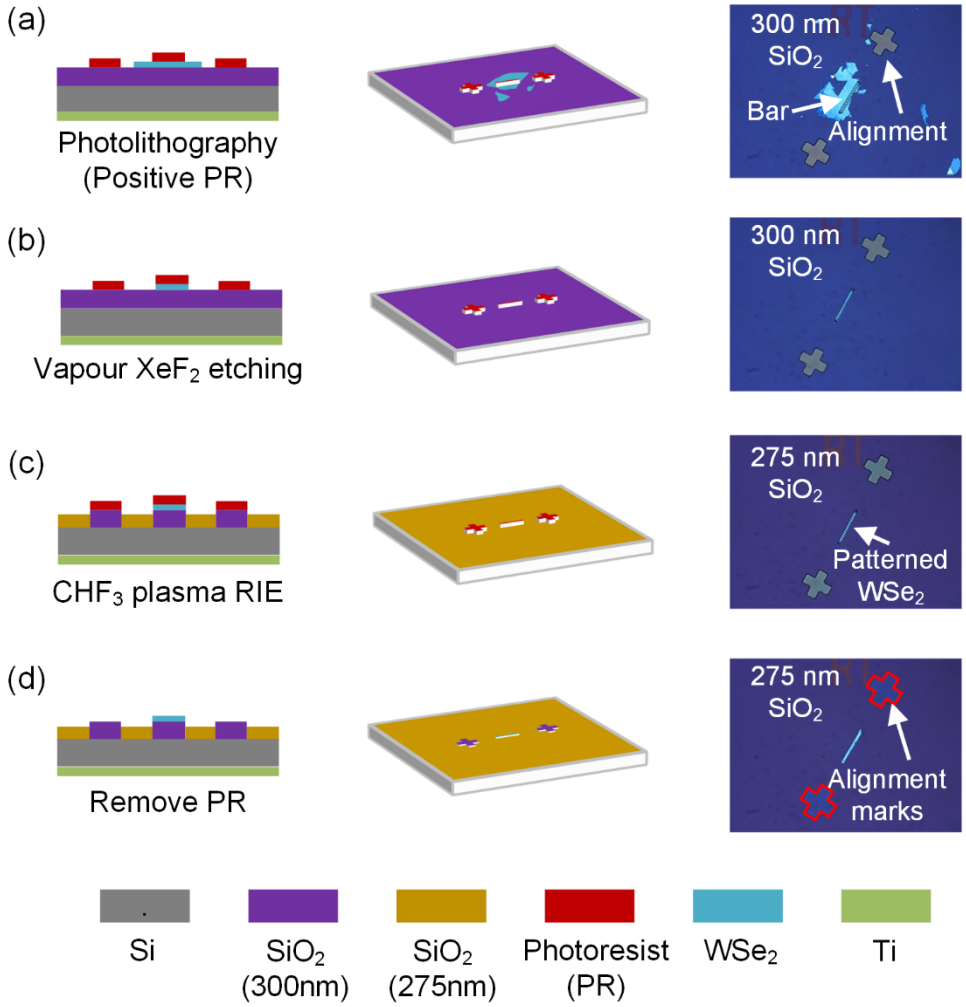

Figure 3-5. Cross-section (left column), 3D (middle column) schematics, and optical images (right column) of the processes of patterning a WSe_2 flake (a, b) and defining alignments marks on a SiO_2/Si substrate (c, d).

For the subsequent drain (D) and source (S) contacts fabrication, the regions of metal contacts (Figure 3-4c) have been defined in the negative photoresist AZ 2035 using photolithography (Figure 3-6a) with the help of alignment marks in SiO_2 formed in the previous processes. Afterwards, Ti (30 nm)/Al (200 nm) metal stack has been deposited through an e-beam evaporation system (Figure 3-6b) and lifted-off in acetone solvent (Figure 3-6c). After the metal deposition, the device has been wire bonded to a chip carrier for further electrical characterization (Figure 3-6d).

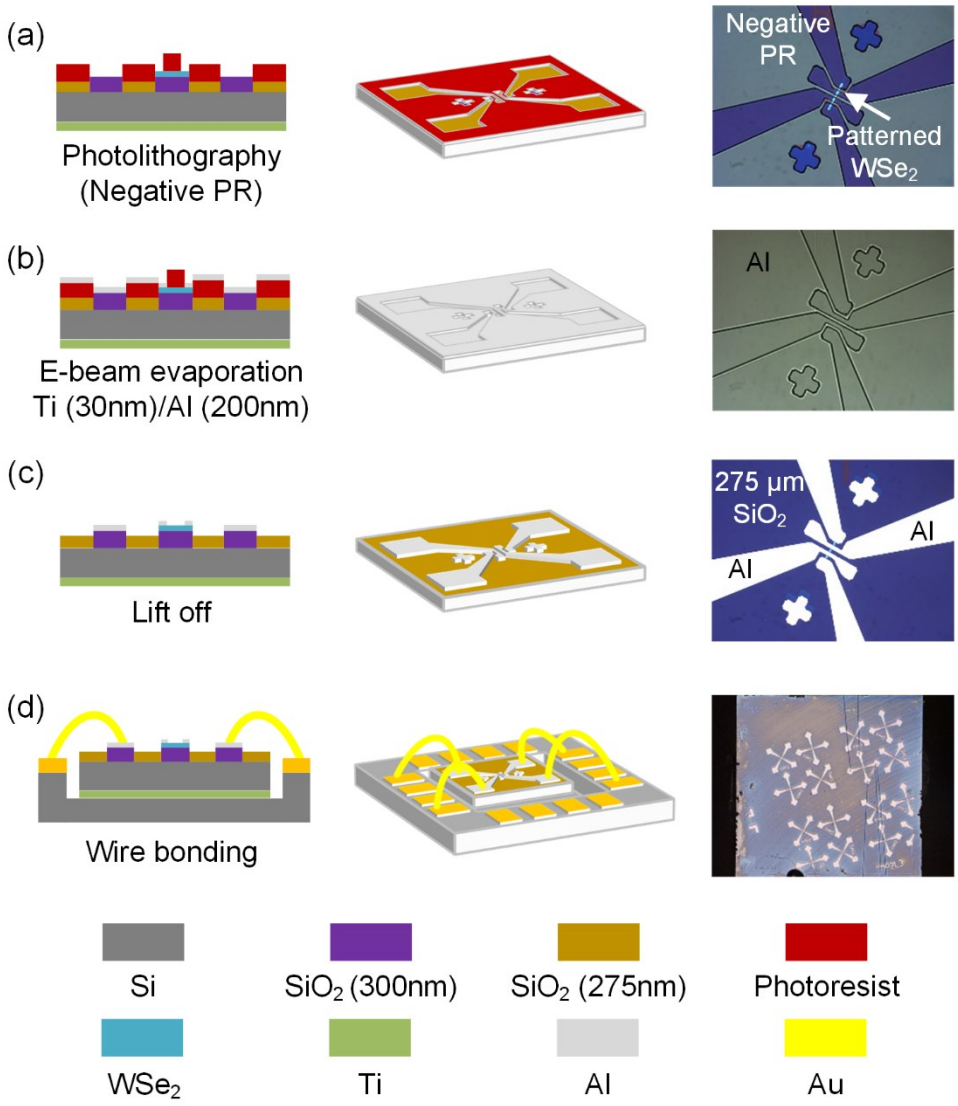

Figure 3-6. Cross-section (left column), 3D (middle column) schematics, and optical images (right column) of the processes of metal contacts deposition (a-c) and subsequent wire bonding (d).

3.2.2 Fabrication of suspended WSe_2 FET

In order to make a suspended channel transistor, the SiO_2 supporting the WSe_2 channel needs to be removed. Here, dry vapour HF etching has been employed to remove the underneath SiO_2 by the chemical reaction of

$$SiO_2 + 4HF(g) \xrightarrow{H_2O} SiF_4(g) + 2H_2O.$$

The main reasons why vapour HF etching is selected here are as below: 1) isotropic etching so that lateral undercut can be made beneath the WSe_2 channel; 2) stiction free

etching which is helpful to prevent the fragile WSe_2 channel from collapsing during its releasing process; 3) compatibility with most of metals, especially the Ti/Al metal stack used in this experiment. The schematics in Figure 3-7 give a brief description of the vapour HF etching process of SiO_2 for a WSe_2 FET. At the initial stage (Figure 3-7b), the HF mainly etches the exposed SiO_2 (the area without any masking by the 2D WSe_2 channel or metal contacts). When the exposed SiO_2 is almost cleared (Figure 3-7c), vapour HF starts to undercut the SiO_2 masked by the WSe_2 channel and metal contacts in a higher etching rate. During this process, a careful control of etching time needs to be taken so that the removal of SiO_2 beneath the channel can be completed and meanwhile, sufficient SiO_2 is left beneath the Ti/Al metal layer to support the metal contacts (otherwise the metal layer will fall onto contact with the Si substrate resulting in the short-circuit between the drain/source electrodes and Si back-gate electrode).

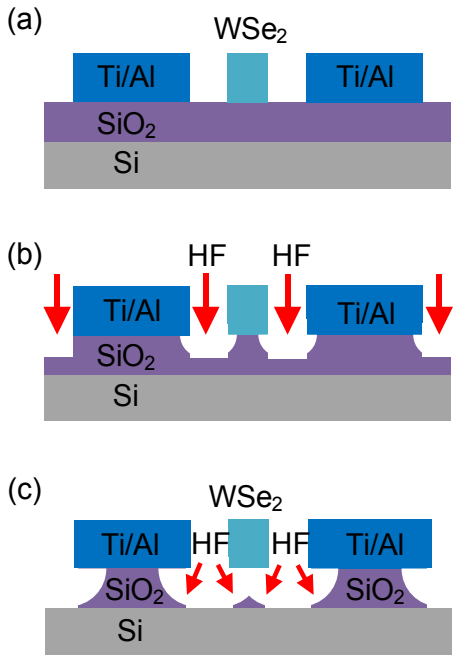

Figure 3-7. Schematic description (not to scale) of vapour HF etching processes of SiO_2: (b) vapour HF mainly etches the exposed SiO_2; (c) vapour HF undercuts the masked SiO_2.

Figure 3-8 shows the optical images of a WSe_2 FET device before and after vapour HF treatment for different times. After 5 min vapour HF etching, the exposed (unmasked) SiO_2 has been thinned to 55 nm from 300 nm, as shown in Figure 3-8b.

When the etching time reaches 6 min (Figure 3-8c), SiO_2 near the edge of the WSe_2 channel and Ti/Al metal contacts has been removed entirely making the bottom Si substrate exposed. Meanwhile, the WSe_2 channel becomes optically invisible originating from the complete removal of SiO_2 beneath the channel. Note that ultrathin SiO_2 (≈7 nm) still remains in the areas relatively far from the WSe_2 channel and metal layer. This is because during the etching process the water is a product of the reaction between HF and SiO_2, which also acts as a catalyst for the reaction. The water produced from the vapour HF etching tends to accumulate near the edge of solid structures, which in return leads to a faster speed of SiO_2 etching around the WSe_2 channel and metal layer.

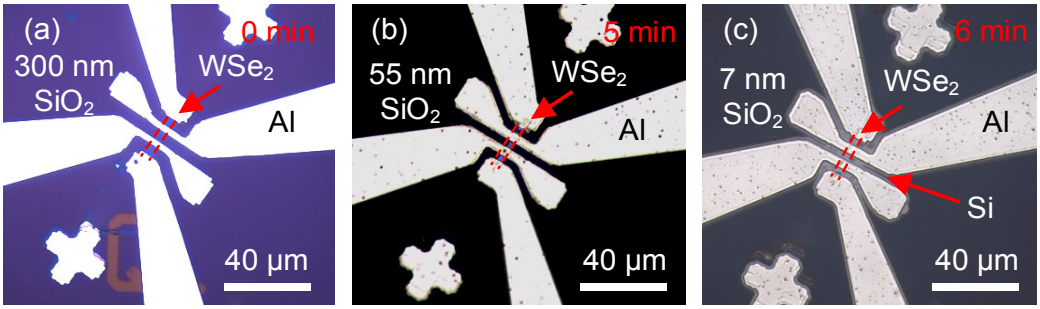

Figure 3-8. Optical images of a WSe_2-based FET before (a) and after vapour HF treatment for 5 min (b) and 6 min (c).

3.3 Configuration of electrical measurements

Electrical measurements on the fabricated WSe_2 FETs were carried out using a Keithley 4200-SCS semiconductor parameter analyzer at room temperature within a shielded probe station in ambient air. During the tests, two- and four-terminal measurements have been employed for different purposes. Figure 3-9 shows the schematics of two- and four-terminal electrical measurements. For two-terminal measurement, a voltage V_{DS} is applied to the inner drain (D) and source (S) electrodes of the transistor then the current I_{DS} flowing across the same electrodes is measured (Figure 3-9a). To measure the intrinsic resistance of the channel, a voltage is applied through an outer pair of electrodes while the current I_{DS} flowing across the outer electrodes and voltage drop V^*_{DS} across the inner drain (D) and source (S) electrodes are measured (Figure 3-9b). Thus, the intrinsic channel resistance can be extracted by

$R_{channel} = V^*_{DS}/I_{DS}$, and the total drain-source resistance including channel resistance and contact resistance is $R_{total} = V_{DS}/I_{DS}$. When the gate voltage V_{GS} applied for two- and four-terminal measurements is same, the contact resistance can be determined by $R_{contact} = R_{total} - R_{channel}$.

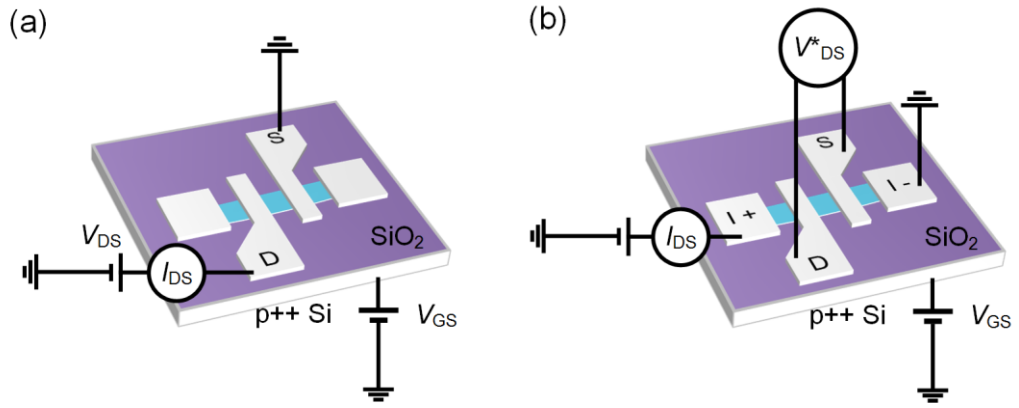

Figure 3-9. Schematics (not to scale) of electrical measurements of two-terminal (a) and four-terminal (b) resistance of a FET.

3.4 Electrical characterization of 2D WSe_2 FETs

3.4.1 Comparison of two- and four-terminal measurements

As the Fermi level of Ti with a low work function of ≈4.3 eV lies between the conduction band minimum (CBM, −4.2 eV) and valence band maximum (VBM, −5.1 eV) of WSe_2 but closer to the CBM [140-143], an n-type Schottky barrier should form at the interface between Ti and semiconducting WSe_2. The n-type Schottky barrier height Φ_{SB} can be defined as the difference between the interfacial conduction band edge E_C and Fermi level E_F, as annotated in Figure 3-10c, d. Therefore, a WSe_2-based transistor can be modelled as two back-to-back n-type Schottky diodes connected with a WSe_2 resistor in series, as shown in Figure 3-10a. When a positive drain bias V_{DS} is applied, the diode near the drain side is forward-biased (many thermally excited electrons in the semiconductor that are able to pass over the barrier), while the other one close to the source side is reverse-biased (few excited electrons in the metal have enough energy to surmount the barrier). Compared to the forward-biased diode, the reverse-biased diode possesses a higher contact resistance $R_{contact}$

relatively and thus plays a more significant role in the electrical transport performance of the device.

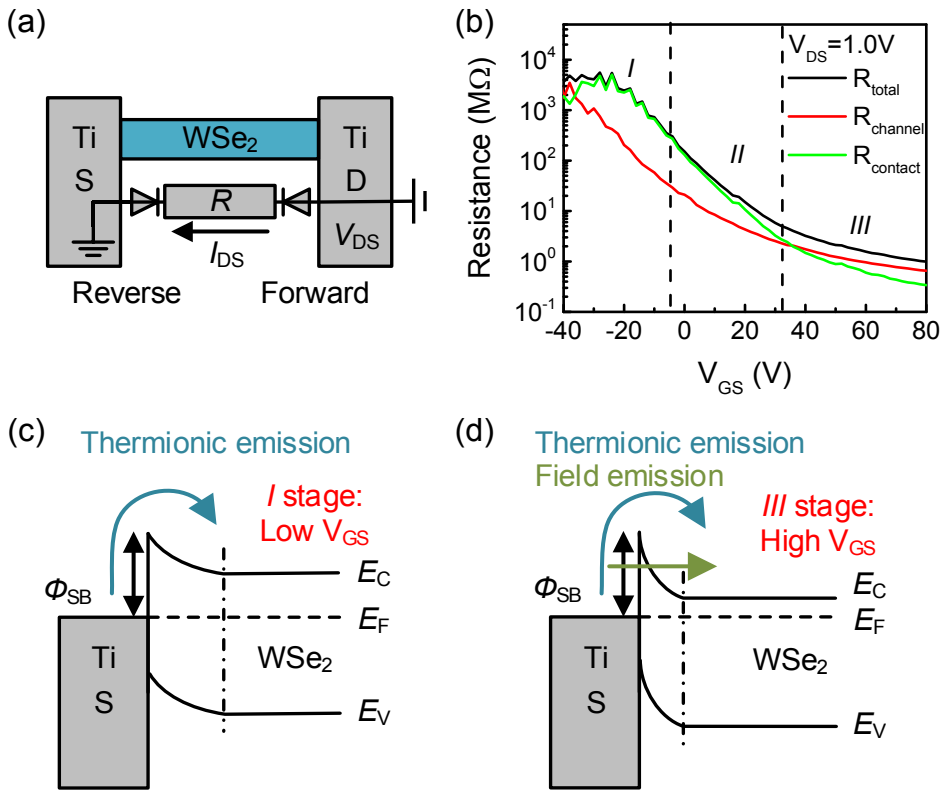

Figure 3-10. (a) Schematic of the equivalent circuit of a WSe_2-based FET. (b) The resistance of the whole FET (black), WSe_2 channel (red), and Ti/WSe_2 metal contact (green) as a function of gate voltage V_{GS}. The band diagram of the Ti/WSe_2 metal contact at low (c) and high (d) gate voltage V_{GS}.

The plots in Figure 3-10b shows the dependence of the resistance of the WSe_2-based FET (Figure 3-6) on the gate voltage V_{GS} with a positive fixed drain bias V_{DS} = 1.0 V. The black curve represents the resistance of the whole device R_{total} obtained from the two-terminal measurement, while the red curve corresponds to the WSe_2 channel resistance $R_{channel}$ measured with the four-terminal configuration. Then the contact resistance $R_{contact}$ (green plot) can be derived as mentioned in Section 3.3. As can be seen, when the gate voltage V_{GS} is small (stage *I* annotated in Figure 3-10b), the contact resistance $R_{contact}$ is much larger than the channel resistance $R_{channel}$, indicating that the overall device performance is dominated by the contact resistance $R_{contact}$. In this stage,

the electrons are injected from the source electrode mainly by the mechanism of thermionic emission, as illustrated in Figure 3-10c. As the gate voltage V_{GS} increases, the Schottky barrier becomes thinner resulting in significant increase in the tunnelling current (Figure 3-10d), which makes contact resistance $R_{contact}$ reduce even in a faster speed than the channel resistance $R_{channel}$. Eventually, in stage *III*, the contact resistance $R_{contact}$ becomes smaller than the channel resistance $R_{channel}$, and the device performance starts to be dominated by the channel resistance $R_{channel}$. From the above measurement results, it can be concluded that the Schottky contact resistance $R_{contact}$ might degrade the overall electrical performance of a device, especially when the gate voltage V_{GS} is in a low value for an n-type Schottky contact. In order to extract the intrinsic electrical property of WSe_2, the four-point measurement should be employed where possible.

3.4.2 Comparison of substrate-supported and suspended WSe_2 FETs

As the electrical performance of 2D materials has been reported to be affected by the 2D crystal/substrate interface (such as the Coulomb scattering by chemical residues or trapped charges) [144-151], it is essential to explore effect of the WSe_2/SiO_2 related interface on the performance of the fabricated WSe_2 FETs. In this section, the electrical transport properties of an 11-layer WSe_2 FET before and after removal of the beneath SiO_2 by vapour HF (Figure 3-8) have been characterized with the four-terminal configuration comparatively.

The top two graphs in Figure 3-11 show the transfer characteristics of the WSe_2 FET under various drain bias V_{DS} measured before (Figure 3-11a) and after (Figure 3-11b) suspension of the WSe_2 channel. Both devices exhibit n-type semiconducting behaviours, which could be contributed from the Se vacancy defects in WSe_2 [101, 152]. Interestingly, the threshold shifts downwards in voltage after the WSe_2 channel is suspended, which is similar to the reported results of suspended MoS_2 FET [136]. It is supposed that the dangling bond on SiO_2 surface induces an extra doping effect on WSe_2, and hence removal of the SiO_2 results in the observed threshold shift. When the gate voltage V_{GS} ranges from −80V~80V, for the substrate-supported WSe_2 FET, the on/off ratio is extracted to be approximately 10^4, while after the WSe_2 channel is

released, the on/off ratio is improved to ≈2 × 10^4. Figure 3-11c, d compare the output characteristics of the substrate-supported and suspended WSe_2 FET under different gate voltage V_{GS}. The I_{DS}–V_{DS} curves from both devices are symmetric and display linear behaviours at low drain voltages V_{DS} regardless of the value of V_{GS}, due to the elimination of the influence of contact resistance by employing the four-terminal configuration.

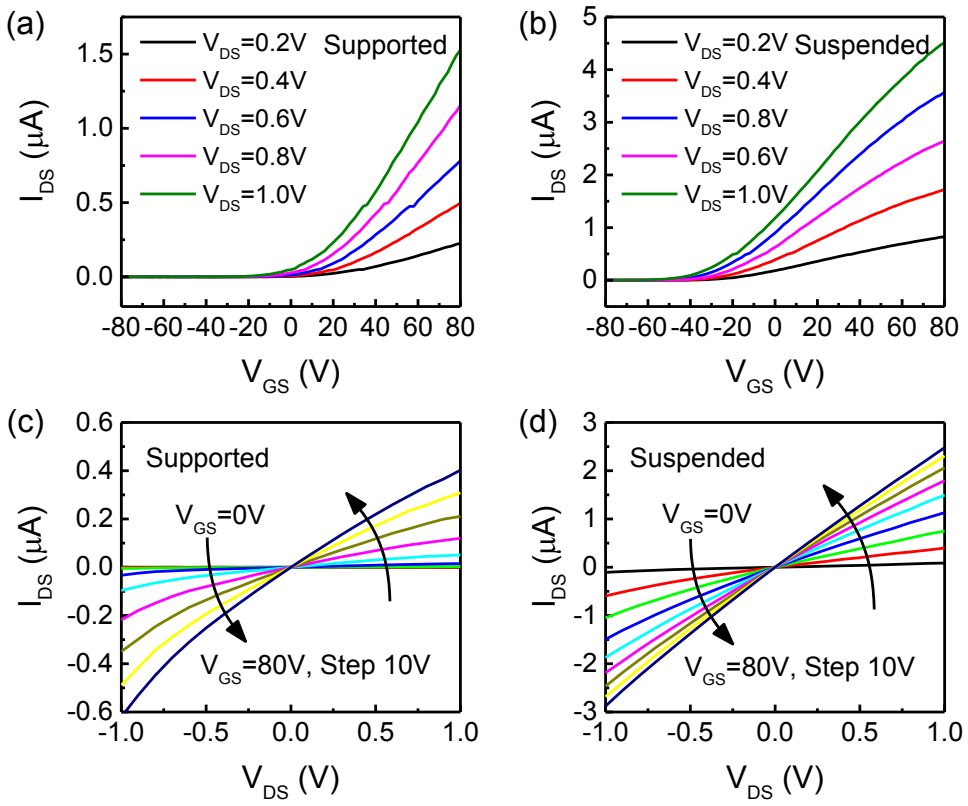

Figure 3-11. Transfer characteristics of an 11-layer WSe_2 FET under several drain voltage V_{DS} before (a) and after (b) the suspension of the WSe_2 channel. Output characteristics of the substrate-supported (c) and suspended (d) WSe_2 FETs under different gate voltage V_{GS}.

By using the equation $\sigma_s = I_{DS}/V_{DS} \times L/W$, where $L = 5$ μm and $W = 2$ μm are the length and width of the conductive channel, respectively, the sheet conductivity σ_s of WSe_2 can be extracted. The mobility μ can be further derived using the equation $\mu = (d\sigma_s/dV_{GS}) \times (1/C_{ox})$, where $C_{ox} = 11.5 \times 10^{-9}$ F cm^{-2} is the capacitance between the WSe_2 channel and back gate per unit area ($\varepsilon_0\varepsilon_{ox}/d_{ox}$; $\varepsilon_{ox} = 3.9$; $d_{ox} = 300$ nm). For the substrate-supported back-gated WSe_2 FET, when $V_{DS} = 1$V and $V_{GS} = -80$V~80V, the

maximum sheet conductivity σ_s and field mobility μ have been measured to be 1.6 μS and 2.7 $cm^2\ V^{-1}\ s^{-1}$, as shown in Figure 3-12a and Figure 3-12b, respectively, which is comparable to one of the previous reports using the same device structure [140]. Note that according to previous reports [100, 153-156], the mobility of WSe_2 FET can be further improved by one order of magnitude by using a thinner gate dielectric with higher dielectric constant (e.g., atomic layer deposited Al_2O_3, ZrO_2, and 2D-hBN), deposition of a passivation layer (e.g., Si_3N_4), and operating in vacuum or low temperature environment. However, the relative comparison of substrate-supported and suspended WSe_2 is the focus here, which can be obtained efficiently using the simplified device structure. After the WSe_2 channel is released from the substrate, increases in both the sheet conductivity σ_s (from 1.6 to 7.4 μS) and field mobility μ (from 2.7 to 25.5 $cm^2\ V^{-1}\ s^{-1}$ in peak value) have been observed.

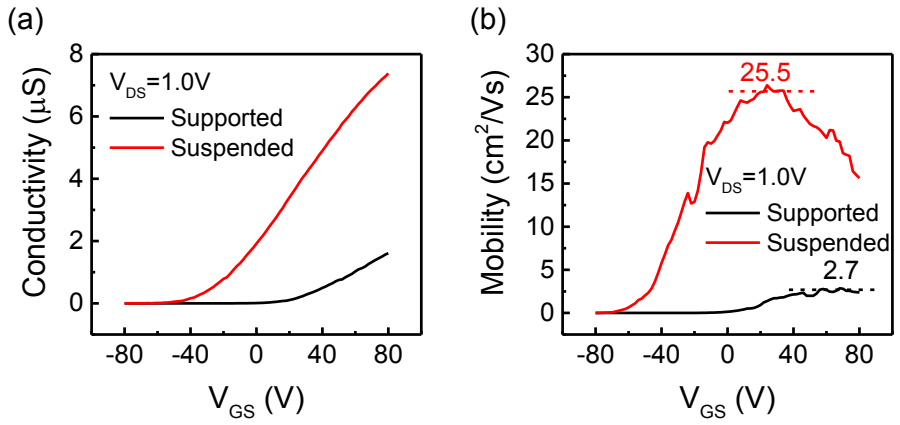

Figure 3-12. The extracted sheet conductivity σ_s (a) and field mobility μ (b) as a function of the gate voltage V_{GS} for the substrate-supported and suspended WSe_2 FETs, respectively.

Figure 3-13a, b show the transfer characteristics of the substrate-supported and suspended WSe_2 FETs with double-direction gate voltage sweeping under various sweep rates. When the gate voltage V_{GS} sweeps in forward (−80 V to 80 V) and reverse (80 V to −80 V) directions under the same sweep rates, threshold voltage shifts forming hysteresis loops can be observed for both the substrate-supported and suspended WSe_2 FETs. Moreover, the width of the hysteresis loop decreases as the sweep rate increases. In addition, the hysteresis loops of the substrate-supported WSe_2 FET have been observed to be broader than those of the suspended WSe_2 FET under

application of a same sweep rate. The graphs of Figure 3-13c, d compare the evolutions of the drain-source current I_{DS} with respect to the measurement time t under a fixed V_{DS} and V_{GS} for the substrate-supported and suspended WSe_2 FETs. Current decaying as the measurement time t increases can be observed in both graphs. In order to evaluate the speed of the current decay quantitively, the data have been fitted with the biexponential equation $I = I_0 + Ae^{-t/\tau_1} + Be^{-t/\tau_2}$, where τ_1 and τ_2 represent two exponential time constants (mean lifetime for the current decay). The extracted time constants of the substrate-supported WSe_2 FET are τ_1 = 7.6 s and τ_2 = 55.6 s (Figure 3-13c), which is three times smaller than that of MoS_2 FET [157]. While after the WSe_2 is suspended, an increase in the time constants (τ_1 = 28.7 s and τ_2 = 277.6 s) has been observed (Figure 3-13d), indicating a slower current decay for the suspended WSe_2 FET.

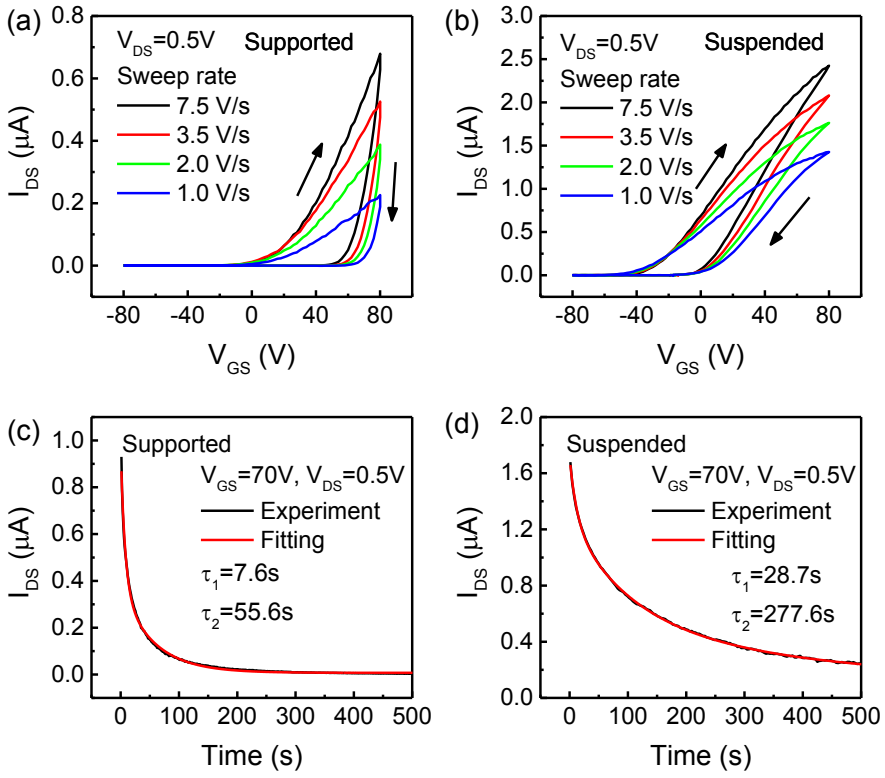

Figure 3-13. The transfer characteristics of the substrate-supported (a) and suspended (b) WSe_2 FETs with double-direction gate voltage sweeping at different sweep rates. Drain-source current I_{DS} versus the measurement time t (black) at a fixed V_{DS} and V_{GS} with the fitted biexponential curves (red) for the substrate-supported (c) and suspended (d) WSe_2 FETs.

Table 3-1. Comparison of the electrical transport properties of the substrate-supported and suspended 11-layer WSe_2 FETs.

Property	**Supported WSe_2 (A)**	**Suspended WSe_2 (B)**	**Ratio (B/A)**
On/off ratio	$\approx 10^4$	$\approx 2 \times 10^4$	2.0
Conductivity (μS)	2.4	7.2	3.0
Mobility ($cm^2\ V^{-1}\ s^{-1}$)	2.7	25.5	9.4
Mean lifetime (s)	$\tau_1 = 7.6$	$\tau_2 = 28.7$	3.8
	$\tau_1 = 55.6$	$\tau_2 = 277.6$	5.0

Table 3-1 summarizes the measured electrical transport properties of the substrate-supported and suspended WSe_2 FETs. Overall, after removal of SiO_2 beneath the WSe_2 channel, the overall electrical performance of the WSe_2 FET has been improved. Note that, as the sheet conductivity σ_s of the gate dielectric, SiO_2 for substrate-supported FET (10^{-28}~10^{-24} μS) and air for suspended FET (10^{-16}~10^{-10} μS), is far smaller than that of the characterized WSe_2 channel presented in Figure 3-12a, the contribution of gate leakage to the electrical performance variation can be negligible. Therefore, it is the WSe_2/SiO_2 interface that affects the electrical performance of the 2D WSe_2 FETs negatively. The potential interface effect can be attributed to several factors below: 1) fabrication residues (e.g., tape residues from the mechanical exfoliation of 2D WSe_2) left over between the WSe_2 and substrate might behave as residual scatters [135, 158]; 2) negatively charged silanol groups (Si–OH) on O_2 plasma cleaned SiO_2 can act as Coulomb scattering centres degrading the mobility [159]; 3) dangling bonds and water adsorbates on the SiO_2 surface supply extra charge trapping states [147, 157, 160, 161], in which case, increasing number of free carriers can get trapped with longer time application of the drain bias V_{DS}, which gives rise to unscreened Coulomb scattering and results in the observed current decay phenomenon [147]. In addition, the occurrences of electron trapping and de-trapping under forward (−80 V to 80 V) and reverse (80 V to −80 V) gate voltage sweeps, respectively, contribute to the observed hysteresis effect [147, 157, 161]. However, to gain a deeper insight into the mechanism

of such interface effects, more systematic studies need to be carried out in the future, such as measuring the electrical performance of the suspended WSe_2 FET in different temperature and pressure. Nevertheless, the measurement result here implies the feasibility of improving the performance of WSe_2 FET by optimizing the quality of the WSe_2/dielectric interface, such as preparing a dielectric layer with smoother and cleaner surface and developing a residue-free transfer method of 2D WSe_2.

3.5 Conclusions

In this chapter, the fabrication of substrate-supported and suspended pre-patterned WSe_2 FETs with the optical lithography and vapour HF etching technology has been developed. Subsequently, two- and four-terminal electrical characterizations have been conducted on the fabricated WSe_2 FETs. In the electrical measurements, 2D WSe_2 FETs exhibit an n-type transport characteristic. In addition, the Schottky barrier formed at the interface of Ti/WSe_2 and the WSe_2/SiO_2 interface can affect the electrical performance of 2D WSe_2 FETs negatively, which indicates that the improvement of the electrical performance of WSe_2 FET can be achieved by optimizing the quality of WSe_2/metal contact and WSe_2/dielectric interfaces. Note that, the fabrication and electrical characterization of the suspended WSe_2 FET are first time reported thus far.

Chapter 4 Layer thinning and p-type doping of WSe_2 by vapour XeF_2

4.1 Introduction

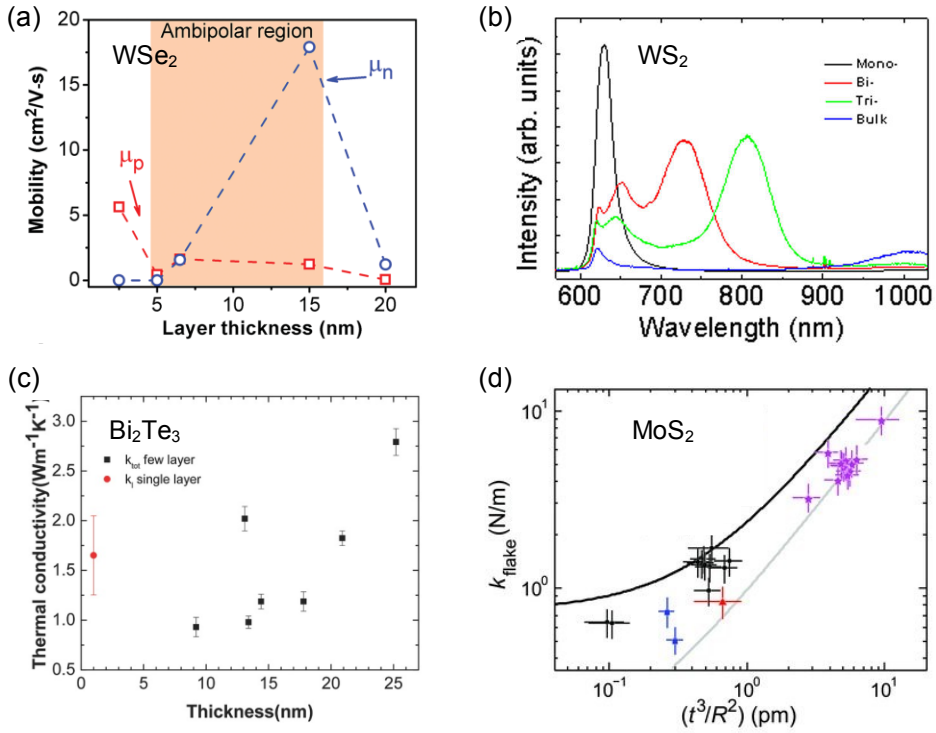

Figure 4-1. (a) Experimentally extracted field-effect mobility of WSe_2 FETs with various thicknesses. [162] (b) Photoluminescence spectra of few-layer and bulk WS_2. [163] (c) Thickness-dependent thermal conductivity of 2D Bi_2Te_3. [164] (d) Elastic constant versus t^3R^{-2} measured for MoS_2 with thickness ranging from 25- down to 5-layer. [162]

Due to the strong surface effects and weak interlayer interaction, the properties of TMDs can vary dramatically with different numbers of layers. Some reports have shown that TMDs exhibit thickness dependent electrical [141, 162, 165-167], optical [31, 89, 163, 168, 169], thermal [164, 170], mechanical [6, 171], and piezoelectrical properties [30, 75], as exampled in Figure 4-1. Therefore, the ability to produce different numbers of TMD layers controllably is highly desirable for tuning the performance of TMDs for various applications. However, none of current preparation

methods of 2D TMDs can achieve good control over the number of layers, which limits the application of 2D TMDs. Moreover, a simple, efficient, and selective patterning approach (complete removal) of TMDs for defining complex structures is desirable for TMD-based very-large-scale integration (VLSI) fabrication.

To date, several methods of TMD thinning (removal of a specified number of layers) and patterning have been reported to tune the number of TMD layers produced. High energy beams, including laser beam and focused ion beam (FIB), have been demonstrated for thinning/patterning of MoS_2 [172, 173]. However, the low efficiency and limited lateral resolution of this approach bring a considerable challenge for large-scale processing. Although thermal annealing assisted thinning can be scaled-up [94, 174, 175], the extremely slow thinning rate and the requirement of high temperature (≥300 °C) to initiate the thinning make the approach incompatible with standard semiconductor fabrication process. Meanwhile, several kinds of plasma (e.g., Ar, O_2, CHF_3, CF_4, and SF_6) [176-178] have been reported to be advantageous at efficient thinning/patterning and good compatibility with conventional complementary metal-oxide-semiconductor (CMOS) technologies. However, the physical crystal damage caused by the ion bombardment inevitably could enhance the possibility of carriers' surface roughness scattering and hence degrade the electrical performance of the thinned TMDs. Furthermore, plasma etching with currently reported recipes also suffers from low selectivity to some of the commonly used dielectrics and metals (e.g., SiO_2, Al_2O_3, HfO_2, and Al) in TMD-based devices. As a result, a thinning method that can overcome the disadvantages of the approaches mentioned above is highly in demand.

Moreover, in order to integrate the TMDs with CMOS logic circuits in future VLSI, both n- and p-type TMD-based FETs need to be fabricated. Therefore, the control of the carrier type and concentration achieved through doping is essential for applications of TMDs in CMOS technologies. Also, the type and height of the Schottky barrier formed at the contact/TMDs interface, which determines the contact resistivity, can be tuned by doping TMDs [155, 179]. Although a lot of research has been conducted on the doping of MoS_2 [180-183], the study of methods for doping WSe_2 is still quite limited [155, 184, 185]. So far, several WSe_2 doping methods using surface adsorption (e.g., NO_2, K vapour, and $Co_6Se_8(PEt_3)_6$ doping) [155, 185, 186] have been reported.

Nevertheless, as shown in Figure 4-2, these doping methods suffer from poor air stability. Hence a doping method for WSe_2 with good air stability, scalability, and controllability still needs to be investigated.

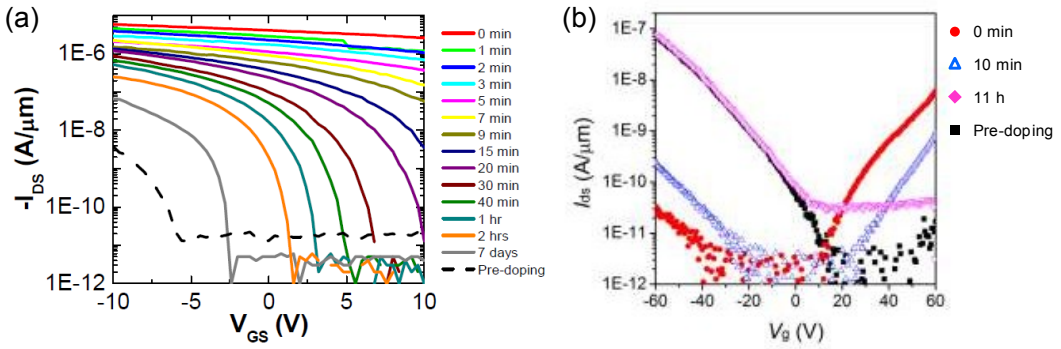

Figure 4-2. Time-dependent I_{DS}–V_{GS} transfer characteristics of the NO_2 (a) [155] and $Co_6Se_8(PEt_3)_6$ [186] (b) doped WSe_2 FET under exposure of ambient air.

In this chapter, a controllable layer thinning and p-doping of WSe_2 with vapour XeF_2 is demonstrated. The thickness and the surface roughness variations of WSe_2 as a function of vapour XeF_2 exposure time and exposure pressure have been characterized using atomic force microscope (AFM) in Section 4.2. The effects of vapour XeF_2 thinning on the surface modification, luminescence properties, and Fermi levels of WSe_2 have been investigated with a combination of Raman, photoluminescence (PL), and X-ray photoelectron spectroscopy (XPS) in Section 4.3 and 4.4. Additionally, the evolution of electrical properties of WSe_2 induced by vapour XeF_2 treatment, including threshold voltage, mobility, and doping concentration, have been studied systematically through the electrical characterization of WSe_2-based FETs in Section 4.6. Afterwards, the chapter ends with the air stability study of the vapour XeF_2 doping in Section 4.7.

4.2 Optical microscope and AFM analysis of XeF_2 treated WSe_2

Firstly, 2D WSe_2 have been exfoliated mechanically from bulk WSe_2 crystals and transferred onto thermally grown SiO_2 (300 nm) on highly p-doped Si substrates. After

cleaning the tap residues, the samples have been treated with XeF_2 (25 sccm)/N_2 (100 sccm) gas in a XeF_2 etcher (memsstar's ORBIS ALPHA system) at the temperature of 20 °C, as shown in Figure 4-3a. When vapour XeF_2 gets in contact with WSe_2, the XeF_2 dissociates into Xe inert gas and F radicals. The F radicals can break the W–Se chemical bonds and react with W and S atoms producing volatile fluorinated W and Se (WF_x and SeF_x), as illustrated in Figure 4-3b. The detailed reaction mechanism will be discussed further in Section 4.4. In Figure 4-4a, b, optical images of a WSe_2 flake before and after XeF_2 treatment under 1 Torr for 60 s have been compared. The colour contrast of the WSe_2 flake, which represents the information of WSe_2 thickness [138, 187], can be seen to change upon vapour XeF_2 treatment. The thicknesses of the WSe_2 flake before and after vapour XeF_2 exposure (represented by *d*' and *d*, respectively) have been determined through AFM analysis (insets of Figure 4-4a, b) and annotated in the corresponding optical images (Figure 4-4a, b). As can be seen, after XeF_2 exposure for 60 s, the thickness of the WSe_2 flake has been reduced by 1.5 nm, which is equivalent to a bilayer of WSe_2 [138].

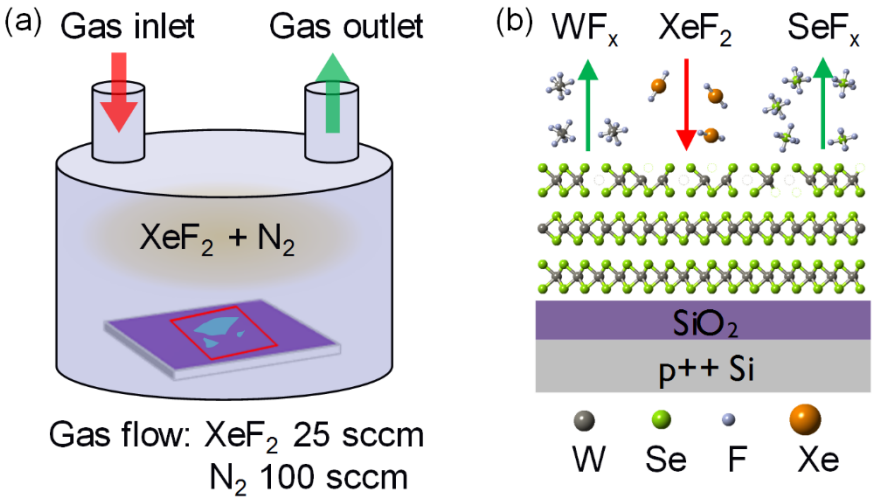

Figure 4-3. Schematics of the experimental setup of the vapour XeF_2 treatment (a) and the chemical reaction of vapour XeF_2 with WSe_2 (b).

Figure 4-4c, d summarize the etched depth $h = d' - d$ and root-mean-square roughness R_{RMS} variation as a function of increasing etching time *t* and etching pressure *P*. The AFM topography images of WSe_2 before and after vapour XeF_2 thinning under various

experimental parameters can be found in Figure 4-5. As shown by the black curve of Figure 4-4c, before 90 s, not much thickness variation is observed, while the etching rate h/t starts to increase significantly after 90 s. In contrast to the change of etching rate, the R_{RMS} value (blue curve in Figure 4-4c) increases quickly before 90 s and is seen to flatten gradually after 90 s. The increase in roughness would result in increased surface area and defect sites hence supplying more reaction sites, which can contribute to an accelerated etching rate as etching time increases.

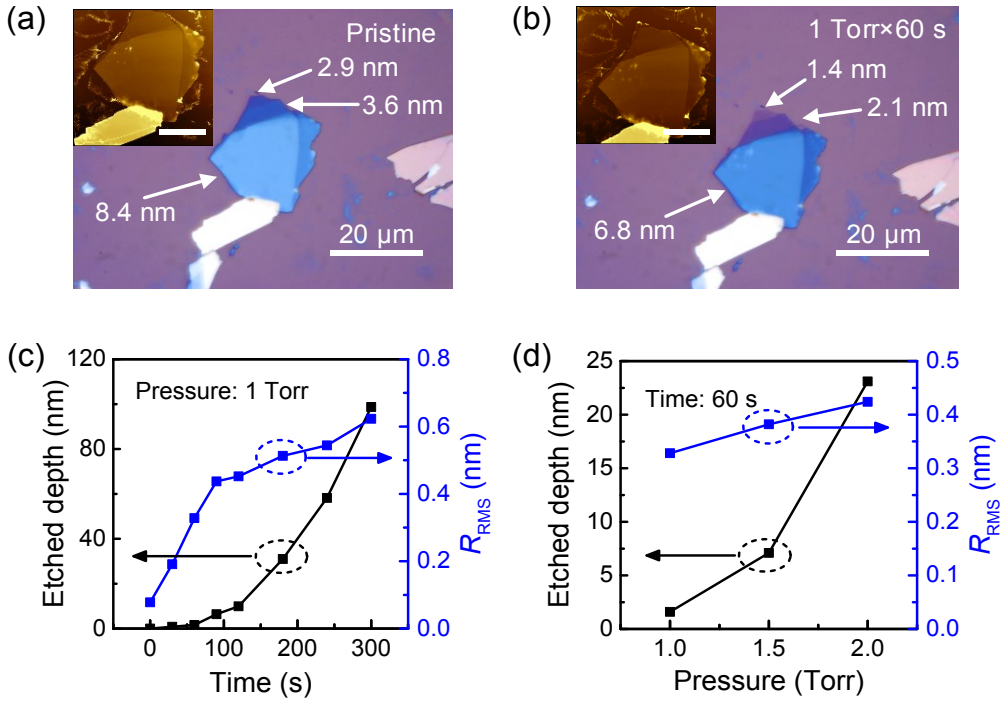

Figure 4-4. Optical images of WSe_2 before (a) and after (b) XeF_2 treatment under 1 Torr for 60 s. Insets are corresponding AFM images of the WSe_2 flake. Scale bars of insets are 10 μm. The etched depth (h, black curves) and root-mean-square roughness (R_{RMS}, blue curves) of WSe_2 versus etching time t under 1 Torr (c) and etching pressure P within 60 s (d). Symbols are measured results, and the solid lines serve as a guide to the eye.

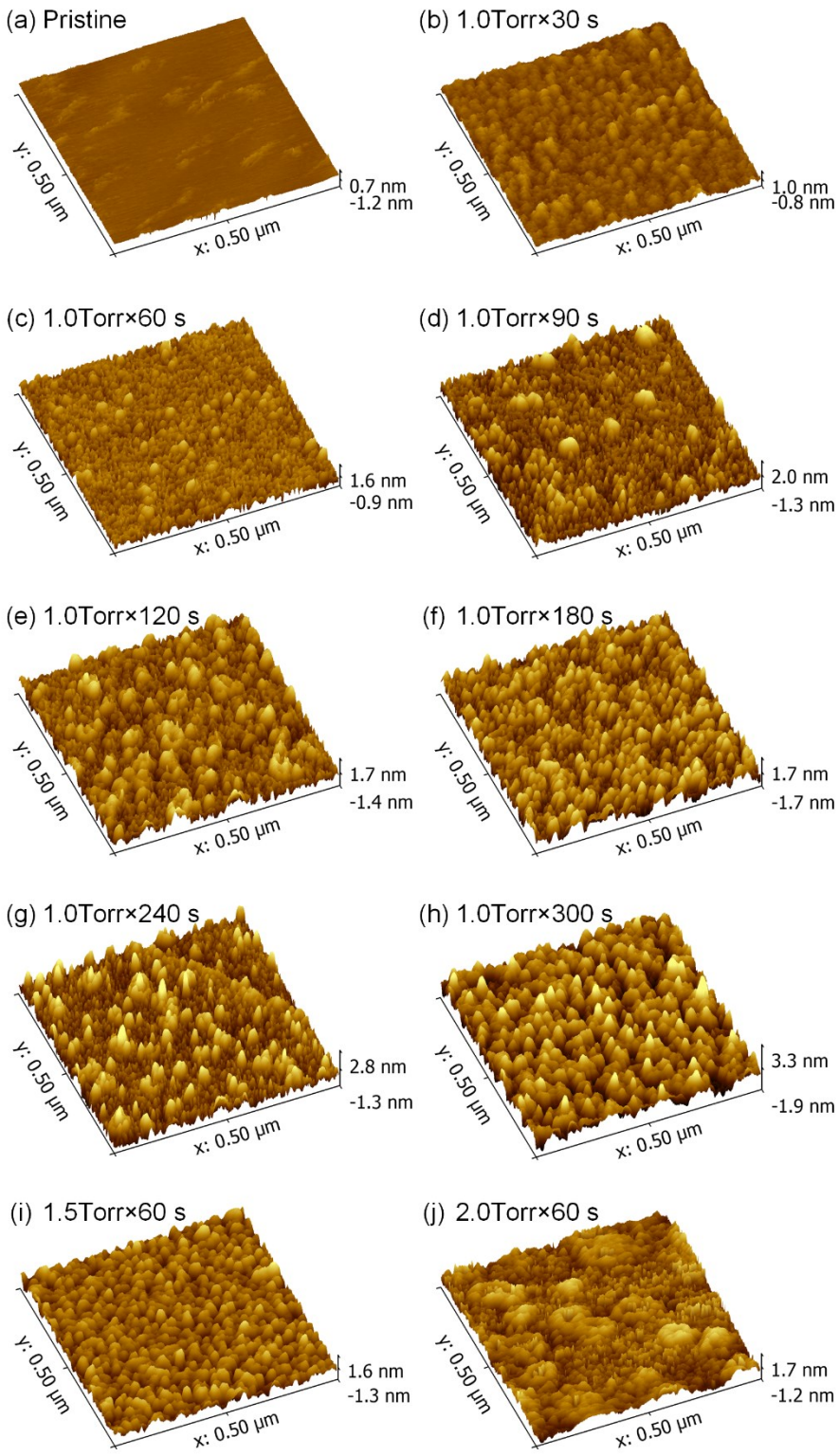

Figure 4-5. AFM topography images of WSe_2 before (a) and after XeF_2 treatment under different exposure conditions: 1.0 Torr for 30 s (b), 60 s (c), 90 s (d), 120 s (e), 180 s (f), 240 s (g), and 300 s (h); 1.5 Torr (i) and 2.0 Torr (j) for 60 s.

Figure 4-4d shows the effect of the exposure pressure on the etched depth and surface morphology during an etching time of 60 s. Both the etching rate and surface roughness show a rising trend when the exposure pressure increases, possibly caused by an increased amount of available etchant (F radicals) with increasing pressure. Notably, the etching rate is observed to increase by one order of magnitude when the exposure pressure is doubled. Therefore, by varying the exposure pressure, the controllability and efficiency of WSe_2 etching can be tuned for different applications easily, i.e., slow speed etching for thinning and fast speed etching for patterning.

Furthermore, the surfaces of WSe_2 with the same etched depth, thinned by vapour XeF_2, are generally smoother than using plasma thinning methods [177, 188, 189], which is crucial to restrain surface scattering and thereby limit the mobility degradation of the etched materials. In addition, vapour XeF_2 thinning is more efficient than FIB, laser, and thermal annealing assisted thinning methods [94, 172-175], and hence easier to scale-up for wafer-level processing. Meanwhile, a highly selective etching of WSe_2 over most dielectrics and metals (e.g., SiO_2, Si_3N_4, Al_2O_3, HfO_2, and Al) can be achieved by using vapour XeF_2 [190].

Figure 4-6 shows an example of layer thinning of 23-layer (Figure 4-6a) and 109-layer (Figure 4-6b) WSe_2 into a monolayer (Figure 4-6c) and a bilayer (Figure 4-6d), respectively, by vapour XeF_2 with appropriate exposure times based on the results in Figure 4-4c. Note that the number of layers of WSe_2 films annotated in Figure 4-6c, d is confirmed further by Raman measurements, which will be explained later. The thicknesses of XeF_2 thinned WSe_2 (1.3 nm for monolayer and 2.1 nm for bilayer), as shown in Figure 4-6e, f, have been found to be larger than those of pristine monolayer (≈0.8 nm) and bilayer (≈1.5 nm) WSe_2 [138]. Moreover, distinct from thinning with thermal annealing methods [94, 174, 191], no etching pits and excellent uniformity in thickness have been observed on vapour XeF_2 thinned WSe_2 (the dots seen in Figure 4-6c, d originate from tape residues beneath the WSe_2 films introduced during the sample preparation process).

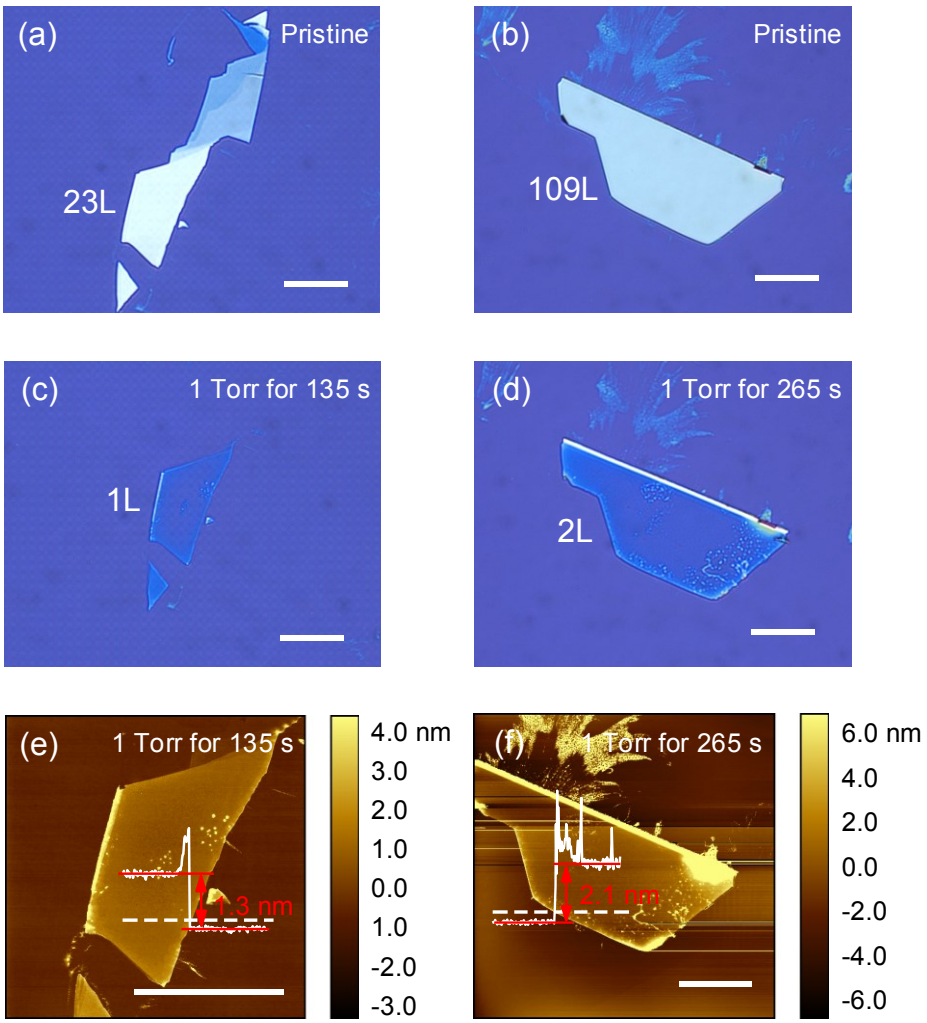

Figure 4-6. Optical images of 23-layer (23L; a) and 109-layer (109L; b) WSe_2 before and after thinned into monolayer (1L; c) and bilayer (2L; d) WSe_2 by vapour XeF_2 under 1 Torr for 135 and 265 s, respectively. (e, f) AFM images of the corresponding WSe_2 in (c) and (d), respectively, with superimposed height profiles along the dashed lines. The scale bars are 20 μm.

4.3 Raman and PL spectroscopy analysis of XeF_2 treated WSe_2

Raman scattering has been conducted to characterize the influence of vapour XeF_2 treatment on the crystal quality of the thinned WSe_2 and determine the number of WSe_2 layers, as shown in Figure 4-7. Note that, the intensity of Raman spectra has been renormalized with reference to the spectra in top row of Figure 4-7a and Figure 4-7b

for clarity. Figure 4-7a compares the Raman spectra of WSe_2 before (5- and 6-layer) and after vapour XeF_2 exposure (3- and 4-layer) under 1 Torr for 60 s. The Raman peaks located at around 249 cm^{-1} and 258 cm^{-1} are attributed to the in-plane vibrational mode (E^1_{2g}) and out-of-plane vibrational mode (A_{1g}), respectively, similar to the reports of [123, 192]. Another Raman peak at 308 cm^{-1} is assigned to the B^1_{2g} mode arising from the presence of interlayer interaction [103], which can be used to distinguish monolayer and multilayer WSe_2. After XeF_2 treatment, blueshifts of the E^1_{2g} mode are observed, and the Raman peak intensities of E^1_{2g} and A_{1g} modes show an increase compared to the spectra of pristine WSe_2, due to the reduction in number of layers, which have also been observed in previous reports [193, 194].

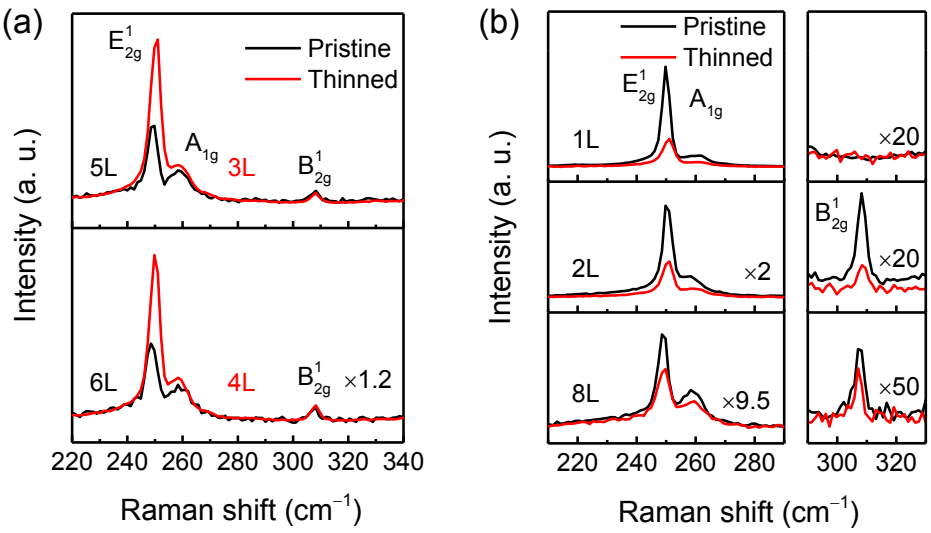

Figure 4-7. (a) Raman spectra of WSe_2 before (5- and 6-layer, black curves) and after XeF_2 treatment (3- and 4-layer, red curves) under 1 Torr for 60 s. (b) Raman spectra of pristine (black curves) and XeF_2 thinned (red curves) WSe_2 in monolayer (1L), bilayer (2L), and 8-layer (8L). For clarity, the intensity of Raman spectra has been renormalized.

Figure 4-7b shows the Raman spectra of pristine WSe_2 (black curves) and vapour XeF_2 thinned WSe_2 (red curves) with the same number of layers. Note that the first two rows (from the top) Raman spectra of thinned WSe_2 in Figure 4-7b are obtained from the samples shown in Figure 4-6c, d, respectively. The thinned WSe_2 in Figure 4-6c is determined to be monolayer because of the absence of the B^1_{2g} mode, as shown in the first row spectrum in Figure 4-7b. The appearance of the B^1_{2g} mode in the second row

Raman spectrum of thinned WSe_2 in Figure 4-7b indicates the presence of multilayer WSe_2 in Figure 4-6d. In addition, the thinned WSe_2 in Figure 4-6d is thicker than the thinned monolayer WSe_2 (Figure 4-6c) by 0.8 nm, which is equal to the interlayer distance of WSe_2 [138], so the WSe_2 film in Figure 4-6d can be determined to be a bilayer WSe_2. In comparison with pristine WSe_2, all of the E^1_{2g} modes of XeF_2 thinned WSe_2 in Figure 4-7b show a similar degree of blueshift (≈1.1 cm^{-1}), regardless of the number of WSe_2 layers, which is likely to be caused by a decrease in free electron concentration (p-doping) [95, 99, 195] after vapour XeF_2 treatment. Moreover, after XeF_2 exposure, no significant change but a slight broadening in the full width at half maximum (FWHM) of the E^1_{2g} peaks (from 3.7 to 4.5 cm^{-1} for monolayer, 3.8 to 4.6 cm^{-1} for bilayer, and 4.0 to 5.3 cm^{-1} for 8-layer) together with the reduction of Raman peak intensities have been observed, which implies that the vapour XeF_2 thinning does not compromise the crystalline quality of WSe_2 at the macroscopic level but introduces some minor defects and/or crystal damages.

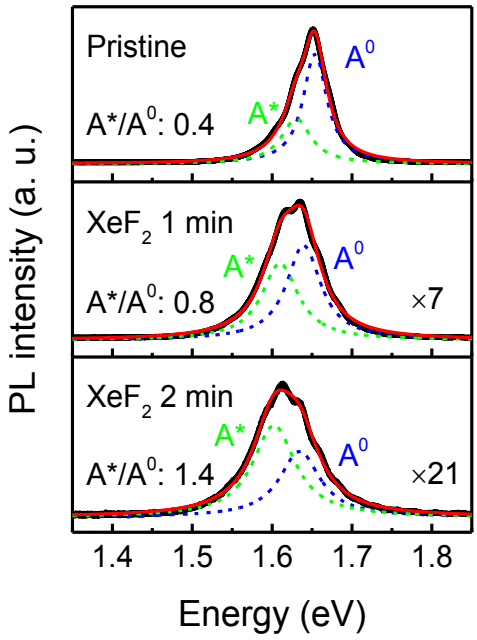

Figure 4-8. Photoluminescence (PL) spectra of pristine and XeF_2 thinned monolayer WSe_2 deconvoluted into neutral exciton (A^0, blue curves) and trion (A*, green curves) emission peaks with Lorentzian functions. The PL intensities are normalized to that of pristine WSe_2.

Photoluminescence (PL) spectroscopy has been performed on pristine and thinned monolayer WSe_2 to characterize the band-to-band emission arising from excitonic transitions. Figure 4-8 compares the normalized PL spectra of pristine monolayer WSe_2 and thinned monolayer WSe_2 achieved by XeF_2 exposure for 1 and 2 min. As shown in the first row spectrum, the pristine monolayer WSe_2 presents a prominent PL peak at 1.65 eV (the A excitonic emission), corresponding to the direct band gap transition (K to K point of the Brillouin zone), as reported in Ref. [10, 104]. The A emission can be deconvoluted further into neutral exciton emission at 1.65 eV (A^0) and trion emission at 1.63 eV (A*) [196]. It can be seen that the neutral excitons (A^0) dominate the PL emission of pristine WSe_2. In contrast to pristine WSe_2, the thinned monolayer WSe_2 after 1 min (second row spectrum) and 2 min (third row spectrum) XeF_2 treatment exhibit approximately 7- and 21-fold decrease in the A peak intensities and broadening of the A emission peaks from 48 meV (0 min) to 70 meV (1 min) and 80 meV (2 min) in FWHM, respectively. In addition, redshifts of the A emission peaks by 21 meV (1 min XeF_2 exposure) and 33 meV (2 min XeF_2 exposure) are observed in the thinned WSe_2. Moreover, the intensity ratios of trion (A*) to neutral exciton (A^0) emissions are found to increase with extending XeF_2 thinning time, from 0.4 (0 min) to 0.8 (1 min) and 1.4 (2 min), which indicates the existence of enhanced concentrations of excess carriers, thus doping effects, caused by XeF_2 treatment, as suggested from Raman measurements. As trions (A*) possess the features of lower PL efficiencies and lower PL emission energy compared to neutral excitons [196, 197], the presence of the higher ratio of trions in XeF_2 thinned WSe_2 can give rise to the observed weakening, broadening, and redshifts of the A emission peaks [198-200]. Note that the defects produced during vapour XeF_2 exposure could also contribute to the reduction of the PL peak intensities of the thinned WSe_2 [99, 101, 201].

4.4 XPS analysis of XeF_2 treated WSe_2

4.4.1 Few-layer WSe_2

To investigate the evolution of the surface composition of WSe_2 before and after vapour XeF_2 treatment, X-ray photoelectron spectroscopy (XPS) measurements have been carried out. Note that most of the XPS experiments have been conducted on

multilayer WSe_2 flakes unless otherwise specified. The survey spectrum (Figure 4-9a) of pristine WSe_2 consists of C, Si, O, W, and Se related peaks. An additional peak associated with F appears after vapour XeF_2 exposure.

Figure 4-9b, c show the high-resolution XPS spectra of W 4f and Se 3d core levels of WSe_2 before and after XeF_2 treatment under 1 Torr for 2 and 5 min, respectively. Before XeF_2 exposure, the doublet observed at 32.6 and 34.8 eV (first row spectrum in Figure 4-9b corresponds to $4f_{7/2}$ and $4f_{5/2}$ lines of W^{4+} contributed from pristine WSe_2 and the peak at 37.9 eV can be assigned to the W $5p_{3/2}$ core level of WSe_2, in agreement with the reports of [142, 202, 203]. The Se 3d core level spectrum of pristine WSe_2 (in the chemical state of Se^{2-}) exhibits a $3d_{5/2}$ and $3d_{3/2}$ doublet at 54.9 and 55.7 eV, as shown in the first row spectrum in Figure 4-9c. After WSe_2 has been treated with vapour XeF_2 for 2 min (second row spectrum in Figure 4-9b), a weaker doublet peak appears at 35.5 and 37.7 eV that can be associated with the $4f_{7/2}$ and $4f_{5/2}$ components of the W^{6+} and W^{5+} chemical states [204-206]. Moreover, the stronger doublet originating from the W 4f core level in the chemical state of W^{4+} shifts towards lower binding energy with 32.1 ($4f_{7/2}$) and 34.2 eV ($4f_{5/2}$). When the exposure time reaches 5 min as shown in the third row spectrum in Figure 4-9b, the W 4f core level of W^{4+} downshifts further by ≈0.8 eV compared with the spectrum of pristine WSe_2. Meanwhile, similar shifts in binding energy are also found in Se 3d core level spectra of WSe_2 treated by vapour XeF_2 for the same time. This observation indicates a Fermi level shift towards the valence band of the WSe_2 film, therefore confirming the presence of a p-doping effect (increased ratio of free hole carriers to electron carriers) caused by XeF_2 exposure, which is consistent with previous Raman and PL measurements. However, no additional doublet representing any other chemical state of Se is observed in the Se 3d core level spectra after XeF_2 exposure.

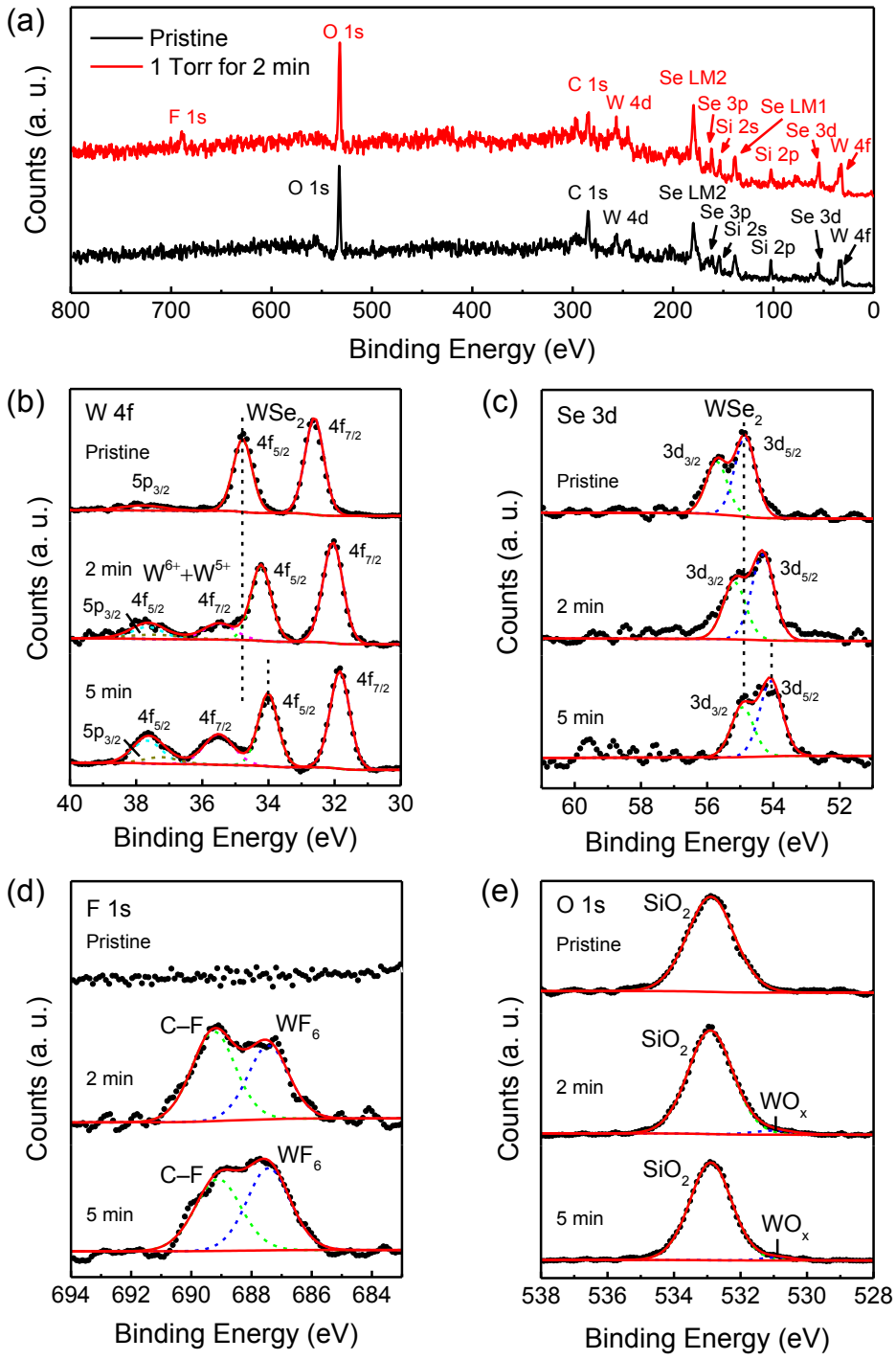

Figure 4-9. (a) XPS survey spectra of a pristine (black curve) and XeF_2 treated (red curve) sample within the range of 0–800 eV. High-resolution XPS spectra of W 4f (b), Se 3d (c), F 1s (d), and O 1s (e) core levels of the samples before and after XeF_2 treatment under 1 Torr for 2 and 5 min. The experimental data are displayed as black circles. The dashed lines are Gaussian-Lorentzian fits. The solid lines are the envelopes of the fitted components. The spectra are offset vertically for clarity. The vertical dashed lines serve as a guide to the eye.

To determine the origin of W^{6+} and W^{5+} chemical states, the high-resolution XPS spectra of F 1s and O 1s core levels of the samples have been acquired. After vapour XeF_2 treatment, a feature at 687.3 eV associated with W–F bond appears in Figure 4-9d, which can be attributed to WF_6 physically trapped in the lattice of thinned WSe_2. Similar results have also been reported in tungsten etching with fluorine-based etchants [207-209]. Although another etching product in the form of WF_4 has been observed in some of the previous reports on tungsten etching, represented by an XPS peak of F 1s core level at 684.0~685.0 eV [209-212], no sign of WF_4 is seen from the XeF_2 thinned WSe_2.

The molar amount of WSe_2 etched by vapour XeF_2 within 1 min can be estimated with the equation of $n_{WSe2} = \frac{Ah\rho}{M} f_{WSe2}$, where A is the area of the substrate (1 cm^2), ρ is the density of WSe_2 (9.32 g cm^{-3}), M is the molar mass of WSe_2 (341.76 g mol^{-1}), h is the etched depth of WSe_2 within 1 min (≤50 nm), f_{WSe2} is the proportion of the area covered by WSe_2 films to the whole substrate (≤0.04). Thus, the n_{WSe2} is extracted to be ≤ ($1.36 \times 10^{-7} \times f_{WSe2}$) mol ≤ 5.44×10^{-9} mol. The equation of $n_{XeF2} = \frac{PV}{RT}$ has been used to estimate the molar amount of vapour XeF_2 fed through the etching system per minute, where P is the pressure of etching environment (1 Torr), V is the volume of XeF_2 gas fed into the system in 1 min (25 cm^3), R is the ideal gas constant (8.314 m^3 Pa K^{-1} mol^{-1}), and T is the temperature of vapour XeF_2 exposure (≈298 K). The calculation gives $n_{XeF2} = 1.35 \times 10^{-6}$ mol. Under the condition of the tungsten and selenium being fluorinated fully, the chemical reaction will occur as below:

$WSe_2 + 9XeF_2 = WF_6 + 2SeF_6 + 9Xe$ and/or $WSe_2 + 18XeF_2 = WF_6 + 2SeF_6 + 18XeF$

Therefore, 1 unit of WSe_2 will react with 9–18 units of vapour XeF_2. The molar ratio of the available XeF_2 reactant to actually consumed WSe_2 is $n_{XeF2}/n_{WSe2} \geq 2.5 \times 10^2 >> 18$, which indicates that the WSe_2 etching has operated under F efficient regime. Therefore, the etching products are expected to be fully fluorinated species, i.e., WF_6 and SeF_6. Because of the greater volatility of SeF_6 (−46.6 °C in boiling point) than WF_6 (18 °C in boiling point), there is less chance for SeF_6 to be trapped inside of the WSe_2 lattice, which explains the observed absence of additional chemical states of Se.

In addition, some W–O bonds are suspected to form on top of the thinned WSe_2 after the samples have been exposed to air, due to the presence of a weak O 1s feature observed at around 531 eV buried by the strong O 1s peak at 533 eV contributed from SiO_2 substrate because of the smaller lateral dimension of WSe_2 than the X-ray spot, (20 μm in radius) in the O 1s core level spectra of XeF_2 treated WSe_2 (Figure 4-9e), which can be assigned to WO_x ($x \leq 3$) [99, 206, 208]. Also, the fact that the monolayer and bilayer WSe_2 achieved by vapour XeF_2 thinning are detected to be thicker than pristine WSe_2 as presented in Figure 4-6e, f, together with previously reported observation of the presence of WO_x from fluorine etched tungsten with no/low ion bombardment [213, 214], supports the existence of WO_x overlayer on XeF_2 thinned WSe_2. Overall, both the WO_x overlayer and trapped WF_6 could contribute to the chemical states of W^{6+} and W^{5+} found in vapour XeF_2 treated WSe_2. Moreover, the observed broadening of the W 4f and Se 3d peaks of WSe_2 after XeF_2 treatment in Figure 4-9b, c is likely to be attributed to the ionized impurity scattering from F^- within the trapped WF_6 and the rougher surface of WSe_2 after XeF_2 exposure.

4.4.2 Bulk WSe_2

Further XPS measurements have been performed on bulk WSe_2 with larger lateral dimension (in millimetre scale) than the X-ray spot to eliminate the interference of the signals contributed from the SiO_2/Si substrates. As shown in Figure 4-10a-d, the F 1s, O 1s, W 4f, and Se 3d core level spectra of pristine WSe_2, as well as XeF_2 treated WSe_2 before and after KOH solution immersion have been investigated. Before XeF_2 treatment, no peak in F 1s spectrum (Figure 4-10a), one O 1s peak located at 532.8 eV attributed to adsorbed water on WSe_2 (Figure 4-10b) [215], one doublet peak at 32.6 and 34.8 eV (Figure 4-10c), and another doublet at 54.8 and 55.7 eV (Figure 4-10c) contributed from W^{4+} and Se^{2-} have been observed, respectively. After vapour XeF_2 treatment of bulk WSe_2 for 5 min, an F 1s peak and an additional O 1s peak appear at 687.4 eV (Figure 4-10a) and 531.3 eV (Figure 4-10b), respectively, accompanied by the emergence of a weaker doublet peak corresponding to W^{6+} and W^{5+} chemical states in W 4f spectrum (Figure 4-10c), which indicates the existence of WF_6 and WO_x after XeF_2 treatment and air exposure. Meanwhile, the W^{4+} and Se^{2-} core levels present a

similar downshift in binding energy (Figure 4-10c, d), similar to the observation in Figure 4-9b, c, implying the p-doping of WSe_2.

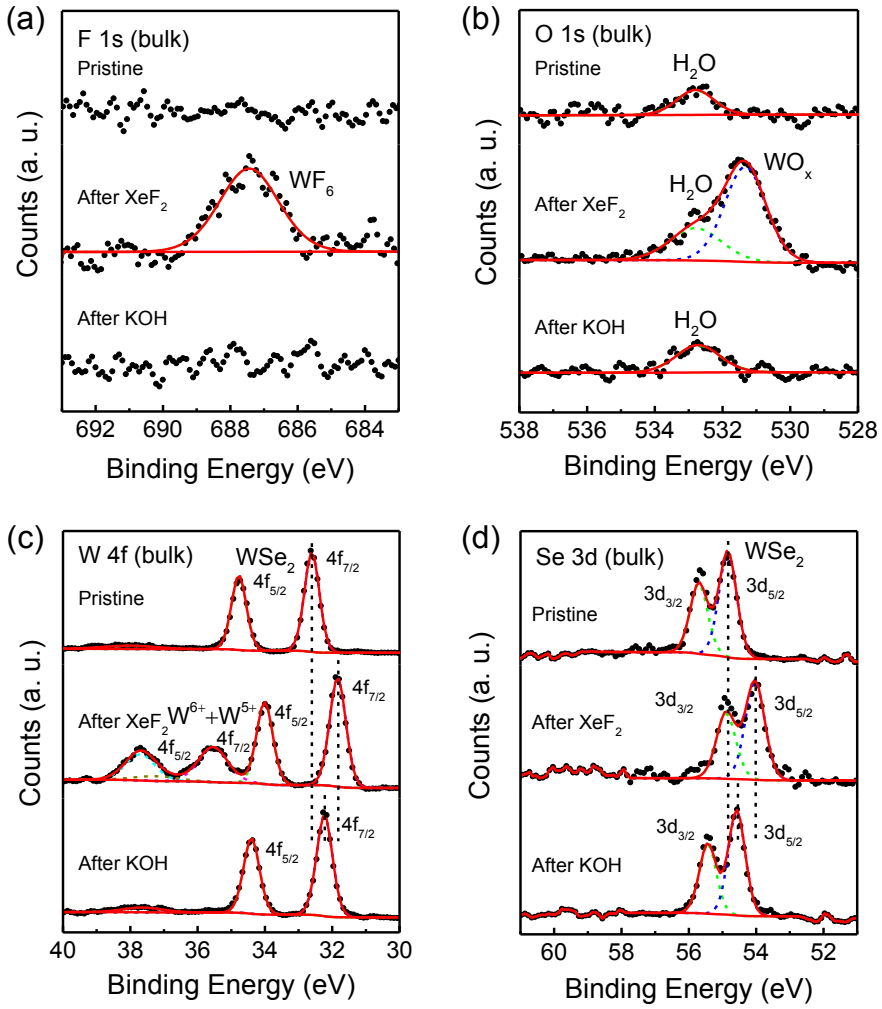

Figure 4-10. High-resolution F 1s (a), O 1s (b), W 4f (c), and Se 3d (d) core levels spectra of bulk WSe_2 before and after XeF_2 treatment for 5 min, followed by immersion in KOH solution for 15 s. The experimental data are displayed as black circles. The dashed lines are Gaussian-Lorentzian fits. The solid lines are the envelopes of the fitted components. The spectra are offset vertically for clarity. The vertical dashed lines serve as a guide to the eye.

The mechanism of WO_x production can be investigated using classical equilibrium thermodynamics. If the Gibbs free energy ΔG of a reaction is negative, then the reaction can occur spontaneously and vice versa. The lower the value of ΔG, the more spontaneous the reaction will be. Below are evaluations of some possible chemical

reactions when the XeF_2 treated WSe_2 undergoes exposure to air. The Gibbs free energy G of the reactants and products in their standard states (298K and 1 atmospheric pressure) obtained from Ref. [216, 217] have been used for calculation (The G of WO_x and WOF_x is assumed to equal that of WO_3 and WOF_4, respectively).

$2WF_6 + O_2 = 2WOF_4 + 2F_2$

$\Delta G = 2 \times (-1298) - 2 \times (-1631.4) = 666.8$ kJ mol^{-1} (Nonspontaneous)

$2WF_6 + 3O_2 = 2WO_3 + 6F_2$

$\Delta G = 2 \times (-764.1) - 2 \times (-1631.4) = 1734.6$ kJ mol^{-1} (Nonspontaneous)

$WF_6 + H_2O = WOF_4 + 2HF$

$\Delta G = (-1298) + 2 \times (-275.4) - (-1631.4) - (-228.6) = 11.2$ kJ mol^{-1} (Nonspontaneous)

$WF_6 + 3H_2O = WO_3 + 6HF$

$\Delta G = (-764.1) + 6 \times (-275.4) - (-1631.4) - 3 \times (-228.6) = -99.3$ kJ mol^{-1} (Spontaneous)

Therefore, based on the above thermodynamics, the reaction product of XeF_2 thinned WSe_2 when exposed to air should be WO_x produced from the reaction of trapped WF_6 and water in the air, while the possibility of the existence of WOF_x can also be excluded. However, no Raman peak belonging to WO_3 (around 712 and 802 cm^{-1}) [103, 218] has been observed from XeF_2 treated WSe_2 (see Figure A-1 in Appendix A), which indicates that the oxide film formed on top of the XeF_2 thinned WSe_2 could be substoichiometric (amorphous) WO_x with $x<3$ [99, 219].

Subsequently, the XeF_2 treated bulk WSe_2 has been immersed in 1 mol/L KOH solution for around 15 s, which is able to remove any existing WF_6 and WO_x. Then, the previously observed F 1s peak, the additional O 1s peak, and the weaker doublet peak of W^{6+} and W^{5+} disappear simultaneously, as shown in the third row spectra in Figure 4-10a-c, suggesting the removal of WF_6 and WO_x by the KOH solution immersion. At the same time, an upshift of W^{4+} and Se^{2-} core level in binding energy has been observed, which indicates a degradation of the p-doping effect on WSe_2 after WF_6 and WO_x are removed. This observation implies that WF_6 and WO_x contribute to the p-doping effect. However, the W^{4+} and Se^{2-} core level of WSe_2 after KOH solution

treatment does not shift back to the original binding energy of WSe_2 (first row spectrum in Figure 4-10c, d), the reason of which will be explained later.

4.4.3 Quantitative analysis

In order to quantify the surface composition of WSe_2, the area of peaks attributed to different components (W^{4+} and Se^{2-} from WSe_2, W^{6+} and W^{5+} from WF_6 and WO_x) have been computed after subtraction of background by the Shirley method and normalization with empirical relative sensitivity factors (2.75 for W and 0.67 for Se) [220]. The ratio of (W^{6+} + W^{5+}) to W^{4+} is seen to increase as the exposure time is extended (blue curve in Figure 4-11a). Notably, despite the different etching times, the XeF_2 thinned monolayer and bilayer WSe_2 are thicker than pristine WSe_2 with the same number of layers by the same amount (0.5~0.6 nm), as shown in Figure 4-6e, f. This observation indicates a fixed thickness of WO_x overlayer regardless of etching time, due to the previously reported self-limiting growth mechanism of WO_x [99, 195]. Therefore, the observed atomic ratio change in (W^{6+} + W^{5+})/W^{4+} is likely to be the result of an increased amount of trapped WF_6 produced during the vapour XeF_2 exposure, which could be within several nanometers from the surface of XeF_2 thinned WSe_2 [213].

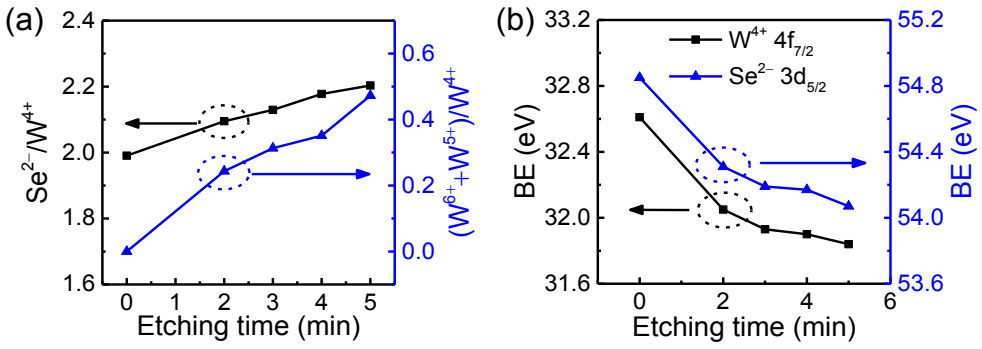

Figure 4-11. (a) Se^{2-}/W^{4+} (black curve) and (W^{6+} + W^{5+})/W^{4+} (blue curve) atomic ratios versus etching time extracted by integration of the XPS peaks. (b) The evolution of binding energy (BE) of W $4f_{7/2}$ and Se $3d_{5/2}$ lines of WSe_2 as a function of XeF_2 exposure time.

Additionally, the atomic ratio of Se^{2-} to W^{4+} goes beyond the standard stoichiometric ratio of WSe_2 (2:1) as the etching time increases (black curve in Figure 4-11a),

suggesting that the availability of W^{4+} bonded with Se^{2-} to form stoichiometric WSe_2 becomes less and less during the vapour XeF_2 treatment, thus rendering the presence of non-stoichiometric WSe_2, i.e., WSe_x with $x>2$. In the case of the uniform layer thinning with surface roughness below 0.7 nm here, the WSe_x is estimated to be 1~2 layer thick, mainly formed at the reaction interface of WSe_2 with vapour XeF_2. The fact that removing WF_6 and WO_x by KOH solution immersion does not shift the W^{4+} core level back to the binding energy of pristine WSe_2, as mentioned before, is possibly due to the remaining non-stoichiometric WSe_x contributing to the p-doping effect.

4.5 Summary of the doping mechanism by vapour XeF_2

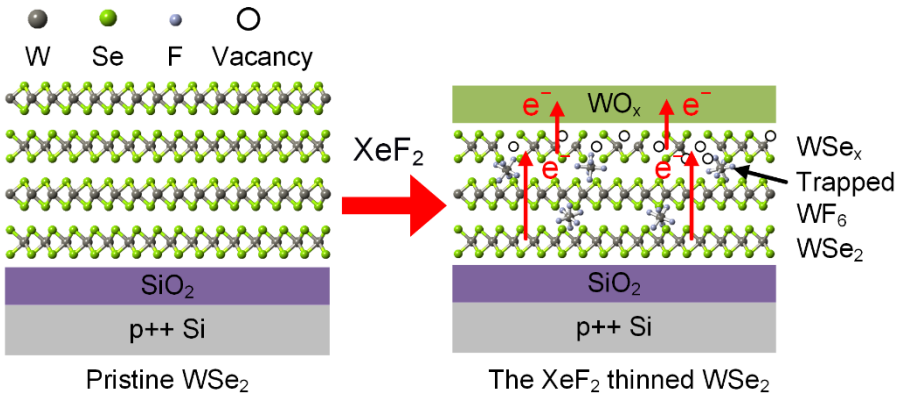

Figure 4-12. Proposed schematic (not to scale) of XeF_2 treated WSe_2 after exposed to air.

To summarize the observed p-doping effect on WSe_2 induced by vapour XeF_2 treatment, three factors could play important roles as depicted in the schematic of Figure 4-12: 1) the large work function of WO_x (≈6.7 eV) [221] enables electron transfer from the underlying thinned WSe_2 to the WO_x overlayer, resulting in the electron carriers depletion in thinned WSe_2 (serving as hole-injection layer) [195]; 2) the presence of fluorine atoms from the WF_6 trapped in the lattice of thinned WSe_2, owing to a stronger electronegativity (3.9) than that of W (1.7) and Se (2.55) [216], attracts the excess electrons from WSe_2 making the thinned WSe_2 p-doped [222]; 3) the non-stoichiometric WSe_x with W^{4+} cation deficiency formed on the surface of the XeF_2 treated WSe_2 could act as electron acceptors and lead to an increase in the hole

density [101, 152, 223, 224]. It is noteworthy that the effective p-doping region, where electrons are depleted, and holes are the major conductive carriers, can exist beyond the location of electron acceptors (non-stoichiometric WSe_x layers and F^- resided layers in this case) based on the Ref. [189]. Additionally, as shown in Figure 4-11b, the degree of binding energy downshift of W $4f_{7/2}$ and Se $3d_{5/2}$ core levels of WSe_2 increases as XeF_2 exposure time extends. This observation indicates the reduced energy difference between the Fermi level and the valence band of WSe_2 and hence increased p-doping level with longer XeF_2 treatment.

4.6 Electrical characterization of XeF_2 treated WSe_2 FETs

4.6.1 Continuous treatment of a WSe_2 FET by vapour XeF_2

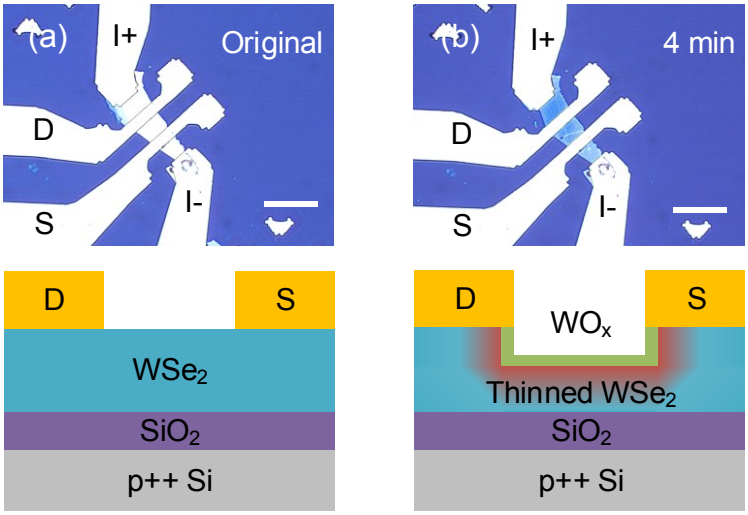

Figure 4-13. Optical (top row) and schematic (bottom row, not to scale) images of a WSe_2 FET before (a) and after (b) 4 min XeF_2 treatment under 1 Torr. Scale bars are 20 µm.

To gain more insight into the doping effects introduced by vapour XeF_2 treatment, WSe_2 FETs have been fabricated and characterized electrically. For these devices, highly p-doped Si substrates serve as back gate electrodes with 300 nm SiO_2 as gate dielectrics, and e-beam evaporated Ti (30 nm)/Al (200 nm) metal stacks have been used as metal electrodes. Figure 4-13a, b display the optical images and schematic

illustrations of a WSe_2 FET before and after vapour XeF_2 treatment. In order to eliminate the impact of contact resistance $R_{contact}$ on the device performance, four-terminal measurements have been employed, unless otherwise specified.

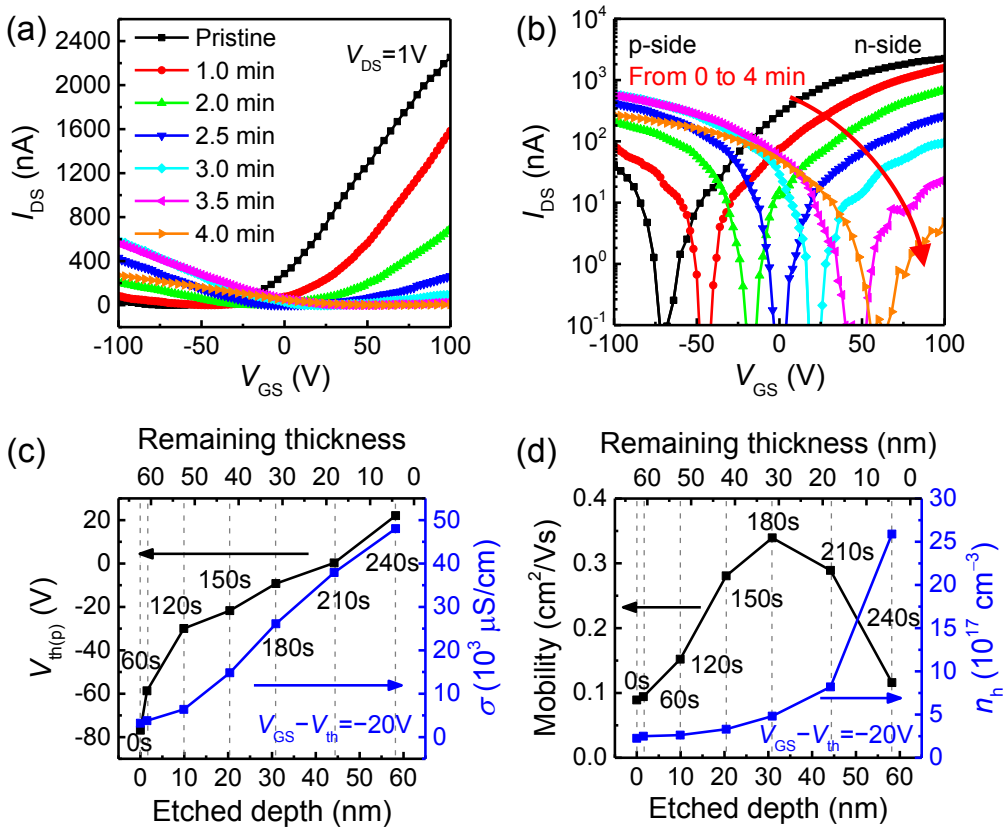

Figure 4-14. The transfer characteristics (I_{DS}–V_{GS}) of the WSe_2 FET at V_{DS} = 1V before and after XeF_2 treatment under 1 Torr for different etching times, plotted in linear (a) and logarithmic (b) scales. (c) The threshold voltage on the p-side $V_{th(p)}$ and hole conductivity σ at $V_{GS} - V_{th(p)} = -20$ V versus etched depth h. (d) Hole mobility μ_h and volume concentration n_h when $V_{GS} - V_{th(p)} = -20$ V as a function of etched depth h. The top axes of (c, d) indicate the remaining thickness of the WSe_2 channel after XeF_2 etching.

Figure 4-14a, b show the linear and logarithmic plots of transfer curves (I_{DS}–V_{GS}) of the WSe_2 FET obtained at a fixed drain bias (V_{DS} = 1 V) before and after vapour XeF_2 exposure under 1 Torr for various times. The transfer characteristic of the pristine WSe_2 FET exhibits an n-type dominant ambipolar behaviour with the threshold voltage at the hole (p-side) and electron (n-side) transport regime measured to be $V_{th(p)}$ = −76.8 V and $V_{th(n)}$ = −11.2 V, respectively. The threshold has been extracted by

extrapolating the slopes of the linear plots of I_{DS}–V_{GS} curves down to 0 A. While after the XeF_2 treatment for 4 min, the ambipolar behaviour of the WSe_2 FET becomes n-type dominant with $V_{th(p)}$ = 22.1 V and $V_{th(n)}$ = 72.3 V, respectively.

Left axis of Figure 4-14c presents the relationship of the threshold voltage at the hole transport regime $V_{th(p)}$ with respect to etching time t and etched depth h extracted from Figure 4-14a. A shift of the $V_{th(p)}$ towards higher voltage with increasing etching time and etched depth has been observed in Figure 4-14c, which can be attributed to the vapour XeF_2 induced p-doping effect (increased ratio of free hole carries to electron carriers) and reduced thickness of the WSe_2 channel [162]. Notably, when the WSe_2 channel is etched to ≈20 nm thick after 3.5 min XeF_2 treatment, the FET possesses a threshold voltage $V_{th(p)}$ of 0 V (Figure 4-14c), and holes start to become the dominant carriers at V_{GS} = 0 V (Figure 4-14b) in the meantime. After 4 min vapour XeF_2 treatment, the volume conductivity (derived by $\sigma = \sigma_s/d$) at a constant gate voltage bias ($V_{GS} - V_{th(p)} = -20$ V) is found to increase by more than one order of magnitude (from 3.2×10^3 to 4.8×10^4 μS cm^{-1}), as presented by the right axis of Figure 4-14c.

The field-effect hole mobility μ_h can be calculated from the linear region of the σ_s–V_{GS} curves on the p-side with the expression of $\mu_h = (d\sigma_s/dV_{GS}) \times (1/C_{ox})$, where $C_{ox} = 11.5 \times 10^{-9}$ F cm^{-2} is the capacitance between the WSe_2 channel and back gate per unit area ($\varepsilon_0\varepsilon_{ox}/d_{ox}$; ε_{ox} = 3.9; d_{ox} = 300 nm). Furthermore, the hole volume concentration n_h can be derived from the relation $\sigma = n_h q \mu_h$, where q is the elementary charge. As shown in Figure 4-14d, the hole mobility μ_h (left axis) first shows a positive then negative dependence on the increasing etching time and etched depth, while the hole volume concentration n_h (right axis) only exhibits a rising trend as etching time extends. When WSe_2 is relatively thick, the current I_{DS} injected from metal contacts on the top surface of WSe_2 needs to flow down to lower layers (bypass some interlayer resistance) before flowing across the WSe_2 channel, because the gate electric field only modulates the free carrier in the bottom layers as a result of charge screening [141]. Therefore, the improvement of hole mobility with increasing etching time in the first stage is caused mainly by the decreasing series interlayer resistance resulting from the reduction of WSe_2 thickness. As the thickness of the WSe_2 channel is thinned to ≈30 nm, the hole mobility enters a downtrend, while further reduction in the thickness of the thinned WSe_2 results in a significant enhancement in hole concentration. This observation

suggests that for a thinned WSe_2 with thickness ≤30 nm, the impact of the XeF_2 induced p-doping is much larger, and the hole carriers in the XeF_2 treated WSe_2 film are likely to undergo more ionized impurity (F^-) and charge-charge scatterings. In addition, the thinner WSe_2 films are more susceptible to carrier scattering induced by increased surface roughness and interfacial Coulomb impurities (including chemical residues on top of WSe_2 film and surface dangling bonds on the SiO_2/Si substrate) [160], which can also be responsible for the observed degraded hole mobility.

4.6.2 Comparison of pristine and XeF_2 treated WSe_2 FETs

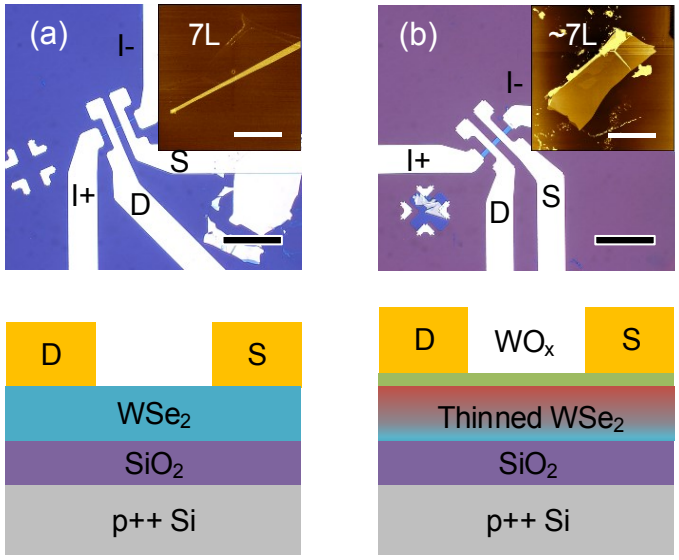

Figure 4-15. Optical, AFM (tow row) and schematic (bottom row, not to scale) images of the FETs fabricated from pristine (a) and XeF_2 thinned (b) WSe_2 with a similar number of layers (≈7-layer). Insets are AFM images of the WSe_2 flakes used for the device fabrication. Scale bars are 40 and 10 μm for optical and AFM images, respectively.

As the thickness variation of WSe_2 can affect the electrical performance of the FET including electrical mobility, threshold voltage, and contact resistance [141, 160, 162, 165, 166, 225-227], in order to study the p-doping effect of vapour XeF_2 treatment without the contribution of reduced thickness of WSe_2, two FETs made from pristine WSe_2 (Figure 4-15a) and XeF_2 thinned WSe_2 (Figure 4-15b) with a similar number of layers (≈7-layer) have been characterized, and their electrical transfer properties have been compared, as shown in Figure 4-16a. The pristine WSe_2 FET exhibits an n-type

dominant ambipolar behaviour with a $V_{th(p)}$ of −45V, while the XeF_2 thinned WSe_2 FET shows an increased value of $V_{th(p)}$ with 18V, which confirms the p-doping effect introduced by vapour XeF_2 treatment. Further calculation (See Appendix B, for details) supports the conclusion of degenerate p-type doping with the vapour XeF_2. However, distinct from some degenerate doping methods that lead to a near-metallic transport behaviour of doped WSe_2 [155, 179, 184], the XeF_2 treated WSe_2 still possesses an apparent semiconducting behaviour, which is critical for the fabrication of logic circuits and optoelectronic devices.

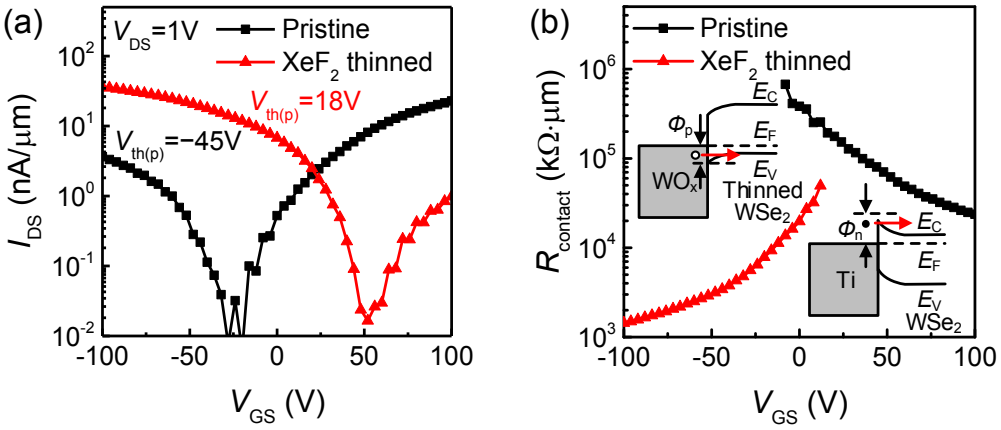

Figure 4-16. (a) Transfer characteristics (I_{DS}–V_{GS}) of the two different FETs at a fixed V_{DS} = 1 V plotted in logarithmic scale. (b) Contact resistance $R_{contact}$ versus gate voltage V_{GS} for the two different FETs. Insets are schematics of the band alignment for the WO_x/thinned WSe_2 and Ti/pristine WSe_2 interfaces.

Figure 4-16b depicts the contact resistance $R_{contact}$ between Ti and WSe_2 of the two kinds of FETs with respect to gate voltage V_{GS}, which has been extracted from two-terminal and four-terminal measurements. As the gate voltage increases, the contact resistance of pristine WSe_2 FET shows a descending tendency while the contact resistance of the FET made from XeF_2 thinned WSe_2 ramps up with values of more than one order of magnitude smaller. For the pristine WSe_2 FET, as discussed before, an n-type Schottky barrier is formed at the Ti/WSe_2 interface. As the gate voltage increases, the width of the Schottky barrier decreases due to the upshift of Fermi level of WSe_2, leading to the reduction of contact resistance. In the case of XeF_2 thinned WSe_2 FET, where an additional layer of WO_x exists on the thinned WSe_2, the contact

between Ti and thinned WSe_2 includes Ti/WO_x and WO_x/thinned WSe_2 dual interfaces. Although WO_3 is an n-type semiconductor with a comparatively large band gap of 2.6~2.9 eV [228, 229], the oxygen vacancies in the WO_3 lattice can narrow the band gap greatly [206]. Therefore, the substoichiometric WO_x can be considered as a metal with a low density of states at the Fermi level and should form an Ohmic contact with Ti at the Ti/WO_x junction [230]. Owing to a high work function of WO_x (≈6.7 eV) [221], the Fermi level of WO_x should lie below the VBM of thinned WSe_2, and one would expect an Ohmic hole contact at the WO_x/thinned WSe_2 junction when the interface Fermi-level pinning of WO_x contacts can be neglected [230]. However, in reality, the WO_x work function can be lowered by oxygen vacancies in the substoichiometric WO_x and carbon contamination (e.g., resist residues) introduced from the device fabrication process, which has been observed in previous reports [195, 231, 232]. Therefore, the notable Schottky contact behaviour of Ti/WO_x/thinned WSe_2 interfaces seen in Figure 4-16b can be attributed to the degraded work function of WO_x which makes the Fermi level of WO_x lie between the CBM and VBM of WSe_2. Nevertheless, the WO_x contact still forms a lower Schottky barrier with WSe_2 than Ti contact does, which allows more effective tunnelling of charge carriers through the contact barriers.

4.7 Air stability of vapour XeF_2 doping

Further tests (electrical and XPS characterization) on the air stability of the XeF_2 doping of WSe_2 have been conducted. Figure 4-17a shows the I_{DS}–V_{GS} curves (plotted in logarithmic scale) at V_{DS} = 1V obtained from the same XeF_2 thinned WSe_2 FET in Figure 4-15b after exposure to air (class 10 cleanroom environment with ≈20 °C in temperature and 35~45 % in humidity) for different time durations. As can be seen, after exposure to air for 240 h, the device still exhibits a p-doping feature, although the threshold voltage on the p-side $V_{th(p)}$ shifts towards the negative direction gradually with increasing time of air exposure, as shown in Figure 4-17b. The similar decreasing trend has also been observed in the I_{DS} when V_{GS} = −80 V and n_h when V_{GS} = 0 V, as shown in Figure 4-17c, indicating a reduction of the p-doping degree caused by ambient air. Note that the I_{DS} exhibits a relatively large degradation (reduced by 40%) after the first 70 h of air exposure, then the device undergoes a gradual I_{DS} drop by

11% after an additional 70 h exposure to air, and eventually starts to stabilize at a certain current level, exhibiting a 5% drop through the last 100 h. Similar to the behaviour of I_{DS}, the hole concentration n_h decreases quickly during the first 140 h and then starts to flatten. The instability of the p-doping effect is most likely to be due to the lowering of WO_x work function arising from atmospheric adsorbates (e.g., carbon contamination and water) located on the top surface of WO_x, as previously observed [195, 233-236]. Therefore, the reduced efficiency of charge transfer from the underlying thinned WSe_2 to the WO_x overlayer can contribute to the decreased hole carrier density and hence degrade the p-doping effect. In addition, the W 4f core level of W^{4+} is observed to upshift slightly by ≈0.1 eV in binding energy after XeF_2 treated WSe_2 has been exposed to air for 6 days as shown in Figure 4-17d, due to the lowering of the p-doping level. Nevertheless, the atomic ratio of $(W^{6+} + W^{5+})/W^{4+}$ is found to stay almost unchanged (≈0.3) after air exposure, which means that the overlayer WO_x could serve as a barrier preventing WF_6 detrapping from the WSe_2 lattice.

Overall, distinct from other unstable surface adsorption or molecular doping methods (e.g., NO_2, K vapour, polyethyleneimine, and $Co_6Se_8(PEt_3)_6$ doping) of which the doping effect will become ineffective once exposed to ambient air for a short period (as depicted in Figure 4-2) [155, 185, 186, 237], the XeF_2 doped device exhibits no significant degradation of p-doping features during the testing period of 10 days, which is crucial for the fabrication of the devices that need to operate at ambient condition for a long-term. In the future, further improvement of the air stability of XeF_2 doping can be achieved by deposition of an additional passivation layer on top of the devices [238]. The doping of WSe_2 with vapour XeF_2 approach can be used to fabricate complementary inverters and lateral p-n junction on the same WSe_2 film for applications in logic circuits, p-n diodes, photovoltaics, and light-emitting diodes (LEDs).

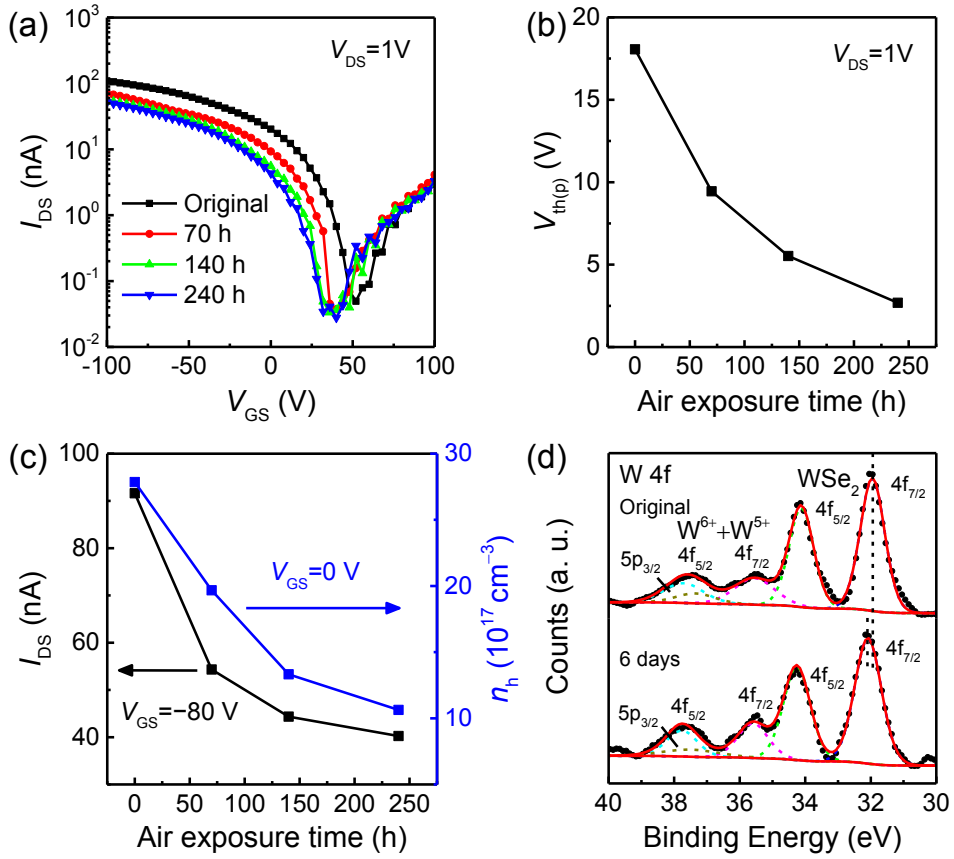

Figure 4-17. (a) Transfer characteristics (I_{DS}–V_{GS} when V_{DS} = 1V) of a XeF_2 doped WSe_2 FET before and after exposure to ambient air for different time durations. The $V_{th(p)}$ (b), I_{DS} at V_{GS} = −80V (left axis of c), and n_h at V_{GS} = 0V (right axis of c) as a function of air exposure time. (d) High-resolution XPS spectra of W 4f core level of XeF_2 treated WSe_2 before and after air exposure for 6 days.

4.8 Conclusions

In summary, an approach for controllable layer thinning and air-stable p-type doping of WSe_2 has been developed by vapour XeF_2 treatment. The surface roughness of XeF_2 thinned WSe_2 can be controlled to below 0.7 nm at an etched depth of 100 nm, which is smoother than general plasma thinning methods. The etching rate of WSe_2 shows a significant dependence on the exposure pressure of vapour XeF_2. Therefore, by tuning the exposure pressure, slow etching and fast etching can be achieved easily for different applications, i.e., thinning and patterning. The phenomena of blueshifts of the E^1_{2g} mode, redshifts of the PL peaks, downshifts of W 4f and Se 3d core levels in

binding energy, and upshifts of the threshold voltage towards higher voltage, observed from Raman, PL, XPS, and electrical characterization of XeF_2 treated WSe_2, respectively, indicate a p-doping effect introduced by vapour XeF_2 exposure. The p-doping effect could be the result of 1) the formation of a substoichiometric WO_x ($x<3$) overlayer on thinned WSe_2 when exposed to air, 2) trapped reaction product of WF_6 within the thinned WSe_2 lattice, and 3) the non-stoichiometric WSe_x ($x>2$) formed at the reaction layer of WSe_2 with vapour XeF_2. By simply adjusting the XeF_2 exposure time, the p-doping level can be controlled easily. The XPS measurements show a Fermi level shift of 0.5~0.8 eV as a function of the vapour XeF_2 exposure time, and the hole doping concentration extracted from electrical measurements can be up to 25.9×10^{17} cm^{-3} which lies in the degenerate doping regime. The junction of Ti/WO_x/thinned WSe_2 exhibits a p-type Schottky contact behaviour with a contact resistance of more than one order of magnitude lower than that of the Ti/pristine WSe_2 junction. The thinning and p-doping of WSe_2 with vapour XeF_2 have the combinatorial advantages of easy scale-up, excellent controllability, high etching selectivity, and compatibility with CMOS fabrication technologies, which is promising for future practical applications including tuning the performance of 2D WSe_2 via thickness engineering and fabricating complex logic circuits, solar cells, and LEDs with 2D WSe_2.

Chapter 5 In-plane elastic properties of 2D WSe_2

5.1 Introduction

Although the elastic properties of some TMDs (such as MoS_2 [6, 7, 37] and WS_2 [37]) have been investigated as mentioned in Section 1.2.1, the experimental measurement of elastic properties of 2D WSe_2 has not been reported yet. To explore the suitability of 2D WSe_2 in the applications of flexible electronics or optoelectronics and nanoelectromechanical systems (NEMS), the characterization of the elastic properties of 2D WSe_2 is essential.

Unlike the conventional tensile or compressive testing method, the in-plane mechanical properties testing of 2D materials is usually performed in a suspended structure on a substrate due to the small dimension and hence tricky manipulation of 2D materials. There are mainly two ways of fabricating a suspended structure with 2D materials. One approach is to transfer 2D materials directly onto pre-patterned substrates, as illustrated in Figure 5-1a [3, 7, 239-244]. The other approach is to transfer 2D materials onto a non-patterned substrate first and then remove the supportive layer beneath (Figure 5-1b) [70, 76, 135, 136, 245-248] as employed in Section 3.2.2. Afterwards, bending experiments on suspended 2D materials under application of a controlled concentrated force by a sharp tip or distributed force (e.g., electrostatic force or pressure difference) can be performed to study the in-plane mechanical properties. In the bending experiments, atomic force microscope (AFM) is used widely to characterize the deformation of the suspended 2D sheets under a certain amount of external force. Once the relationship of external force versus deformation of suspended 2D materials is obtained experimentally, specific mechanical models represented by mathematical expressions are selected and applied to fit the experimental data to extract the corresponding mechanical parameters of 2D materials.

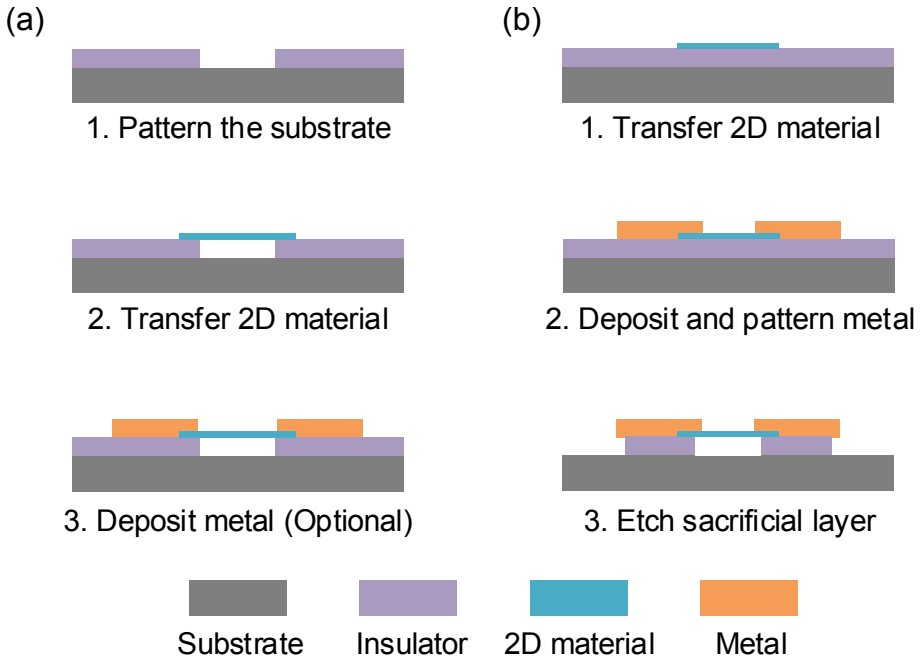

Figure 5-1. Schematics of two representative approaches of suspended 2D materials fabrication: (a) transfer 2D materials directly onto a pre-patterned substrates; (b) suspend 2D materials by removing the supportive layer underneath.

In this chapter, the in-plane elastic properties (including the Young's modulus, prestress, and breaking strain) of exfoliated 2D WSe_2 have been investigated with nanoindentation experiments. The detailed characterization method is given in Section 5.2 and 5.3. The measured statistical results and comparison of elastic properties of 2D WSe_2 to other 2D materials are presented in Section 5.4. The work aims to pave the way for the design and fabrication of 2D WSe_2-based flexible devices and NEMS.

5.2 Preparation of suspended WSe_2 membranes

The indentation experiments have been performed on 2D WSe_2 membranes suspended over circular holes with an atomic force microscope (AFM). Firstly, 300 nm SiO_2 has been grown on Si substrates by thermal oxidation. Then, the SiO_2 layers have been patterned with circular hole (1.55 μm and 2.6 μm in diameter, 220 nm in depth) arrays by photolithography and CHF_3/Ar plasma-based RIE as described in Figure 5-2. Figure 5-3 shows the AFM images of a SiO_2/Si substrate patterned with hole arrays. After etching, the photoresist has been stripped by sonication in acetone, isopropyl

alcohol (IPA), and deionized (DI) water sequentially. Then the substrates have been soaked in piranha solution (H_2SO_4:H_2O_2 = 3:1) for 30 min and rinsed in DI water to remove organic residues, followed by O_2 plasma treatment to increase the interaction between 2D WSe_2 flakes and SiO_2 surface by removing ambient adsorbates on the SiO_2 surface [159, 249].

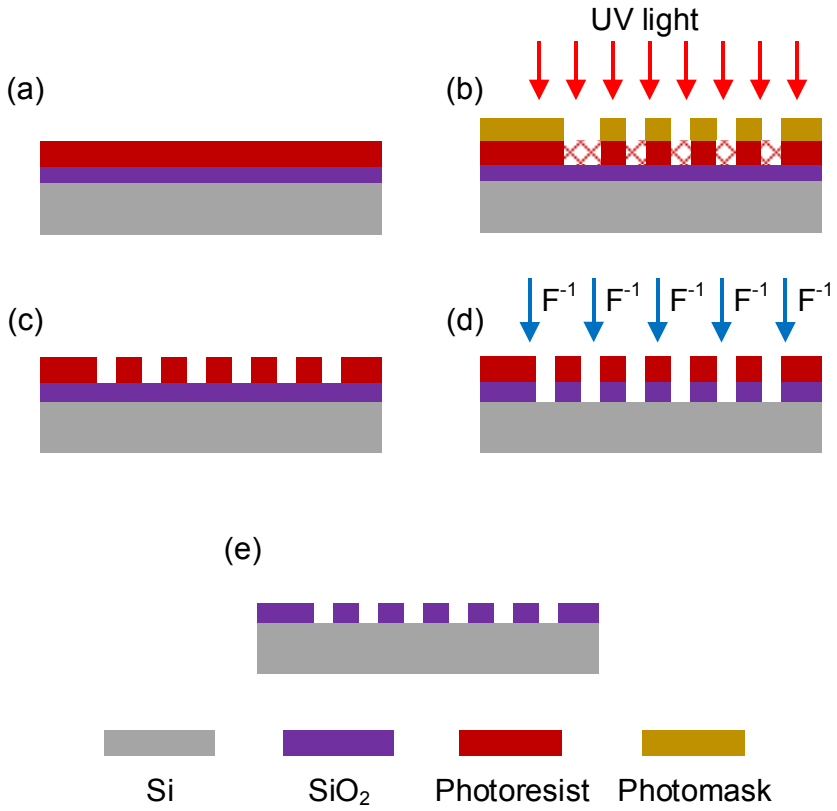

Figure 5-2. Schematic of patterning a SiO_2/Si substrate with hole arrays. (a) Spin coating of photoresist on top of the substrate. (b) Expose the photoresist under UV light with photomask covering on top. (c) Develop the photoresist. (d) Pattern SiO_2 with fluorine-based reactive ion etching (RIE). (e) Strip the photoresist.

Thereafter, 2D WSe_2 flakes have been exfoliated mechanically from bulk WSe_2 crystals and transferred onto the pre-patterned SiO_2/Si substrates with a PDMS stamp. Then AFM has been used to obtain the topography and thickness h of WSe_2 flakes on the substrates. The number of layers of the corresponding flakes has been derived by dividing the measured thickness h by interlayer distance. An interlayer distance of 0.70 nm for WSe_2 [103, 140] has been adopted for calculation.

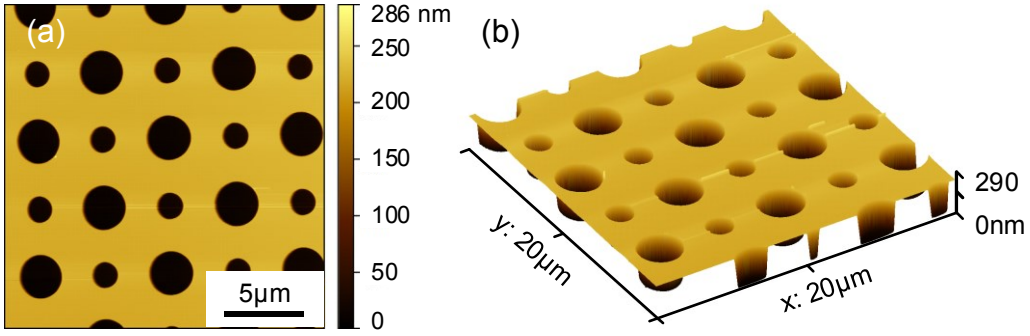

Figure 5-3. Top view (a) and 3D view (b) AFM images of a SiO_2/Si substrate patterned with hole arrays.

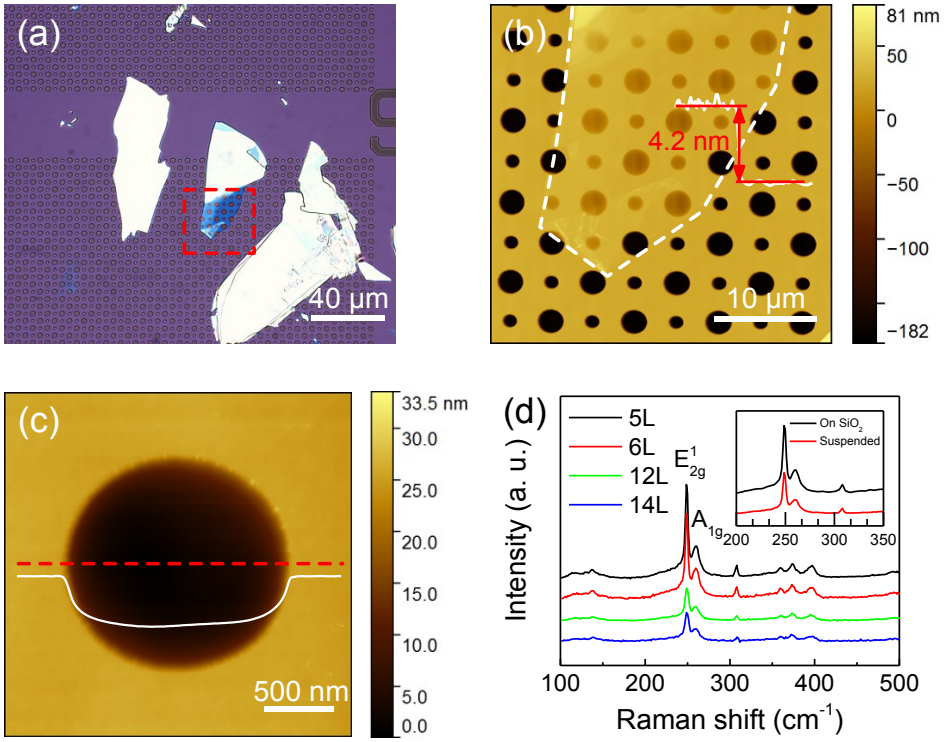

Figure 5-4. (a) Optical image of WSe_2 flakes transferred onto a pre-patterned SiO_2/Si substrate. (b) AFM image of the corresponding WSe_2 flake inside the square area of (a). (c) AFM image of a WSe_2 membrane suspended over a hole and a superimposed height profile (along the dashed line) showing a step height of ≈30 nm. (d) Raman spectra of the suspended WSe_2 flakes with different numbers of layers in the range of 100–500 cm^{-1}. The inset shows the Raman spectra of substrate-supported and suspended areas of a 5-layer (5L) WSe_2 flake in the range of 200–350 cm^{-1}. Spectra are offset vertically for clarity.

Figure 5-4a shows the optical image of 2D WSe_2 flakes that have been transferred onto a substrate pre-patterned with an array of holes, forming several suspended WSe_2 membranes over the holes. Figure 5-4b presents the AFM image of the corresponding WSe_2 flake in the square area of Figure 5-4a, while Figure 5-4c shows the magnified AFM topography image of the suspended area of a 6-layer (6L) WSe_2 membrane over a 1.55 μm diameter ($2r$) hole. No visible bubbles, wrinkles or residue particles have been found on the membranes, which benefits from the appropriate pressure control during the all-dry transfer process of 2D WSe_2 onto the substrate [241]. The height profile superimposed in the AFM image of Figure 5-4c shows a uniform height around the edge of the hole, indicating that the WSe_2 membrane adheres tightly to the edge of the hole by van der Waals interaction (dispersion forces or dipole interactions or both) with the substrate. The Raman spectra of the 2D WSe_2 flakes suspended over the holes are shown in Figure 5-4d. The in-plane mode E^1_{2g} (248.7 cm^{-1}), out-of-plane mode A_{1g} (259.6 cm^{-1}) [192], and a weak peak at 308.2 cm^{-1} arising from the interlayer interaction [103] have been observed. No Raman splitting of the E^1_{2g} mode has been observed, indicating no large strain (>1%) exists in the transferred WSe_2 flakes [51]. The inset of Figure 5-4d compares the Raman spectra of substrate-supported and suspended areas of a 5-layer (5L) WSe_2 flake. No peak position shift of E^1_{2g} and A_{1g} modes has been found, which suggests a similar level of strain exists in the supported and suspended areas.

5.3 Indentation experiments

To obtain the in-plane elastic properties of the suspended membranes, indentation experiments using AFM have been conducted. Prior to the indentation, the samples have been scanned for 1 hour under AFM to minimize the thermal drift of the piezoelectric scanner. Then, the tip of an AFM probe has been positioned to the centre of the suspended area of a membrane, and the membrane has been indented with a loading/unloading rate of 100 nm/s repeatedly for several cycles. The data during the loading process has been captured.

During the indentation experiments, the AFM probe was fixed, while the sample on the piezoelectric scanner approached towards the AFM probe, as illustrated in Figure 5-5. The indentation depth (membrane deformation) at the centre of a membrane has

been determined by $\delta = \Delta Z - d$, where ΔZ is the displacement of the piezoelectric scanner and d is the deflection of the AFM probe as the AFM probe starts to contact with the WSe_2 membrane. The force applied from the AFM tip onto the membranes can be derived from $F = k \times d$, where k is the spring constant of the AFM probe (35.7 N/m), which has been calibrated with the method mentioned in Section 2.4.

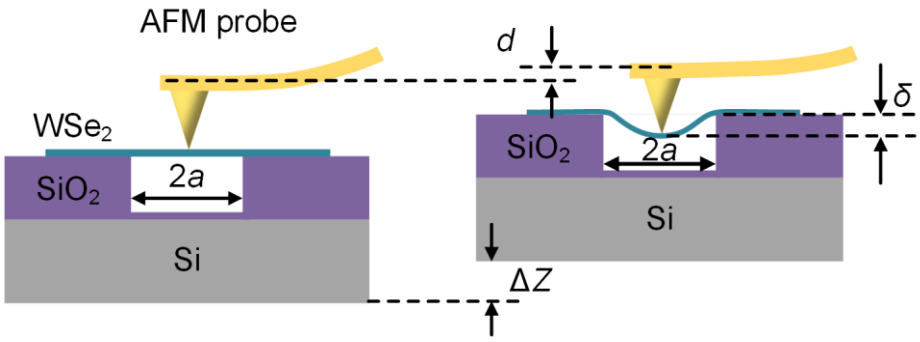

Figure 5-5. Schematic of the indentation experiment on a suspended WSe_2 membrane.

In order to obtain the correct force–deformation (F–δ) curves of the WSe_2 membranes, it is critical to identify the point where the AFM probe starts to indent the sample, so that the ΔZ and δ can be determined precisely. Figure 5-6a shows a representative AFM probe deflection d versus scanner displacement Z curve obtained directly from the indentation experiment. When the gap between the AFM probe tip and sample is close enough, the AFM probe bends downwards suddenly because of the attractive force near the surface of the sample (as shown in the inset of Figure 5-6a). As the sample continues to approach the probe, the AFM probe bends backwards, then straightens, and deflects upwards sequentially. To obtain the point where the AFM probe is restored to the zero force point, the differential of the d–Z curve in the inset of Figure 5-6a has been calculated, as presented in Figure 5-6b. The centre of the relatively flat region (between the two vertical dashed lines) of the differential curve is approximately the zero force point (marked as "O") [3]. Afterwards, the points around "O" have been assumed to be the zero force point to extract several sets of force–deformation (F–δ) curves that have been fitted with Equation (4-1) using the least square method afterwards. The zero force point has been determined when the minimum curve fitting error has been achieved. In addition, during the measurement, when the maximum indentation depth is applied to a same membrane, no visible

difference among the *d*–*Z* curves obtained from different times of indentation has been observed, as shown in Figure 5-7, indicating that no plastic deformation has occurred to the membranes, and the membranes have not slid over the margins of holes either.

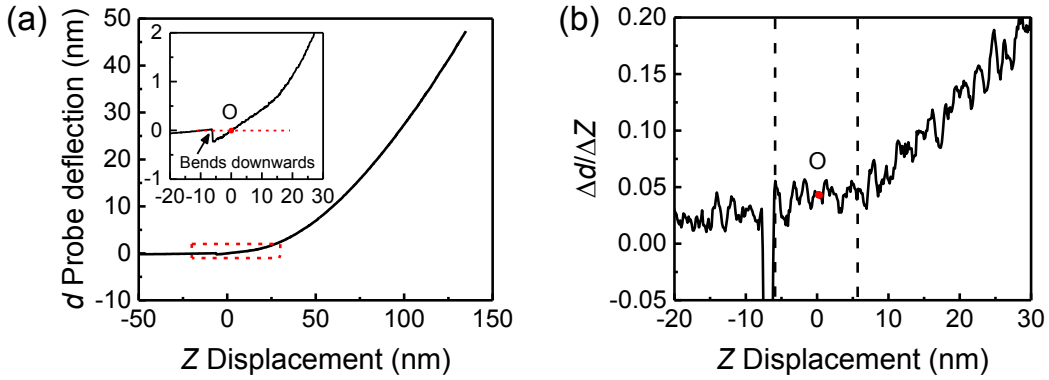

Figure 5-6. (a) A representative AFM probe deflection *d* versus scanner displacement *Z* curve obtained on a suspended WSe_2 membrane. The inset shows a magnified graph of the red rectangular area. (b) The differential curve extracted from the *d*–*Z* curve in the inset of (a).

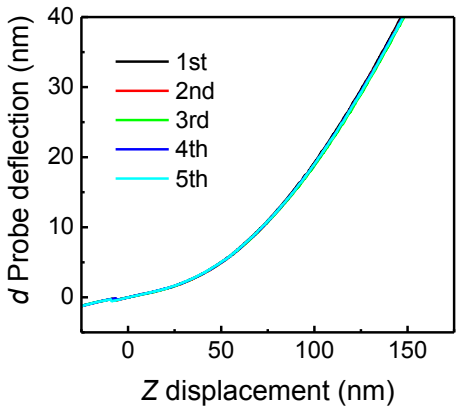

Figure 5-7. AFM probe deflection *d* versus scanner displacement *Z* curves obtained from a 6-layer WSe_2 membrane with 5 times indentation.

Representative force *F* versus displacement Δ*Z* curves on a suspended WSe_2 membrane and a SiO_2/Si substrate are shown in Figure 5-8a. When the AFM probe indents towards the rigid substrate, the probe deflection *d* is assumed to be equal to the displacement of the scanner Δ*Z*, which has been used to calibrate the sensitivity of the photodetector of the AFM. Since WSe_2 owns a three-fold rotation symmetry and the

suspended area of WSe_2 has circular symmetry, each WSe_2 membrane has been modelled as a film with isotropic in-plane mechanical properties. Figure 5-8b shows the representative force–deformation (F–δ) curves obtained from 2D WSe_2 membranes with different numbers of layers, which can be approximated with the Schwering-type solution as [3, 250, 251]:

$$F = \left(\sigma_0^{2D}\pi\right)\delta + \left(E^{2D}\frac{q^3}{r^2}\right)\delta^3, \tag{4-1}$$

where σ_0^{2D} is the pretension, r is the radius of the hole, E^{2D} is the 2D elastic modulus, v is the Poisson's ratio (0.19 [252, 253] for WSe_2), and q is a dimensionless constant determined by $q = 1/(1.05 - 0.15v - 0.16v^2)$. With the least square fitting of the experimental data using the Equation (4-1), the pretension σ_0^{2D} and 2D elastic modulus E^{2D} of the membranes can be derived. The fitted curves (solid lines in Figure 5-8b) show good agreement with the experimental data, demonstrating the suitability of the chosen mechanic model. From this model, we can see the applied load F has an approximately linear relationship with the indentation depth δ when the membrane deformation is small, while follows a cubic relationship under large deformation.

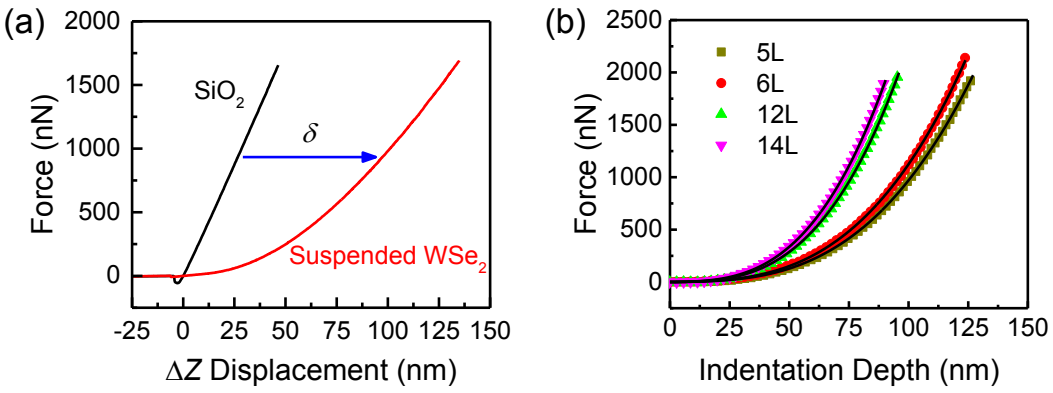

Figure 5-8. (a) Force–displacement (F–ΔZ) curves obtained on a suspended WSe_2 membrane and a SiO_2/Si substrate. (b) Representative force–deformation (F–δ) curves for suspended 2D WSe_2 membranes with different numbers of layers. The symbols correspond to the experimental data, and the solid lines are fitted curves that agree well with the experimental results.

5.4 Results and discussions

5.4.1 2D elastic modulus and pretension

To determine the variation of the mechanical properties of the suspended WSe_2 membranes, statistical analysis has been conducted on several WSe_2 flakes with 5-, 6-, 12-, and 14-layer. For each set of layers, the test has been done on 5 membranes with 3 different indentation depths twice, and therefore 30 force–deformation curves have been obtained, which derives 30 sets of σ_0^{2D} and E^{2D} from the curve fittings. The results in Figure 5-9 show that both the extracted 2D elastic modulus E^{2D} and pretension σ_0^{2D} are independent of the indentation depth δ, which verifies the WSe_2 membranes undergo linear elastic deformations and no sliding of WSe_2 membranes over the substrates during the indentation experiments during the measurements.

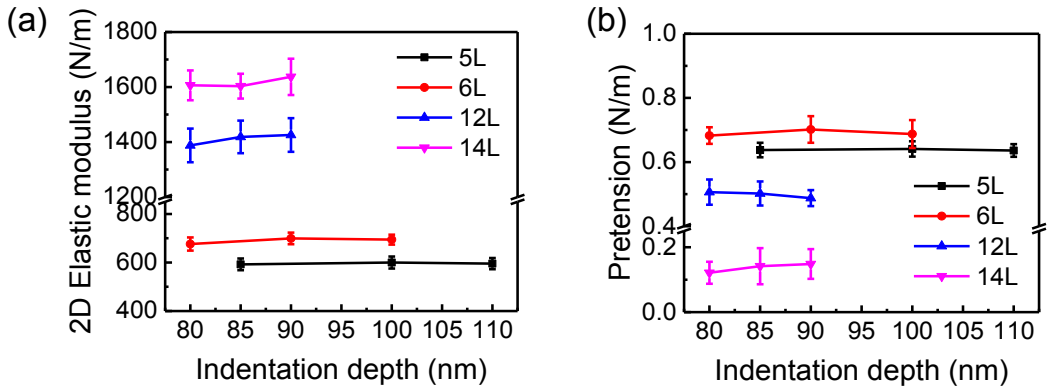

Figure 5-9. 2D elastic modulus E^{2D} (a) and pretension σ_0^{2D} (b) obtained from suspended WSe_2 membranes with different numbers of layers at various indentation depths. The error bars represent the standard deviations.

The histograms of the derived 2D elastic modulus E^{2D} and pretension σ_0^{2D} for WSe_2 membranes with different numbers of layers are shown in Figure 5-10 and Figure 5-11, respectively, which can be fitted with Gaussian distributions. The mean 2D elastic modulus E^{2D} and their standard deviations are 596 ± 23, 690 ± 25, 1411 ± 61, and 1615 ± 56 N/m for 5-, 6-, 12-, and 14-layer WSe_2 membranes, respectively. The deviations are attributed to different defect densities, stacking faults in the membranes, offsets of

the AFM tip from the centre of membranes, and curve fitting errors. The relative standard deviation (ratio of the standard deviation to the mean) of E^{2D} is about 3~4 %, while the relative deviation resulting from the offset of the AFM tip is estimated to be ≈0.5 % conservatively and the relative curve fitting errors have been found to be <0.1 %, which indicates that it is the intrinsic crystal property variation across different test samples that contributes to the observed deviations most. The 2D elastic modulus E^{2D} of the 2D WSe_2 membranes has been observed to increase statistically linearly as the number of layers increases, as shown in Figure 5-12, indicating that interlayer sliding has not occurred during the indentation experiments due to the reported relatively strong WSe_2 interlayer interaction originating from the van der Waals force [254].

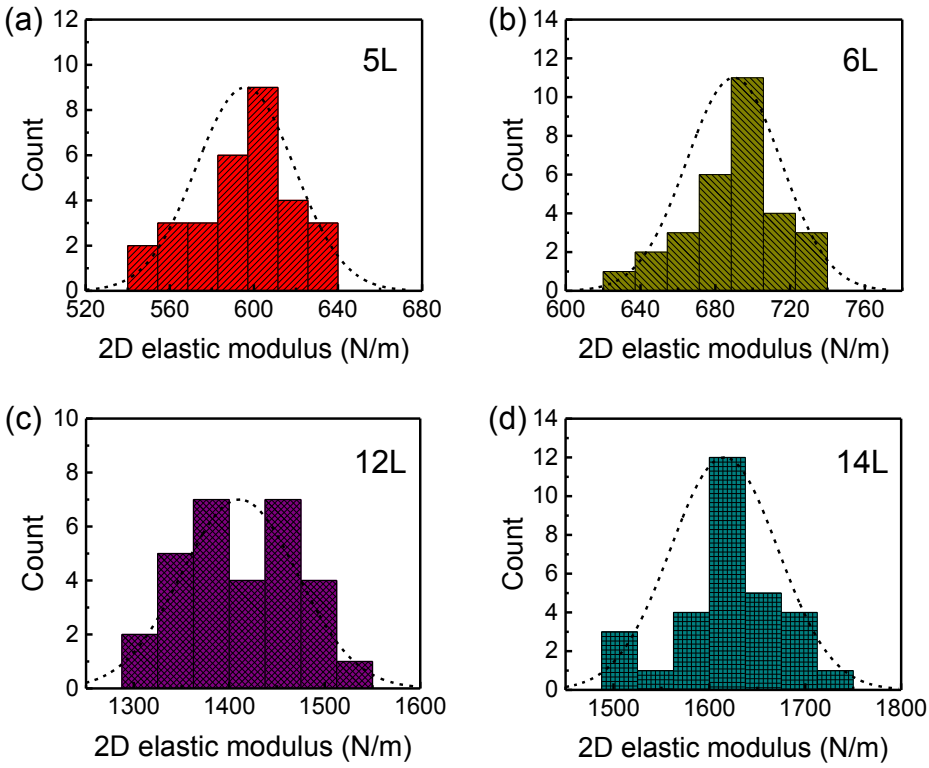

Figure 5-10. Histograms of 2D elastic modulus E^{2D} acquired from the curve fitting for 5L (a), 6L (b), 12L (c), and 14L (d) WSe_2 membranes. The dashed lines indicate the fitted Gaussian distributions.

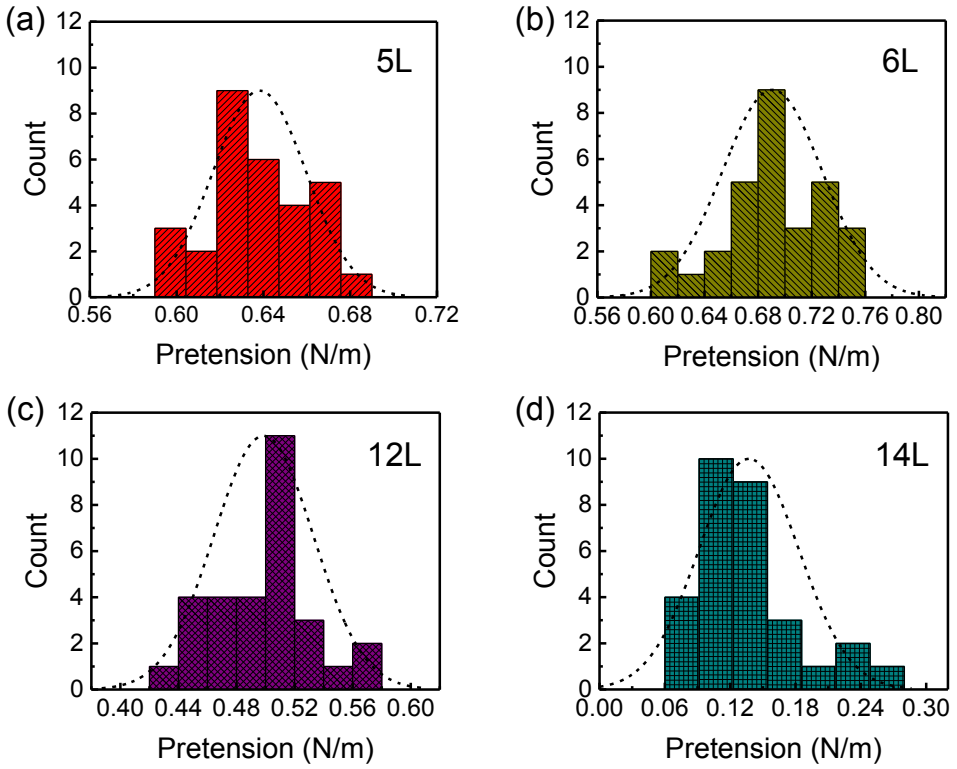

Figure 5-11. Histograms of pretension σ_0^{2D} acquired from the curve fitting for 5L (a), 6L (b), 12L (c), and 14L (d) WSe_2 membranes. The dashed lines indicate the fitted Gaussian distributions.

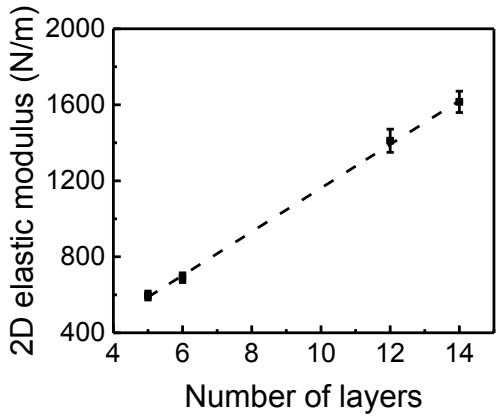

Figure 5-12. 2D elastic modulus E^{2D} of WSe_2 membranes as a function of the number of layers. The error bars represent the standard deviations.

5.4.2 Young's modulus and prestress

In order to compare the elastic properties of 2D WSe_2 with bulk materials and other 2D materials, the 2D elastic modulus E^{2D} has been converted to the normal 3D Young's modulus E_Y by dividing the 2D value by the thickness of the membranes h. Figure 5-13a shows the box chart of Young's modulus E_Y for WSe_2 membranes with 4 different numbers of layers. No statistical difference of E_Y among the different thick WSe_2 membranes has been observed in the results, which indicates the Young's modulus E_Y of the measured 2D WSe_2 membranes is independent of the thickness h. The corresponding values are 170.3 ± 6.7, 166.3 ± 6.1, 167.9 ± 7.2, and 164.8 ± 5.7 GPa for 5-, 6-, 12-, and 14-layer WSe_2 membranes, respectively, which is close to one of the first principle simulation results [253]. Moreover, the mean value of E_Y (167.3 ± 6.7 GPa) for 2D WSe_2 is smaller than that of multilayer MoS_2 (≈330 GPa) [6], monolayer MoS_2 (≈270 GPa) [7, 37], monolayer WS_2 (≈270 GPa) [37] and roughly equal to one-sixth of graphene (≈1.0 TPa) [3, 45]. The smaller Young's modulus of 2D WSe_2 compared to 2D MoS_2 and WS_2 is possibly due to the weakened binding between the metal and chalcogen induced by the increased lattice constant and decreased charge transfer of WSe_2 [253]. For a given geometry of NEMS, the fundamental resonant frequency will be lower if the Young's modulus of the suspended structure is lower or the density is higher [255, 256]. Thus, 2D WSe_2 with a relatively higher density (9.32 g/cm^3) [257] and lower Young's modulus compared to other 2D materials (e.g., graphene, MoS_2, and WS_2) can be put into the application of NEMS resonator working in the audio frequency, such as acoustic sensor [81] and loudspeaker [82]. In addition, when flexible electronics composed of 2D materials are bent or stretched, extra stress will be formed at the interface between the 2D material and soft polymeric substrate, due to the mismatch of their mechanical properties, which may weaken the reliability of the devices. 2D WSe_2 with lower Young's modulus can reduce this kind of stress and therefore may be more suitable for flexible device applications.

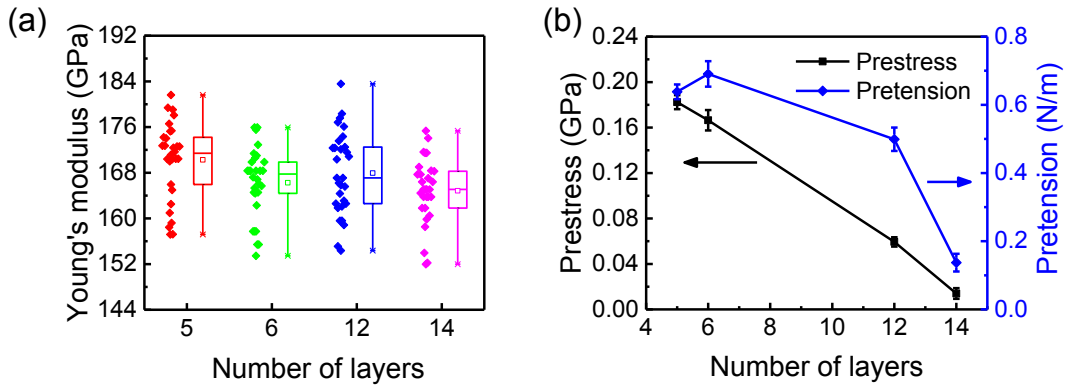

Figure 5-13. (a) The box chart of Young's modulus E_Y for WSe_2 membranes with different numbers of layers. Each plot includes the minimum, lower quartile, median (horizontal line), mean (hollow square), upper quartile, maximum and discrete data at the left. (b) Pretension σ_0^{2D} and prestress σ_0 for the corresponding 2D WSe_2 membranes.

Figure 5-13b shows the extracted pretension σ_0^{2D} and prestress σ_0 (pretension divided by the thickness of the membranes h) with respect to the number of WSe_2 layers. As can be seen, the pretension σ_0^{2D} varies with the thickness of WSe_2 h and is in the same scale as the reports of Ref. [6, 37] that employ a similar 2D materials transfer method. In addition, the prestress σ_0 decreases approximately linearly as the number of layers increases. The prestress σ_0 existing in WSe_2 membranes mainly originates from the mechanical exfoliation and transfer process of 2D WSe_2. During the transfer process, the pressing of PDMS stamp together with 2D WSe_2 would have resulted in the PDMS stamp expanding laterally due to great softness of the PDMS [258], which could have stretched the WSe_2 flakes to a certain extent. When the PDMS stamp has been peeled off from substrates, the stretched WSe_2 flakes have adhered to the SiO_2/Si substrates by van der Waals force, which results in the positive (tensile) pretension residing in the transferred flakes.

5.4.3 Breaking stress and strain

During the whole indentation experiments, the maximum force F_{max} applied to these WSe_2 membranes is ≈3200 nN. None of the membranes has been fractured, and all still have kept their original elastic properties after this force. The maximum stress σ_{max}

for a circular and linear elastic membrane during an indentation experiment with a spherical indenter in the case of $r_{tip}/r \ll 1$ can be derived with the expression as [259]

$$\sigma_{max} = \sqrt{\frac{F_{max} E^{2D}}{4\pi r_{tip} d^2}} . \quad (4\text{-}2)$$

Thus, the maximum stress σ_{max} for a 5-layer WSe_2 membrane is calculated to be ≈12.4 GPa. As the 2D WSe_2 has been observed to undergo linear elastic deformation during the indentation measurements, assumption of linear relationship of stress with strain ($\sigma = E_Y \cdot \varepsilon$) can be made, which results in the maximum strain ε_{max} of approximate 7.3%. Therefore, 2D WSe_2 can withstand at least ≈12.4 GPa stress and ≈7.3% strain without breaking or mechanical degradation (The breaking stress/strain is larger than ≈12.4 GPa/≈7.3%). This means the breaking strain of 2D WSe_2 is at least three times larger than that of silicon (0.4~2.2%) [260] and comparable to the common materials used for substrates of flexible devices, such as polyimide (PI) and PDMS (≈7%) [49], implying the suitability of 2D WSe_2 in flexible device applications.

5.5 Conclusions

In this chapter, 2D WSe_2 membranes suspended over circular holes have been fabricated. The elastic properties of the suspended WSe_2 membranes with different numbers of layers (5-, 6-, 12-, and 14-layer) have been first time determined experimentally using nanoindentation methods. The results show that although the prestress σ_0 decreases approximately linearly as the number of layers increases, the Young's modulus E_Y is independent of the number of layers, which indicates the interlayer interaction is strong enough to prevent the interlayer sliding during the conducted indentation measurements. The Young's modulus of 2D WSe_2 is about two-thirds of other most studied 2D semiconducting TMDs, namely MoS_2 and WS_2, and one-sixth of graphene. During the experiments, the measured 2D WSe_2 membranes have withstood ≈12.4 GPa stress and ≈7.3% strain without breaking or mechanical degradation. 2D WSe_2 can be an attractive alternative for graphene in some applications requiring flexible semiconducting materials, such as bendable transistors, photodetectors, and photovoltaics, as well as NEMS resonators operating in the audio frequency, such as acoustic sensors and loudspeakers.

Chapter 6 Strain and field-effect induced electronic properties change of WSe_2: theoretical studies

6.1 Introduction

Internal strain can be formed during the preparation process of 2D materials, such as mechanical exfoliation and stamp transfer of 2D materials to target substrates as discussed in Chapter 5. Chemical vapour deposition (CVD) synthesis process of 2D materials under high temperature (generally above 500 °C) can also results in internal strain existing in the synthesised 2D materials due to the thermal mismatch (different thermal expansion coefficients between 2D materials and the substrate) [261-263]. Moreover, strain can be applied externally to 2D materials by extending or bending the flexible substrates that 2D materials are located on or embedded in [50, 52, 264]. The electrons in a semiconductor experience the periodic potential of the crystal lattice, which leads to the formation of energy bands. Application of stress induces changes of the crystal lattice parameters and crystal symmetry properties hence modifying the electrons distribution. Therefore, strain can affect the band structure of a semiconductor. As introduced in Section 1.2.2, experimental photoluminescence (PL) studies have proved that the strains existing in 2D materials can modify the band gaps of TMDs [50-53]. The tunable band gap under strain results in the strain-dependent optical and electrical properties of TMDs [70, 265, 266], which can be used for novel strain sensor applications. Furthermore, strain can be used for engineering the band gap for enhancing the performance of TMDs-based optoelectronics, such as photodetectors, LEDs, and solar cells. Although the band gap changes can be probed via PL measurements, the influence of strain on the crystal structure and band structure of 2D TMDs can hardly be quantified with experimental methods. Furthermore, neither theoretical or experimental study of electrical transport property of 2D WSe_2 under different levels of strain has been reported.

In addition, doping TMDs with field-effect is one of the most widely used doping methods owing to the advantages of reversibility, great universality, and excellent

controllability. Although a great quantity of experimental studies has been conducted to characterize the performance of 2D WSe_2 under field-effect with various configurations (back-gate, top-gate, dual-gate, and electrolyte-gate) [154, 156, 185, 267, 268], more profound understanding of the influence of the field-effect on the fundamental properties, including the crystal structure, band structure, and conductive channel size of WSe_2 is still unknown due to the inaccessibility by experiments.

In this chapter, systematic first-principles calculations have been conducted within the framework of plane-wave based density functional theory (DFT) to study the evolutions of the crystal structure, band structure, and electrical transport property of 2D WSe_2 under the effects of tensile strain and field-effect in Section 6.2 and Section 6.3, respectively. Computational methods for applications of strain and field-effect under the established DFT models are introduced at the beginning of each section (Section 6.2.1 and Section 6.3.1). At last, the primary calculated results are summarized in Section 6.4. The computed results are expected to provide more insights into the strain and field-effect engineering of 2D WSe_2 for future practical applications such as strain sensors. Note that the calculations in this chapter are under the assumption of perfect crystals (no defects) and no contamination from the ambient environment.

6.2 Strain engineering

6.2.1 Computational methods

In the structural optimization, both the lattice vectors and atomic coordinates have been optimized using the BFGS algorithm with the convergence thresholds of 10^{-6} Ry on total energy and 10^{-3} Ry/Bohr on force. A full structure relaxation (lattice vectors and atomic coordinates) has been first performed to determine the unstrained atomistic structure. In the case of strained structures, the lattice parameters have been fixed with specific values, and the atomic coordinates have been allowed to relax. The biaxial in-plane strain is defined as $\varepsilon = (a - a_0)/a_0 \times 100\%$, where a_0 and a are the lattice constants of the unstrained and strained cells, respectively. Then self-consistent field (SCF) calculations have been performed to find the ground-state charge density for the

previously optimized structures with the convergence threshold for total electronic energy set to 10^{-10} Ry.

To obtain the electronic band structure and density of states (DOS), non-self-consistent calculations have been performed starting from the converged charge density of the optimized structures. Compared to the more extensively studied MoS_2, WSe_2 has been reported to possess a stronger spin-orbit coupling (SOC, electromagnetic interaction between the electron's magnetic dipole associated with the spin of electrons, its orbital motion, and the electrostatic field of the positively charged nucleus) with larger spin-orbit splitting (SOC induced shifts in an electron's atomic energy levels) due to the heavier W and Se atoms [269, 270]. Here, the calculations of band structures and DOS with and without inclusion of the SOC effect have been performed comparatively using scalar and fully relativistic pseudopotential, respectively.

6.2.2 Structural geometry

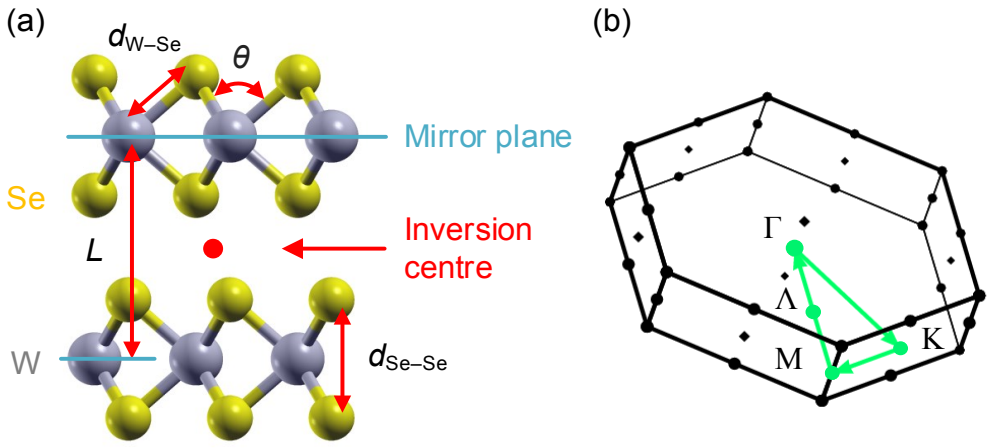

Figure 6-1. (a) Schematic of the 2H-WSe_2 crystal structure (grey-W atom; yellow-Se atom). (b) The k-path (green) of Γ–M–K–Γ in the Brillouin zone of WSe_2.

Figure 6-1a depicts the crystal structure of 2H-WSe_2 (hexagonal symmetry, two atomic layers per repeat unit, trigonal prismatic coordination). The WSe_2 with an odd number of layers contains a mirror plane (mirror symmetry), whereas the one with an even number of layers owns an inversion centre (inversion symmetry).

Table 6-1. The structural parameters (W–Se bond length $d_{W–Se}$, Se–Se intralayer distance $d_{Se–Se}$, Se–W–Se bond angle θ, and interlayer separation distance L) of WSe_2 under various levels of biaxial tensile strain.

Number of layers	**Strain (%)**	$d_{W–Se}$ **(Å)**	$d_{Se–Se}$ **(Å)**	θ **(°)**	L **(Å)**
1	0	2.542	3.370	80.825	N/A
	1	2.548	3.346	81.564	N/A
	2	2.554	3.322	82.288	N/A
	3	2.561	3.298	82.996	N/A
2	0	2.540	3.367	80.886	6.591
	1	2.548	3.344	81.625	6.560
	2	2.554	3.320	82.350	6.531
	3	2.561	3.297	83.005	6.504
3	0	2.542	3.369	80.825	6.588
	1	2.543	3.354	81.251	6.574
	2	2.546	3.341	81.620	6.559
	3	2.550	3.329	81.984	6.544
Bulk	0	2.540	3.365	80.889	6.566
	1	2.546	3.341	81.629	6.539
	2	2.553	3.317	82.355	6.511
	3	2.560	3.293	83.064	6.485

Table 6-1 lists the structural parameters of WSe_2 (W–Se bond length $d_{W–Se}$, Se–Se intralayer distance $d_{Se–Se}$, Se–W–Se bond angle θ, and interlayer separation defined by the proximal W–W interlayer distance L, as annotated in Figure 6-1) under various biaxial tensile strains. Note that the calculated $d_{W–Se}$ (2.54 Å) and $d_{Se–Se}$ (3.36 Å) of unstained bulk 2H-WSe_2 are in agreement with the reported experimental value (2.53 Å for $d_{W–Se}$ and 3.34 Å for $d_{Se–Se}$) [122]. As the applied biaxial tensile strain increases, the W–Se bond length $d_{W–Se}$ increases whereas the Se–Se intralayer distance $d_{Se–Se}$ and the interlayer separation L of multilayer WSe_2 decrease. The ionic position change

under strain results in modification of the electronic structures of WSe_2, which will be discussed in the next section.

6.2.3 Band structure and DOS

6.2.3.1 Electronic band structure

Figure 6-2 compares the calculated electronic band structures along the Γ–M–K–Γ k-point path (Figure 6-1b) for unstrained 1~3-layer and bulk WSe_2 without (left column) and with (right column) inclusion of the SOC. When the SOC effect is not considered, both the conduction band minimum (CBM) and valence band maximum (VBM) are located at the K point of the Brillouin zone forming a 1.64 eV direct band gap, which is in agreement with the experimental PL results (≈1.65 eV) reported in Ref. [10, 123] and Chapter 3. Unlike monolayer WSe_2, the unstrained multilayer WSe_2 exhibit indirect band gap semiconducting features due to the interlayer hybridization. The interlayer hopping of electrons between different atomic layers [271] leads to splittings of the uppermost valence band (UVB) at the Γ point as well as the lowermost conduction band (LCB) at the Λ point that consequently become the VBM and CBM of multilayer WSe_2, respectively. However, the LCB of multilayer WSe_2 is nearly degenerate around the K point. In addition, the LCB at the Λ point moves down while the UVB at the Γ point shifts up as the number of WSe_2 layers increases, while the energy of the LCB at the K point stays almost unaffected.

After inclusion of the SOC effect (presented in the right column of Figure 6-2), the band structures of unstrained WSe_2 are modified in three significant aspects below: (1) the CBM of monolayer WSe_2 shifts to the Λ point exhibiting an indirect band gap semiconductor, and the VBM of bilayer and trilayer WSe_2 move from the Γ point to K point in the presence of the SOC, as reported previously in Ref. [51, 272]; (2) compared to the calculations without the SOC effect, the band gaps of WSe_2 are reduced because of the reported underestimation of band gap calculated with the GGA method [51] due to the approximations employed in the DFT as introduced in Section 2.5. Meanwhile the thinner WSe_2 tends to undergo greater influence (1.64 to 1.29 eV for monolayer, 1.39 to 1.17 eV for bilayer, 1.21 to 1.08eV for trilayer, and 1.00 to 0.92 eV for bulk); (3), the SOC induced spin-orbit splitting (break in spin degeneracy) of the UVB and LCB along the path of M–K–Γ (not including the M and Γ points) has

been observed from monolayer and trilayer WSe_2, due to the absence of inversion symmetry in the WSe_2 with odd number of layers [269, 273]. The maximal splitting is located at the K point of the UVB (459 meV) observed from monolayer WSe_2, which is larger than the reported values of monolayer MoS_2 (149 meV), $MoSe_2$ (183 meV), and WS_2 (426 meV) [269], indicating that monolayer WSe_2 is a more promising material among the 2D TMD family for the realization of spin field-effect transistor.

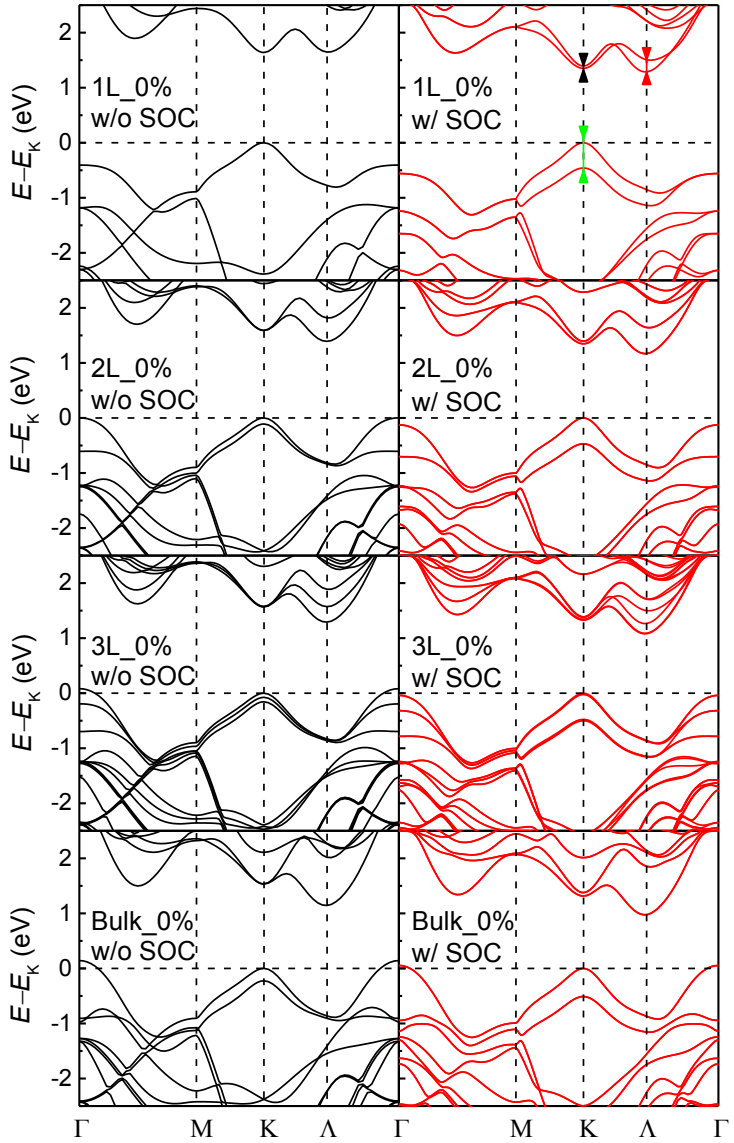

Figure 6-2. Calculated electronic band structures of unstrained 1~3-layer and bulk WSe_2 without (left column, black) and with (right column, red) inclusion of the SOC. Energies are given relative to the local maximum of the uppermost valence band (UVB) around the K point. The paired arrows at the top right plot point out the SOC induced spin-orbit splitting.

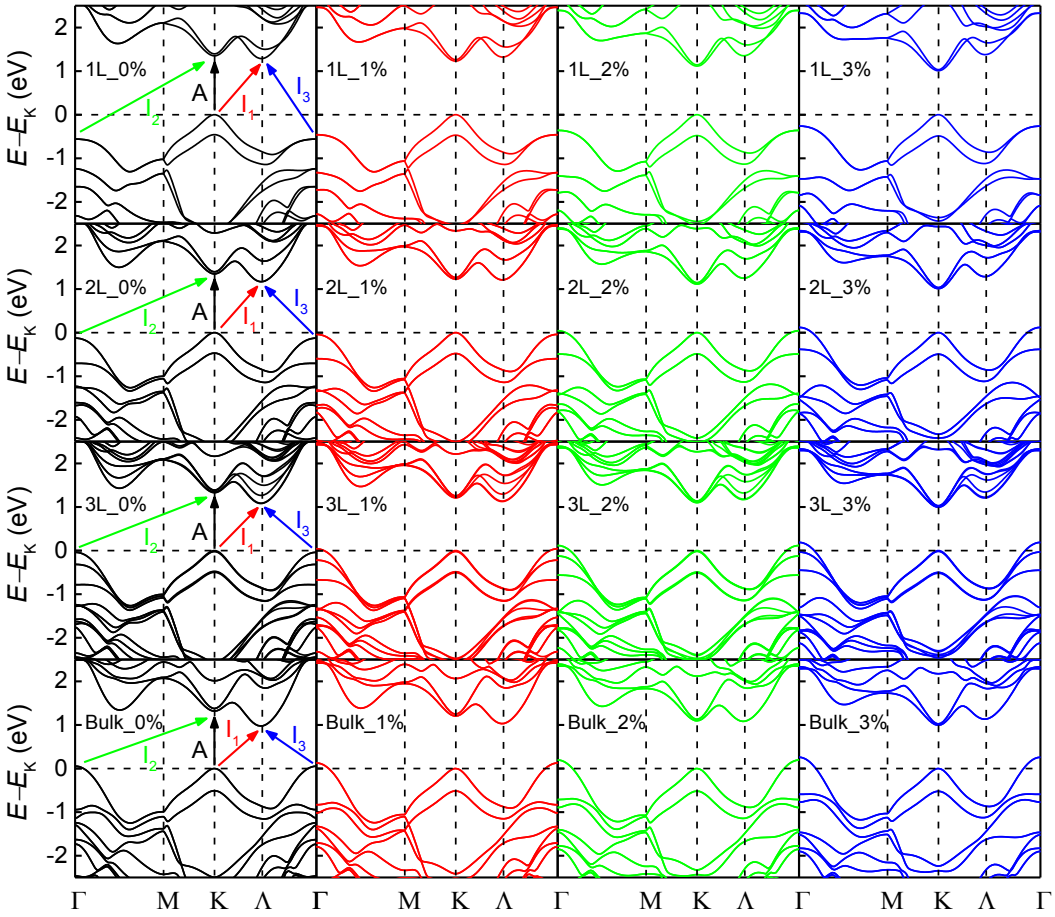

Figure 6-3. Computed electronic band structures of monolayer (1L; first row), bilayer (2L; second row), trilayer (3L; third row), and bulk (fourth row) WSe_2 with inclusion of the SOC under different biaxial tensile strains: 0% (first column), 1% (second column), 2% (third column), and 3% (fourth column). Energies are given relative to the local maximum of the uppermost valence band (UVB) around the K point. The arrows indicate the band gaps of direct (A) and indirect (I_1, I_2, and I_3) transitions.

It is worth noting that although the calculation based on a screened Coulomb Heyd-Scuseria-Ernzerof (HSE06) hybrid functional or GW approach can possibly fix the issue of the underestimation of band gaps, some reports show that these methods can also overestimate the band gaps sometimes [274, 275], and more importantly such computation methods are considerably computationally expensive. In addition, the band structures calculated by HSE06, GW, and PBE methods exhibit similar features except for the rigid shift of band gap energy [51, 275-277]. Here, instead of the absolute value of the band gap energy, the overall variation trend of band gaps with

respect to strain is the focus of this study, which can be predicted reliably with the PBE method [273, 276, 277]. Thus, the choice of the PBE exchange-correlation functional for this study is believed to be appropriate.

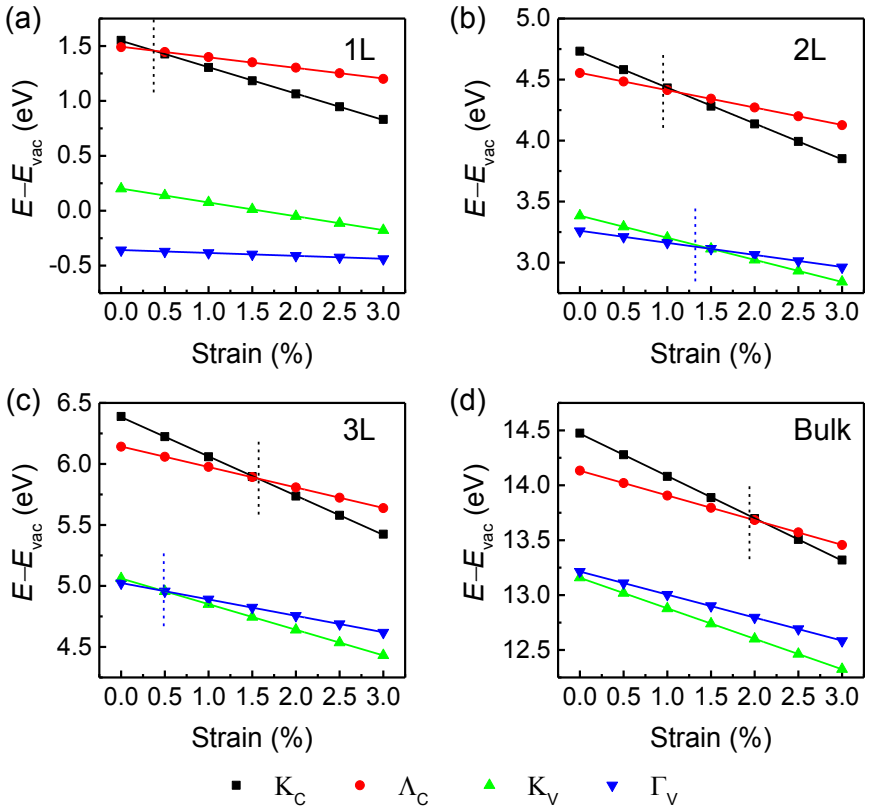

Figure 6-4 The band energies of the LCB and UVB of monolayer (1L; a), bilayer (2L; b), trilayer (3L; c) and bulk (d) WSe_2 at particular k points relative to the common vacuum level as a function of applied biaxial tensile strain. Straight lines are the linear fits of the computed results (scatters). The black (blue) vertical dashed lines indicate the shift of the CBM (VBM) from the Λ (K) to K (Γ) point.

Upon applying biaxial tensile strain, the LCB at the K (Λ) point moves down (up) and the UVB at the Γ point upshifts relative to the UVB at the K point, as shown in Figure 6-3. Continuous increase in strain can result in the shift of CBM from the Λ point to K point and VBM from the K point to Γ point. As a result, the occupancy of electrons or holes in each valley changes with strain correspondingly. In addition, the values of the critical strain correlating to the CBM and VBM relocation points are dependent on the number of layers. It can be seen from Figure 6-4, the crossover point of CBM

upshifts while VBM downshifts in strain as the number of WSe_2 layers increases. As the applied strain ranges from 0 to 3%, various transitions of lowest band gap have occurred for WSe_2 with different thicknesses (I_1–A for monolayer WSe_2, I_1–A–I_2 for bilayer WSe_2, I_1–I_3–I_2 for trilayer WSe_2, I_3–I_2 for bulk WSe_2), as shown in Figure 6-5, attributing to the dependence of the critical strains for the CBM and VBM shifts on the number of WSe_2 layers. Meanwhile, the spin splitting of the LCB at the Λ point and the UVB at the K point get enhanced while the LCB at the K point is weakened, as shown in Figure 6-6.

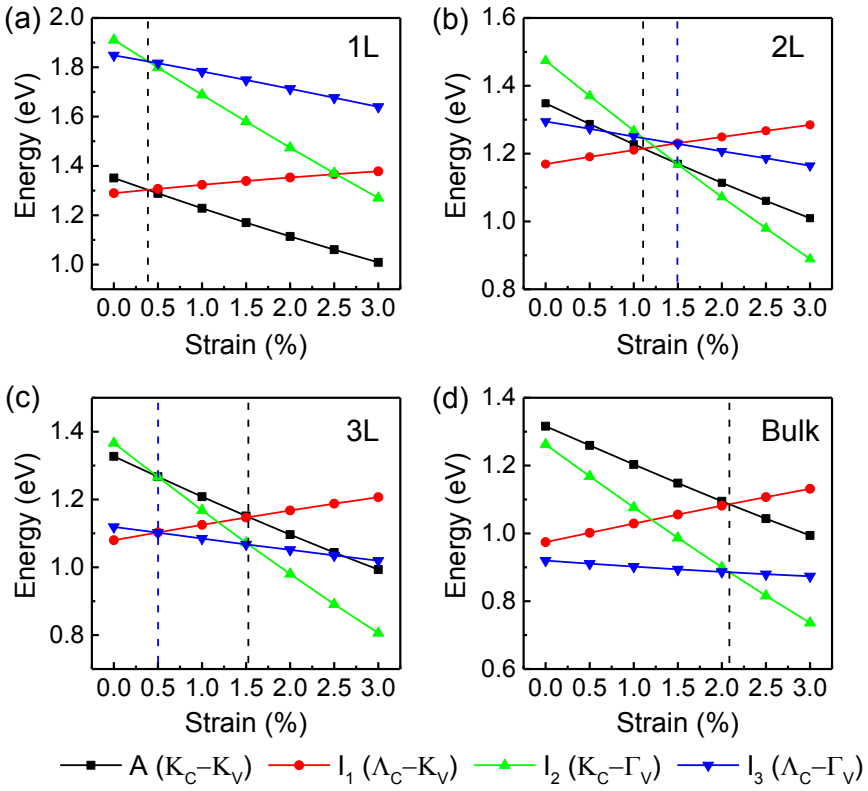

Figure 6-5. Computed band gaps for direct (A) and indirect (I_1, I_2 and I_3) transitions of monolayer (1L; a), bilayer (2L; b), trilayer (3L; c), and bulk WSe_2 (d) as a function of biaxial tensile strain ranging from 0 to 3% with inclusion of the SOC. The vertical dashed lines indicate the relocations of the CBM (black) and VBM (blue).

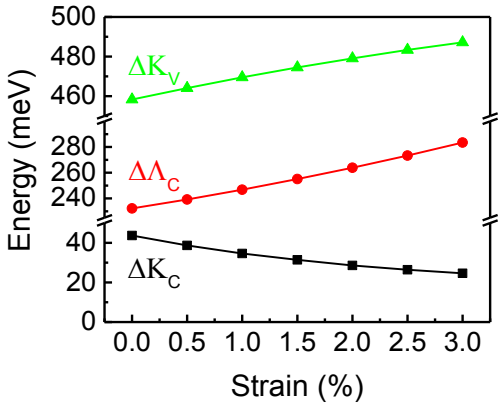

Figure 6-6. The spin-orbit splitting at various k points of the Brillouin zone (LCB at the K point, black; LCB at the Λ point, red; UVB at the K point, green) of monolayer WSe_2 as a function of biaxial tensile strain.

6.2.3.2 Projected DOS and band structure

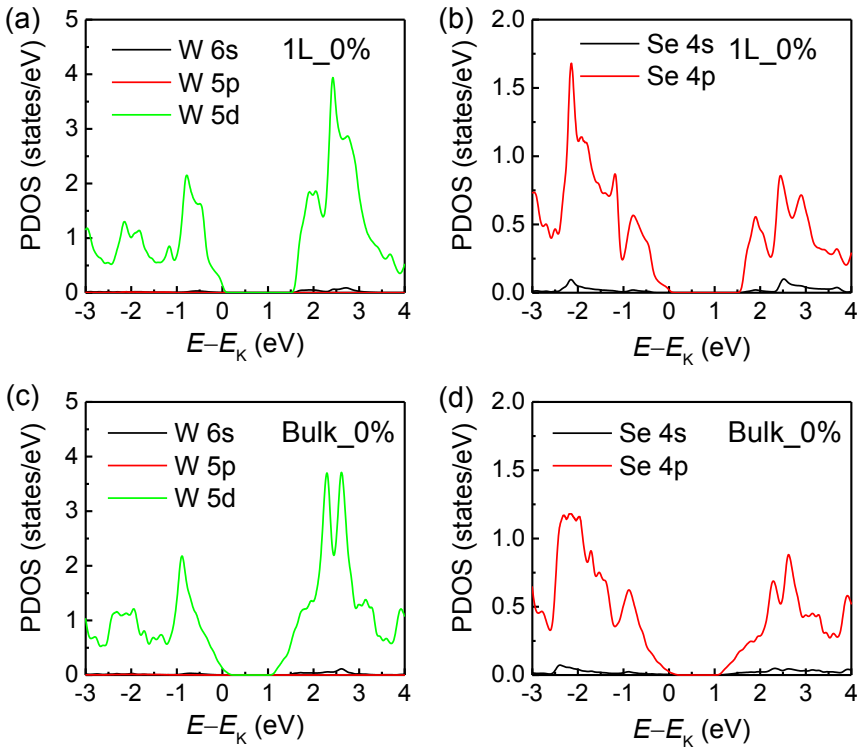

Figure 6-7. Atomic orbital projected DOS of W (a, c) and Se (b, d) atoms of the unstrained monolayer (1L; a, b) and bulk (c, d) WSe_2 without the SOC.

To gain more insights into the evolution of electronic properties of WSe_2 under strains, the atomic orbital projected DOS and band structure of WSe_2 have been computed (without inclusion of the SOC) and analyzed.

For the electronic bands near the Fermi level (upper part of valence band and lower part of conduction band), the electronic states of Se and W atoms are mainly contributed from Se 4p and W 5d atomic orbitals, respectively, as presented in Figure 6-7. Therefore, the study of the Se 4p and W 5d orbitals is focused in this section.

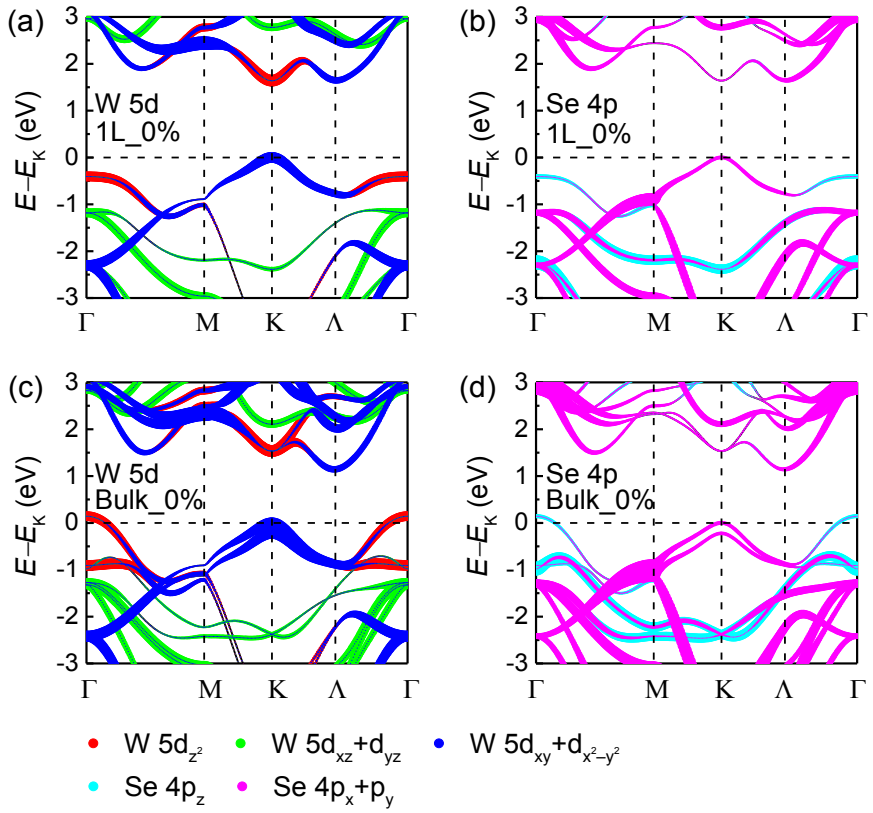

Figure 6-8. Atomic orbital projected band structures of W 5d (a, c) and Se 4p (b, d) orbitals of the unstrained monolayer (1L; a, b) and bulk (c, d) WSe_2. The line width is proportional to the projected weight of different atomic orbitals represented by distinct colours.

Figure 6-8 shows the projected band structures of W 5d and Se 4p orbitals of unstrained monolayer and bulk WSe_2. Although the VBM and CBM of WSe_2 with different numbers of layers may lie at distinct k points, the proportional contribution from various atomic orbitals to the UVB and LCB is analogical. The UVB at the K valley is dominated by the hybridization of bonding W $5d_{xy}+d_{x2-y2}$ and Se $4p_x+p_y$ orbitals,

while the UVB around the Γ point is mainly contributed from the bonding W $5d_{z2}$ and Se $4p_z$ orbitals. Meanwhile, the LCB at the K point primarily originates from the W $5d_{z2}$ orbitals plus minor contribution of the Se $4p_x+p_y$ orbital, and the local minimum of the LCB around the Λ point are favoured by the W $5d_{xy}+d_{x2-y2}$ and Se $4p_x+p_y$ orbitals. The contribution of W $5d_{xz}+d_{yz}$ orbital to the band edges can be negligible. In addition, the electronic states of W $5d_{z2}$ orbital near the LCB and UVB, as well as the Se $4p_z$ orbital at the UVB, move towards the centre of the band gap as tensile strain increases, as depicted in the projected DOS of monolayer (Figure 6-9) and bulk (Figure 6-10) WSe_2.

As the LCB and UVB around the K point are primarily composed of the 5d orbital of W atoms located in the middle of each atomic layer (Figure 6-1a) owning minimum interlayer coupling, increasing the number of WSe_2 layers almost does not affect the direct band gap at the K point. On the contrary, the UVB at the Γ point and LCB at the Λ point exhibit stronger interlayer coupling, due to relatively more contribution of the 4p orbital of S atoms that extends beyond the outmost planes of each WSe_2 layer. Therefore, the band gap energies of indirect I_1 (Λ_C–K_V) and I_2 (K_C–Γ_V) transitions present more sensitive dependence on the number of WSe_2 layers.

Application of tensile strain leads to the increase in W–Se bond length and thus the reduction in the overlap of atomic orbitals. Then the coupling between the bonding orbitals (W $5d_{z2}$ and Se $4p_z$; W $5d_{xy}+d_{x2-y2}$ and Se $4p_x+p_y$) is strengthened while the hybridization between the antibonding orbitals (W $5d_{z2}$ and Se $4p_x+p_y$) is weakened [278]. As a result, the band energy (Figure 6-3) and spin-orbit splitting (Figure 6-6) mainly contributed by the bonding orbitals (UVB at the K and Γ point and LCB at the Λ point) rise while the ones dominated by the antibonding orbitals (LCB near the K point) fall with increasing strain.

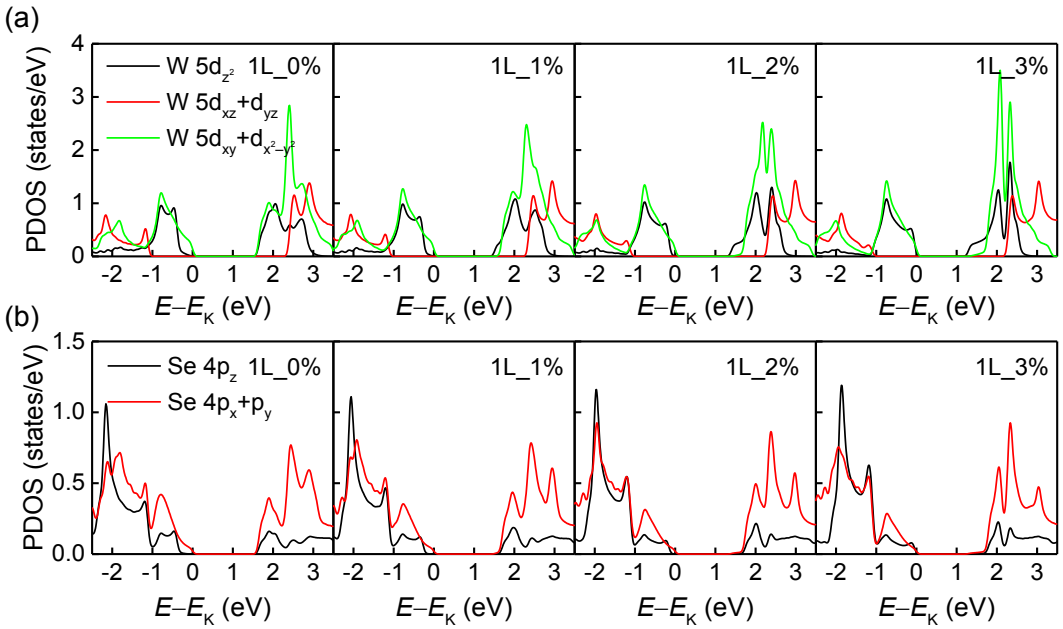

Figure 6-9. Atomic orbital projected DOS of W 5d (a) and Se 4p (b) orbitals of monolayer (1L) WSe_2 with respect to various biaxial tensile strains.

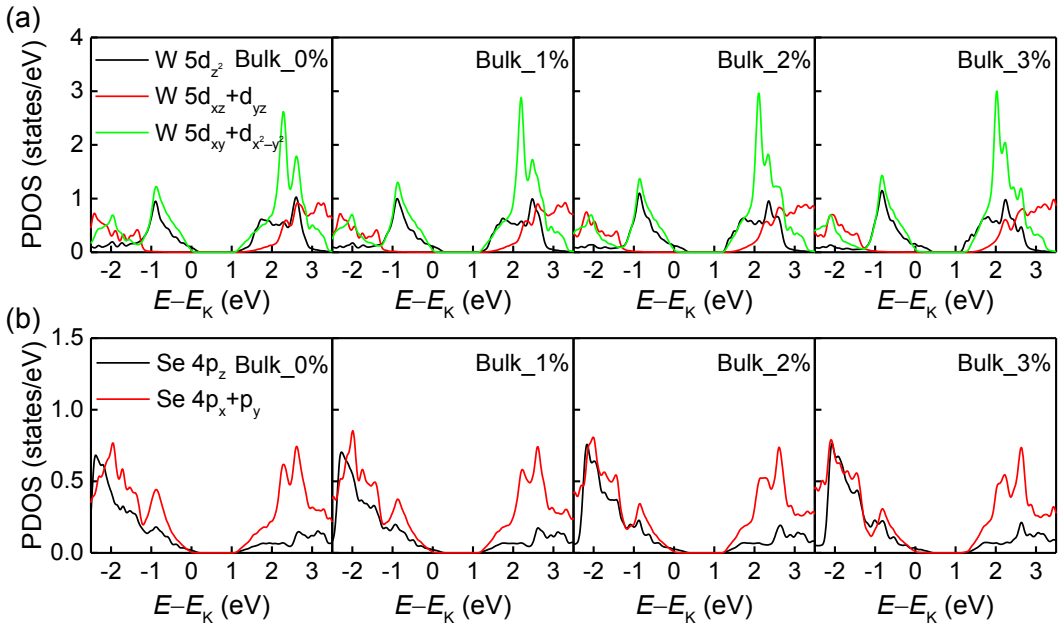

Figure 6-10. Atomic orbital projected DOS of W 5d (a) and Se 4p (b) orbitals of bulk WSe_2 with respect to various biaxial tensile strains.

6.2.4 Electrical transport property

Based on the calculated band structures, the electrical transport properties have been estimated by using the semi-classical Boltzmann transport theory within the constant relaxation time approximation and rigid band approximation, implemented in the BoltzTraP code [279]. Within this approximation, the electrical conductivity σ depends linearly on the relaxation time τ, and the relaxation time τ scaled in-plane conductivity (σ_{xx} / τ) is calculated.

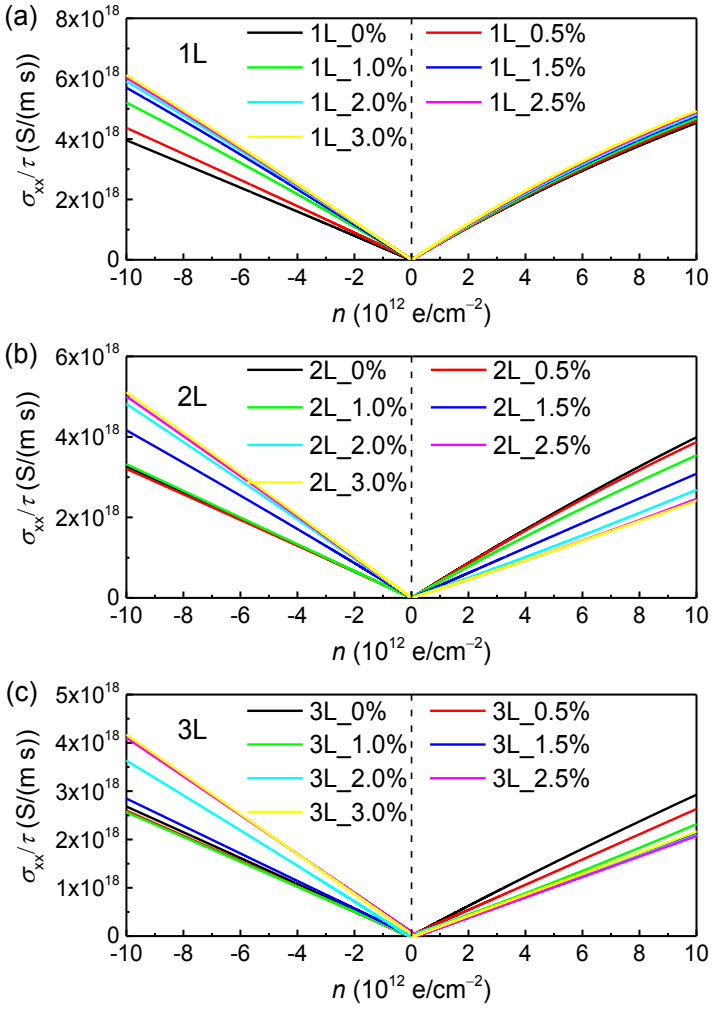

Figure 6-11. Relaxation time scaled in-plane conductivity (σ_{xx} / τ) as a function of doping density n ranging from -10^{13} cm^{-2} to $+10^{13}$ cm^{-2} for monolayer (1L; a), bilayer (2L; b), and trilayer (3L; c) WSe_2 under various levels of tensile strains at the temperature of 300 K.

Figure 6-11 shows the σ_{xx} / τ of 1~3-layer WSe_2 regarding the doping density (net carrier concentration) per unit area n ranging from -10^{13} cm^{-2} to $+10^{13}$ cm^{-2} at the temperature of 300 K. As can be seen, σ_{xx} / τ follows a positive linear relationship with the doping concentration n, which indicates that in such doping range the 1~3-layer WSe_2 system can be modelled as a 2D electron gas (electrons free to move in two dimensional but bound in the third). The calculated σ_{xx} / τ versus tensile strain ε for lightly-doped 1~3-layer WSe_2 with a net carrier concentration of $n = -2\times10^{12}$ cm^{-2} (electron) or $n = +2\times10^{12}$ cm^{-2} (hole) are plotted in Figure 6-12a-c. The σ_{xx} / τ of the n-doped WSe_2 show a drastic increase when the applied strain is near the crossover point where CBM shifts from the Λ point to K point (0~1.0% for monolayer WSe_2; 1.0~2.0% for bilayer WSe_2; 1.5~2.5% for trilayer WSe_2). However, application of tensile strain close to the relocation of VBM from the K point to Γ point (0.5~2.0% for bilayer; 0~1.5% for trilayer) results in an abrupt reduction in the σ_{xx} / τ of p-doped WSe_2. In addition, in the region relatively far ahead of the CBM (VBM) relocation ($\leq$ 0.5% for n-doped bilayer and trilayer WSe_2; $\leq$ 3% for p-doped monolayer WSe_2), the σ_{xx} / τ of n-doped (p-doped) WSe_2 decreases (increases) gradually as the tensile strain increases. Whereas, after the relocation of the CBM and VBM ($\geq$ 2.0% strain for n-doped monolayer WSe_2; $\geq$ 2.5% for p-doped trilayer WSe_2), the σ_{xx} / τ of both n- and p-doped WSe_2 shows a rising trend with increasing tensile strain.

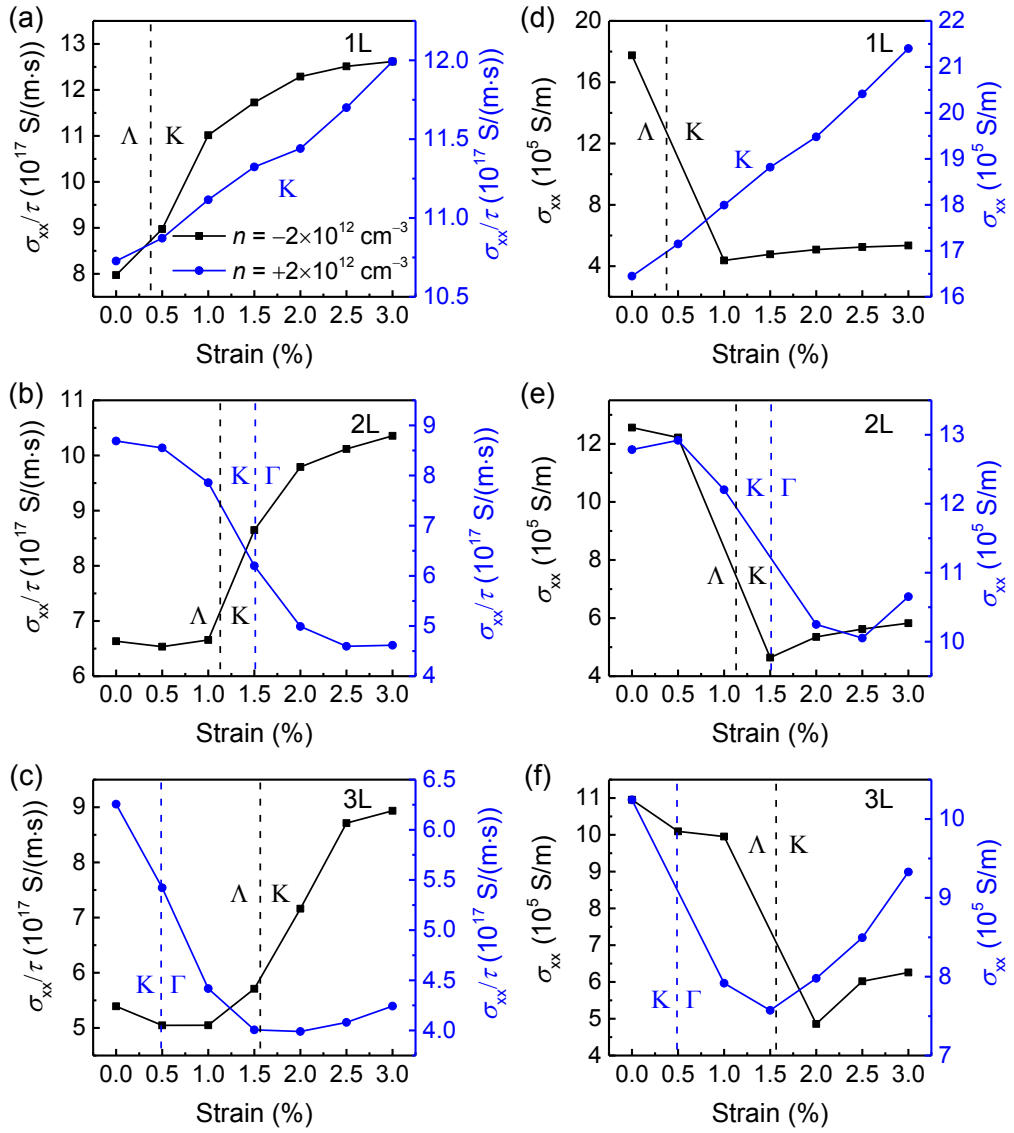

Figure 6-12. Relaxation time scaled in-plane conductivity σ_{xx} / τ (a-c) and calculated in-plane conductivity σ_{xx} (d-f) of n-doped (black plots) and p-doped (blue plots) 1~3-layer WSe_2 as a function of biaxial tensile strain at the temperature of 300 K with net carrier concentrations of $n = -2\times10^{12}$ cm^{-2} (electron, black) and $n = +2\times10^{12}$ cm^{-2} (hole, blue), respectively. Vertical dashed lines indicate the CBM (black) and VBM (blue) relocation points.

In order to estimate the relaxation time τ, the acoustic-phonon-limited carrier mobility μ is calculated analytically using the deformation potential (DP) theory (because the coherent wavelength of thermally activated carriers at room temperature is close to the acoustic phonon wavelength and way larger than the lattice constant) [280]. Based on

the DP theory, the mobility of 2D materials has been extensively evaluated with the following expression [281-285]:

$$\mu_{2D} = \frac{2e\hbar}{3E_1^2 k_B T \left|m^*\right|^2}, \tag{5-1}$$

where e is the elementary charge, $\hbar$ is the reduced Planck constant, k_B is the Boltzmann constant, T is the temperature. m^* represents the effective mass of the carriers which can be approximated from $m^* = \hbar$ [illegible] (parabolic dispersion) in case of the 2D electron gas, where $E(\vec{\kappa})$ is the band energy of the CBM (VBM) with respect to the vacuum level at the wavevector $\vec{\kappa}$ for electron (hole). The DP constant E_1 of the VBM for hole and CBM for electron is defined by $E_1 = \partial E(\vec{\kappa})/\partial\varepsilon$, describing the band energy shift rate of the VBM or CBM under strain ε, extracted by linear fittings of the data in Figure 6-4. The term C_{2D} is the 2D elastic modulus, which is determined by quadratic fittings of total energy increase versus strain curve with the expression of $(E_{str} - E_0)/S_0 = C_{2D}\varepsilon^2/2$, as shown in Figure 6-13, where $E_{str} - E_0$ is the total energy variation of the cell caused by application of strain ε, and S_0 is the lattice area in the x-y plane of the unstrained cell. It is worth noting that since the Equation (5-1) only considers the coupling between free carriers and acoustic phonons, it can overestimate the carrier mobility considering that in reality, carriers can also be scattered by other factors such as defects.

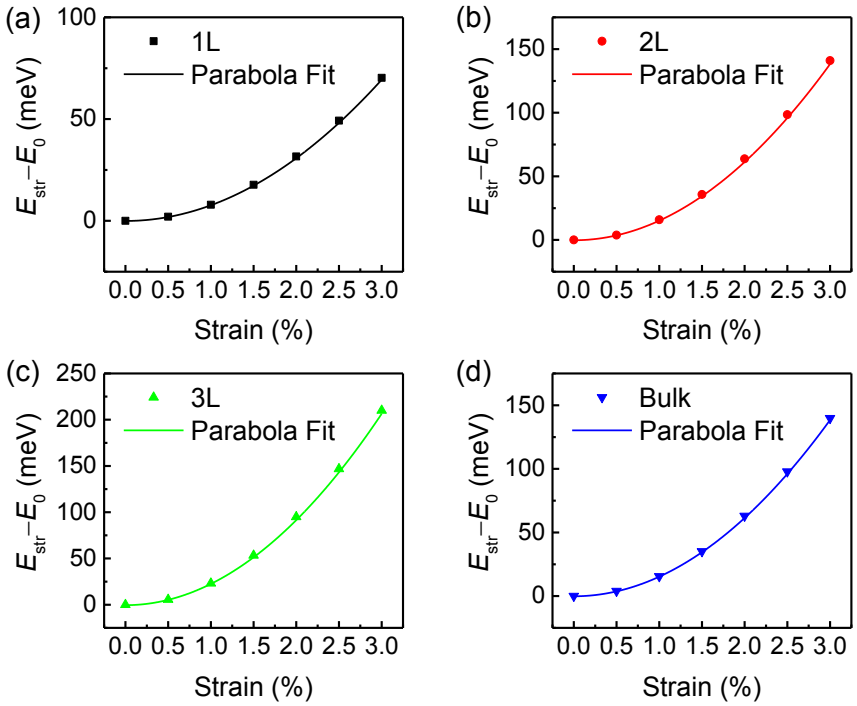

Figure 6-13. The plots of total energy changes ($E_{str} - E_0$) of monolayer (1L; a), bilayer (2L; b), trilayer (3L; c), and bulk (d) WSe_2 under different levels of tensile strain (scatters) and corresponding parabolic fits (solid lines).

Subsequently, the relaxation time τ can be estimated from the calculated 2D carrier mobility μ_{2D} by the relation of $\tau = m^*\mu_{2D}/e$. The calculated values of DP constant E_1, effective mass m^*, 2D carrier mobility μ_{2D}, and relaxation time τ of 1~3-layer WSe_2 under different levels of strain are listed in Table 6-2. Note that when the energy differences between the local maxima of the UVB at the K point and Γ point is small (around the VBM relocation point), the doping holes may occupy both the K and Γ valleys simultaneously, which is not applicable to the DP theory. Thus, the data lying in such region have not been taken into account. Similarly, the data have also been omitted where the energies of the local minima of the LCB at the Λ point and K point are proximal.

After the relaxation time τ is estimated, the in-plane conductivity σ_{xx} can be obtained with the previously calculated σ_{xx} / τ. Figure 6-12d-e show the plots of in-plane conductivity σ_{xx} versus strain ε for lightly n- and p-doped 1~3-layer WSe_2 with a carrier concentration of $n = -2\times10^{12}$ cm^{-2} (electron) or $n = +2\times10^{12}$ cm^{-2} (hole). For unstrained 1~3-layer WSe_2 with light n-doping, doping electrons first occupy the

valley at the Λ point where the CBM is located. Then the K valley becomes to be favoured by doping electrons after the CBM shifts from the Λ point to K point induced by tensile strain where the electrons possess much (≥ 3 times) shorter relaxation time τ. For this reason, the strain induced CBM shift can result in considerable reductions in electron conductivity at the strain range of 0~1.0% for monolayer, 0.5~1.5% for bilayer and 1.0~2.0% for trilayer WSe_2, as observed from Figure 6-12d-e. Far from the shift of the CBM, the effective mass m^* as well as the relaxation time τ of the electrons show negative (positive) relationship with tensile strain before (after) the CBM relocation, as listed in Table 6-2, following the same tendency of σ_{xx} / τ versus ε (Figure 6-12a-c), which contributes to a similar overall relationship of $\sigma_{xx} - \varepsilon$ to $\sigma_{xx} / \tau - \varepsilon$ in such range.

In contrast, the relaxation time τ of the holes of p-doped WSe_2 occupying the K valley is close to (slightly longer) that filling the Γ valley. Therefore, during the relocation of the VBM from the K point to Γ point (1.0~2.0% strain for bilayer WSe_2; 0~1.0% strain for trilayer WSe_2), the conductivity σ_{xx} of p-doped WSe_2 has not been affected significantly. Outside the region of the VBM shift, the relaxation time τ increases as the strain increases, like σ_{xx} / τ. The above factors result in the similar relationship of σ_{xx} versus ε to σ_{xx} / τ versus ε for p-doped WSe_2 across the whole strain range (0~3%), regardless of the number of WSe_2 layers. The above calculated results can provide a guideline for tuning the performance of future WSe_2 based strain sensor by varying the thickness or type of carriers of WSe_2. It can also be concluded that compared to the p-doped WSe_2, in general, n-doped WSe_2 exhibits a greater sensitivity of the conductivity to the applied tensile strain with the maximum calculated gauge factor being ≈305, ≈160, and ≈105 for n-doped monolayer, bilayer, and trilayer WSe_2, respectively, which is higher than that of 2D MoS_2 (148 for monolayer and 44 for trilayer) [70] and graphene (≈2) [65-69]. Therefore, 2D WSe_2 is more promising for sensitive strain sensor applications.

Table 6-2. Deformation potential (DP) constant E_1, effective mass m^*, 2D carrier mobility μ_{2D}, and relaxation time τ for hole and electron of lightly-doped 1~3-layer WSe_2 under different levels of tensile strain.

Number of layers	**Strain (%)**	**Carrier**	E_1 **(eV)**	m^* **(**m_e**)**	μ **(cm^2/V·s)**	**τ (ps)**
1	0	Hole	−12.606	−0.373	72.413	1.533
		Electron	−9.636	0.439	89.263	2.227
	1	Hole	−12.606	−0.353	80.689	1.619
		Electron	−24.020	0.396	17.651	0.397
	2	Hole	−12.606	−0.336	89.274	1.703
		Electron	−24.020	0.381	19.134	0.414
	3	Hole	−12.606	−0.321	98.052	1.784
		Electron	−24.020	0.371	20.107	0.424
2	0	Hole	−18.09	−0.377	68.820	1.472
		Electron	−14.237	0.473	70.565	1.893
	1	Hole	−18.09	−0.357	76.631	1.553
		Electron	N/A	N/A	N/A	N/A
	2	Hole	−9.894	−0.902	40.087	2.053
		Electron	−29.402	0.384	25.090	0.547
	3	Hole	−9.894	−0.803	50.597	2.307
		Electron	−29.402	0.373	26.567	0.563
3	0	Hole	−21.014	−0.375	76.947	1.637
		Electron	−16.780	0.474	75.4716	2.031
	1	Hole	−13.454	−0.835	37.793	1.792
		Electron	−16.780	0.488	71.110	1.971
	2	Hole	−13.454	−0.749	47.059	2.000
		Electron	−32.164	0.386	30.960	0.679
	3	Hole	−13.454	−0.681	56.856	2.199
		Electron	−32.164	0.374	32.965	0.700

Note that the experimental conductivity of pristine 7-layer WSe_2 has been extracted to be ≈0.5 S/m when V_{GS} = 0V with the free electron carrier concentration of 1.03×10^{11} cm^{-2} as presented in Figure 4-16a. While the DFT calculated conductivity under the same electron carrier concentration is 7.1×10^4, 7.0×10^4, and 5.0×10^4 S/m for unstrained monolayer, bilayer, and trilayer WSe_2, respectively based on the calculated results of σ_{xx} / τ (Figure 6-11) and τ (Table 6-2). The overestimation of the calculated conductivity is possibly due to not inclusion of crystals defects, fabrication residue, charge scattering sites existing at the WSe_2/SiO_2 interface, water adsorbates from the ambient environment, and etc. in the DFT model. However, the variation trend of the conductivity of 2D WSe_2 as a function of tensile strain is focused here, which can be predicted with the employed DFT calculation.

6.3 Field-effect doping

This section will move on to the discussion of the influence of field-effect doping on the crystal structure, band structure, conductive channel size, and electrical transport property of 2D WSe_2.

6.3.1 Computational methods

Figure 6-14 shows a simple configuration of the field-effect doping calculation, in which a crystal system is separated from a gate electrode by a dielectric layer. Application of a gate voltage V_{GS} results in the misalignment of the Fermi levels of the gate electrode and the system. For this reason, opposite charges gather around the gate/dielectric and dielectric/system interfaces. At the system side, the field-effect doping charge per unit area n as a function of the applied gate voltage V_{GS} can be described with the expression below:

$$n = \begin{cases} C\left(V_C - V_{GS}\right) & \text{if } V_{GS} > V_C \\ C\left(V_V - V_{GS}\right) & \text{if } V_{GS} < V_V \\ 0 & \text{else} \end{cases}, \tag{5-2}$$

where V_C and V_V are the potential extrema to fill the CBM and VBM of the system, respectively. C represents the capacitance per unit area of the dielectric layer determined by $C = \varepsilon_0\varepsilon_r/d$, where ε_0 is the vacuum permittivity, ε_r is the dielectric

constant depending on the type of the gate dielectric material, and d is the dielectric thickness. In the dielectric layer, a constant electric field exists due to the formation of opposite charges at the left and right sides of the dielectric layer, and hence the potential in the dielectric layer increases or decreases monotonously along the z-direction. However, the potential changes rapidly at the dielectric/system interface due to the nonuniform distribution of the doping charges inside the crystal system close to the dielectric layer. On the contrast, for the region relatively far away from the dielectric/system interface where doping charges barely exist in the system, the potential in the system oscillates periodically dominated by the periodic distribution of the ions of the system.

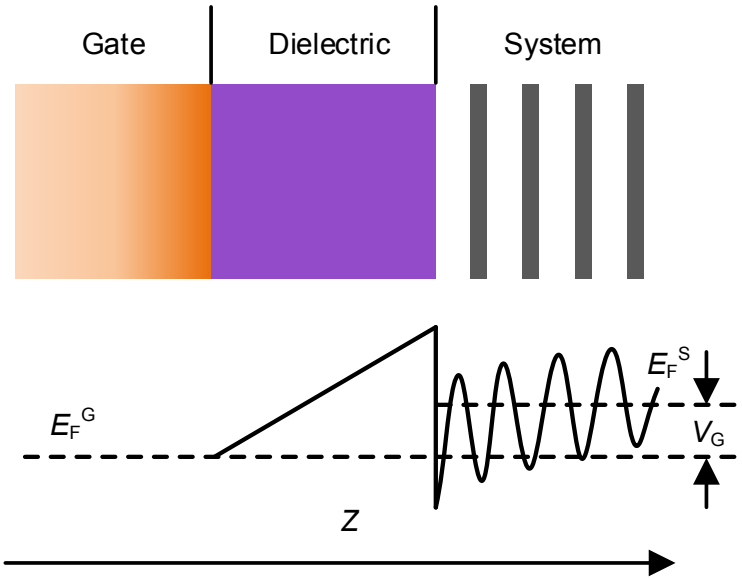

Figure 6-14. Top: Schematic diagram of a field-effect configuration including a gate, a dielectric layer, and a crystal system. Bottom: The Fermi energies of the gate and crystal system (dashed lines) together with electrostatic potential in the dielectric layer and crystal system along the z-direction (solid lines). Adapted from [286].

To describe such FET configuration using the DFT method within the periodic boundary condition, a simplified model [286] has been used as shown in Figure 6-15. The gate electrode has been modelled as a charged plate to simulate the charge formed at the gate/dielectric interface when gate voltage V_{GS} is applied. The charged plate is positioned at $z_{gate} = 0.011\ L_z$, where L_z is the size of the unit cell in the z-direction and

meanwhile, possesses the same amount of charges as the doping charges in the crystal system but with an opposite polarity. Then the dielectric layer is simplified as a potential barrier with a width d_b of 0.1 L_z and an energy height of 3 Ry to prevent the ions in the system moving too close to the charged plate during the structural relaxation of the system under field-effects. Within the periodic boundary condition, the doped system can interact with nearby periodically imaged charged plate in the z-direction producing an artificial electric field, which disagrees with the real situation where the electric field should be zero in the vacuum region far from the crystal system. To cancel such artificial electric field, an electric dipole (formed by two oppositely charged planes) has been inserted at the back of the gate electrode (z_{diploe} = 0~0.1 L_z) to avoid the interaction between the doped system and the next imaged charged plate. With this model, the crystal structure of 1~3-layer WSe_2 under various degrees of field-effect have been optimized. Subsequently, the non-self-consistent calculations of the optimized structures have been performed with inclusion of the SOC to obtain the electronic band structure and spatial distribution of the doping charges. At last, the electrical transport property of the field-effect doped WSe_2 has been computed.

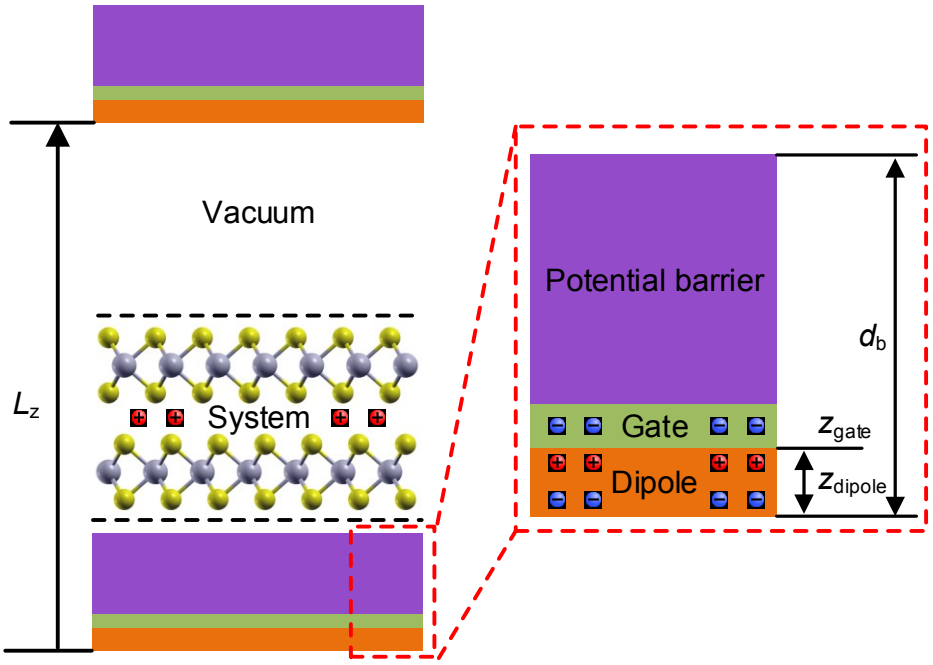

Figure 6-15. Schematic of the DFT model (not to scale) employed for the computation of the p-type field-effect doping of a bilayer WSe_2.

6.3.2 Structural geometry

Figure 6-16 shows the variations of three selected structural parameters of trilayer WSe_2 as a function of the field-effect doping density n. As presented in Figure 6-16a, application of gate voltage V_{GS} results in discrepancies of W–Se bond length $d_{W–Se}$ (and hence the Se–W–Se bond angle θ) not only among different atomic layers but also between the top and bottom W–Se pyramids in the same atomic layer. Moreover, the W–Se bond length $d_{W–Se}$ of the W–Se pyramid closest to the dielectric (the bottom pyramid of the first layer) has been observed to undergo the most considerable change under the field-effect and exhibit a positive relationship with the field-effect doping density n. Compared to the first layer, the W–Se bond length $d_{W–Se}$ of the second layer shows slight variations with different doping densities, and the $d_{W–Se}$ for the third layer even stays almost unchanged. Similar behaviour has been observed for the Se–Se intralayer distance $d_{Se–Se}$ and interlayer separation L, whose significant changes occur closest to the dielectric, as shown in Figure 6-16b and Figure 6-16c, respectively. Increasing doping charge density leads to further Se–Se intralayer distance $d_{Se–Se}$ in the first layer and reduction in the interlayer separation L between the first and second layers. However, the Se–Se intralayer distance $d_{Se–Se}$ in the third layer and the interlayer separation L between the second and third layers are nearly constant under varying doping density. The above phenomenon has also been found from monolayer and bilayer WSe_2. Note that, such structural changes under field-effects can contribute to the loss of crystal symmetries, namely, the mirror symmetry and inversion symmetry for WSe_2 with odd and even number of layers, respectively. It has been reported that the piezoelectric property can be observed in TMDs with an odd number of layers only, arising from the broken inversion symmetry [30, 75]. In the condition of the field-effect doping induced symmetry breaking, the piezoelectric property is predicted to be observed in WSe_2 with an even number of layers.

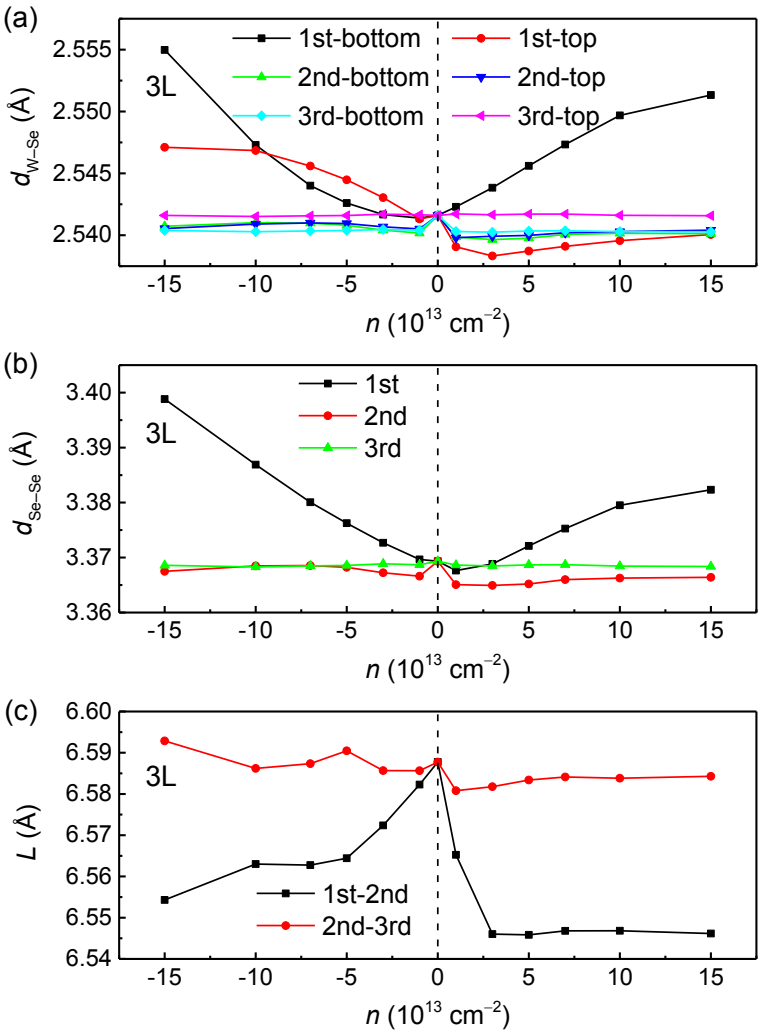

Figure 6-16. The W–Se bond length d_{W-Se} (a), Se–Se intralayer distance d_{Se-Se} (b), and interlayer separation L (c), as defined in Figure 6-1a, of trilayer (3L) WSe_2 versus field-effect doping concentration n. 1st, 2nd, and 3rd in the legends of figures indicate the order of the atomic layers closet to the dielectric.

6.3.3 Electronic band structure

Figure 6-17 and Figure 6-18 present the influence of n- and p-type field-effect doping on the electronic band structures of 1~3-layer WSe_2, respectively. As can be seen, field-effect does not merely act as rigid doping but also modifies the shape of the band structures. Figure 6-19 shows the band energies of the local minima and maxima of the LCB and UVB at special k points with respect to the Fermi levels under different degrees of field-effect doping. For n-type doping, the doping electrons solely occupy

the LCB at the Λ valley of 1~3-layer WSe_2, while the K valley first approaches and then reverses away from the Fermi levels with increasing doping density *n*, as shown in Figure 6-17 and Figure 6-19. In contrast to the n-type doping, the doping holes in the p-type doping first occupy the VBM valley at the K point then both the K and Γ valleys get occupied as the hole doping density keeps increasing (Figure 6-18 and Figure 6-19). In addition, fewer doping holes are needed to occupy the Γ valley for WSe_2 with more number of layers (≈9×10^{13} cm^{-2} for monolayer WSe_2, ≈3×10^{13} cm^{-2} for bilayer WSe_2, ≈2×10^{13} cm^{-2} for trilayer WSe_2) due to the smaller energy difference between the local maxima of the UVB at the K and Γ points.

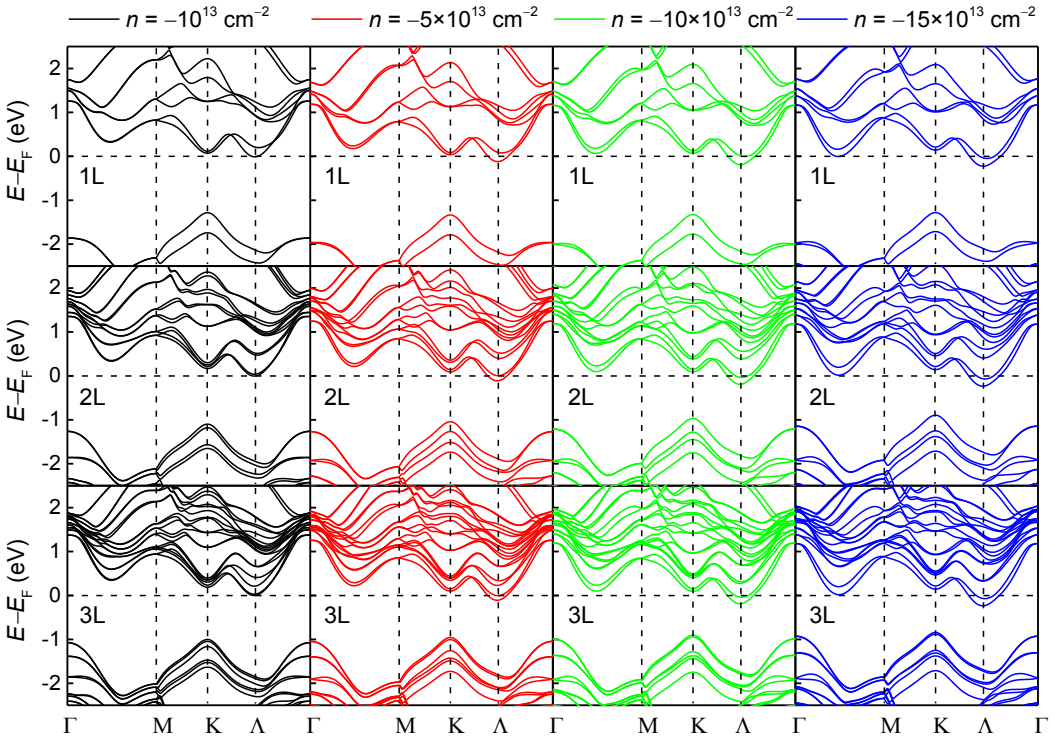

Figure 6-17. Calculated electronic band structures of monolayer (1L; top row), bilayer (2L; middle row), and trilayer (3L; bottom row) WSe_2 with inclusion of the SOC effect under different degrees of n-type field-effect doping. Energies are given with reference to the Fermi levels.

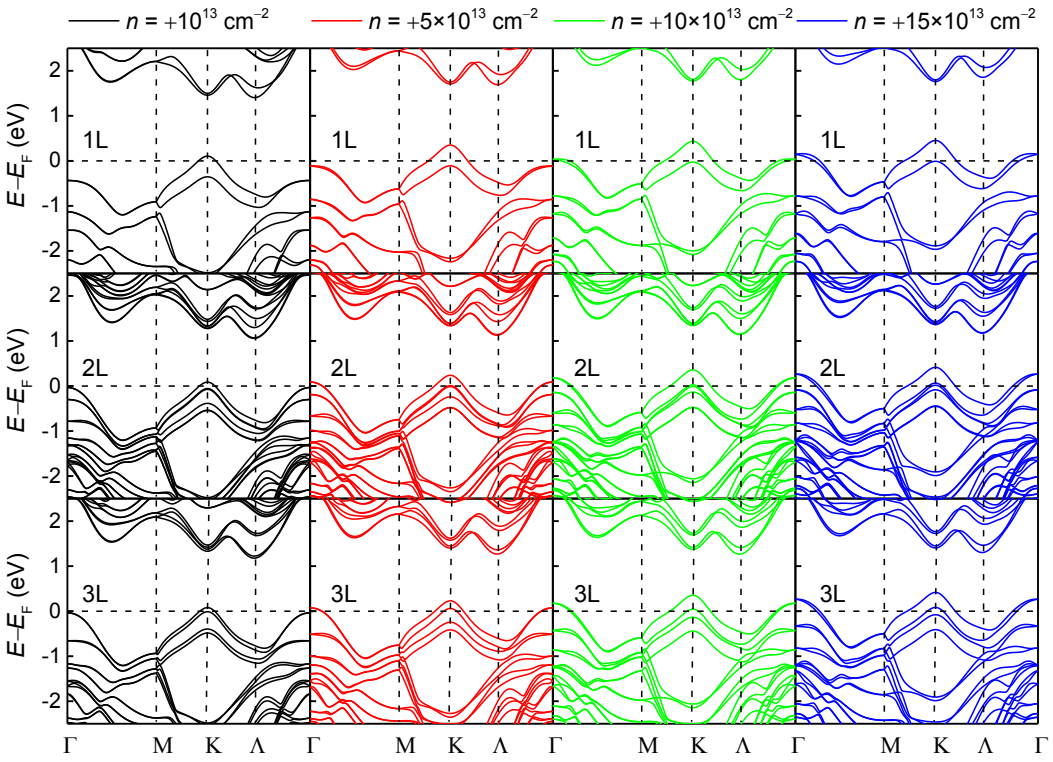

Figure 6-18. Calculated electronic band structures of monolayer (1L; top row), bilayer (2L; middle row), and trilayer (3L; bottom row) WSe_2 with inclusion of the SOC effect under different degrees of p-type field-effect doping. Energies are given with reference to the Fermi levels.

In addition, distinct from the Figure 6-2, spin-orbit splitting appears in bilayer WSe_2 resulting from the field-effect induced broken inversion symmetry. Figure 6-20 depicts the spin-orbit splitting of the LCB at the K (black) and Λ points (red) together with the UVB at the K point (green) of 1~3-layer WSe_2 as a function of the field-effect doping density *n*. The spin-orbit splitting of the UVB at the K point increases monotonically as the hole doping density increases, while the LCB at the K and Λ points shows distinct behaviour for n-doped WSe_2 with different numbers of layers. More interestingly, the spin-orbit splitting of the LCB at the K point for trilayer WSe_2 first gets weakened and then enhanced with increasing levels of n-type field-effect. The reason for this phenomenon needs to be studied systematically in the future. Moreover, bilayer and trilayer WSe_2 have been observed to possess greater sensitivities of the spin-orbit splitting to the field-effect compared to monolayer WSe_2, which might attribute from larger degree of symmetry breaking in multilayer WSe_2. As the spin-

orbit splitting affects the spin-polarized carrier populations (larger spin splitting increases the spin polarization of the carriers) [11], multilayer WSe_2 can be a promising candidate for gate-controlled spintronic devices.

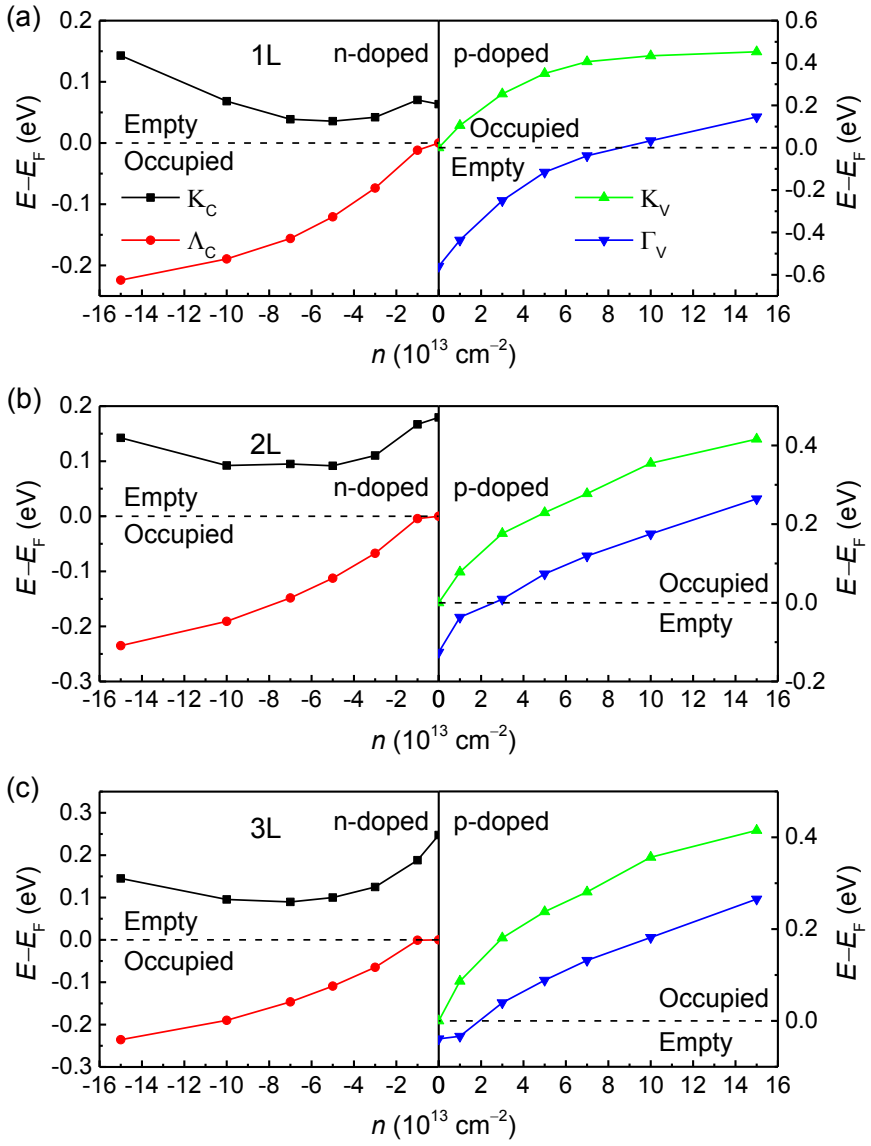

Figure 6-19. The band energies of the LCB at the K (black) and Λ (red) points as well as the UVB at the K (green) and Γ (blue) points of monolayer (1L; a), bilayer (2L; b), and trilayer (3L; c) WSe_2 with reference to the Fermi level versus the field-effect doping density *n*. The horizontal dashed lines indicate the Fermi levels. For n-type (p-type) doping, the valleys with band energies below (above) the Fermi levels are occupied by doping electrons (holes).

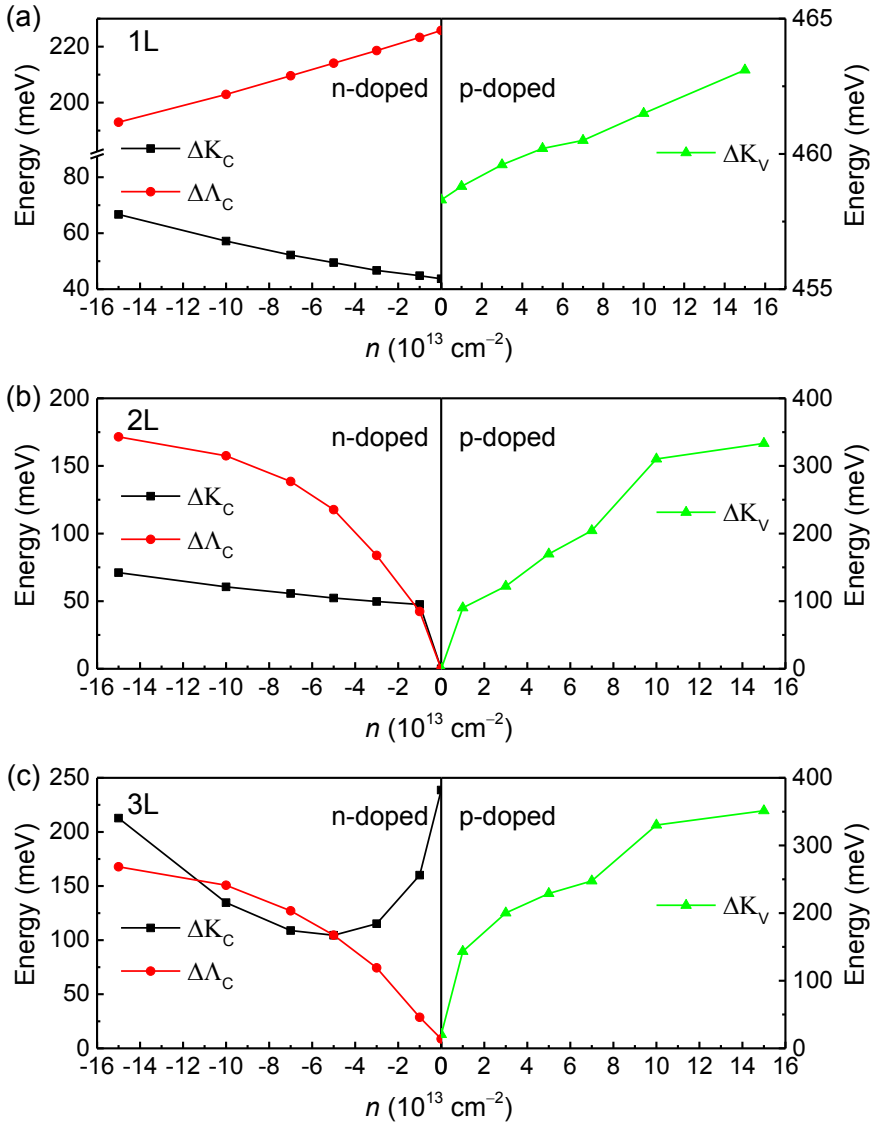

Figure 6-20. The spin-orbit splitting at various k points (LCB at the K point, black; LCB at the Λ point, red; UVB at the K point, green) of monolayer (1L; a), bilayer (2L; b), and trilayer (3L; c) WSe_2 as a function of field-effect doping density *n*.

6.3.4 Doping charge distribution

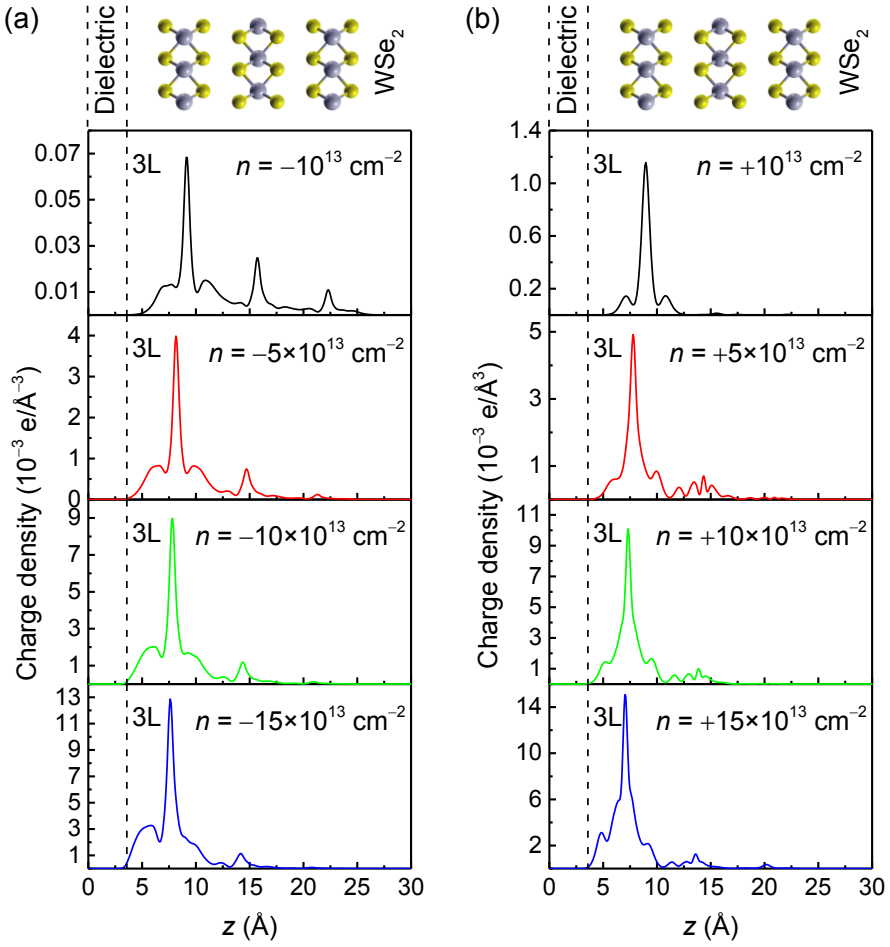

Figure 6-21. The planar-averaged distribution of n-type (a) and p-type (b) field-effect doping charges along the z-direction of trilayer WSe_2. The vertical dashed lines indicate the left and right boundaries of the dielectric layer. The schematics of trilayer WSe_2 crystal at the top of each figure show the location of the ions of undoped trilayer WSe_2.

Figure 6-21 shows the planar-averaged distribution of the doping charges along the z-direction of trilayer WSe_2 under different levels of field-effect doping. As can be seen, in the same atomic layer, the doping charges mainly localize around the W atoms and fewer around the Se atoms. For the case of light electron doping (the first row of Figure 6-21a), most of the doping charges are located asymmetrically around the W atoms within the first layer (closest to the dielectric) with fewer occupancies within the second and third layers. As the electron doping density increases, the localization and asymmetric distribution of the doping charges in the first layer become more

prominent. When the electron doping density reaches -15×10^{13} cm^{-2} (the bottom row of Figure 6-21a), the distribution of the doping charges on the third layer is almost negligible. Distinct from the n-type field effect doping, the doping charges for the light p-type doping (the first row of Figure 6-21b) are mainly localized within the first layer symmetrically around the W atoms with negligible occupancies of the doping charges within the second and third layers. Further increase in the hole doping density results in the asymmetric distribution of the doping charges in the first layer. Note that, such localization behaviour of the doping charges in WSe_2 also contributes to the observed most notable structural change in the first layer (Figure 6-16). In addition, the whole WSe_2 system moves closer to the dielectric as the doping level increases for both n- and p-type doping.

Figure 6-22 gives the proportional distribution of field-effect doping charges within each atomic layer of trilayer WSe_2. When the WSe_2 is lightly n-doped ($n = -10^{13}$ cm^{-2}), two-thirds of the doping charges occupy the first layer approximately with the least occupancy in the third layer. Increasing the n-type doping level results in stronger localization of the doping electrons in the first layer and thus thinner conductive channels. In contrast, for the p-type doping, the doping holes are mainly located in the first layer with initial light hole doping ($n = +10^{13}$ cm^{-2}). With increasing hole doping level, a decrease in the relative proportion of the doping holes in the first layer has been observed in the beginning. However, after the doping density is above $+7\times10^{13}$ cm^{-2}, the relative proportion of the doping holes in the first layer starts to exhibit a positive relationship with the doping density n. The reason for such result is possibly due to the conversion of sole occupancy of the doping holes at the K valley to the occupancy at both the K and Γ valleys with increasing doping hole density, as observed previously in Figure 6-19. As discussed before, the states at the K valley of the UVB are mainly contributed by the in-plane states, namely, W $5d_{xy}+d_{x2-y2}$ and Se $4p_x+p_y$ orbitals, which own a weaker hybridization between the layers. Whereas, the holes located at the Γ valley are featured with out-of-plane contributions (W $5d_{z2}$ and Se $4p_z$ orbitals) with stronger hybridization between the atomic layers. For this reason, the doping holes are localized within the first layer when the K valley is occupied only, while the occupancy of the Γ valley makes the conductive channel expand from the first layer to few layers. However, further increasing the doping density (above

$+7\times10^{13}$ cm^{-2}) leads to more substantial screening of the gate electric field, for which reason the doping holes tend to get localized towards the first layer once again contributing to the thinning of the conductive channel.

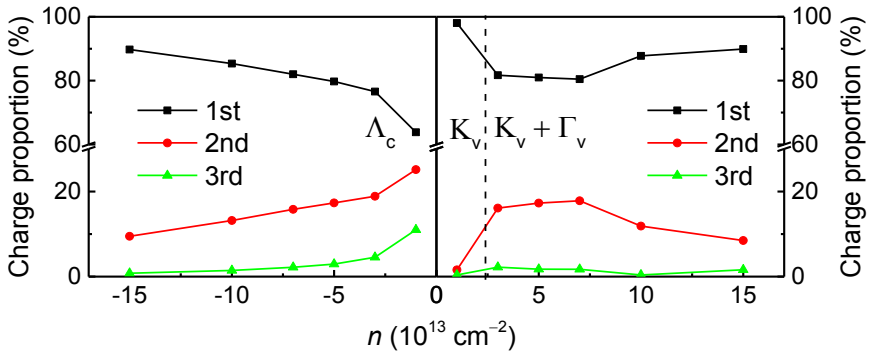

Figure 6-22. The proportions of the field-effect doping charges present in each atomic layer of trilayer WSe_2 as a function of the doping charge density n. 1st, 2nd, and 3rd in the legends of figures indicate the order of atomic layers closest to the dielectrics. The vertical dashed line indicates the starting point of the doping holes occupancy at both the K and Γ valleys.

6.3.5 Electrical transport property

In this section, the influence of field-effect on the electrical transport properties of 1~3-layer WSe_2 will be discussed. Figure 6-23 shows the relationship of the calculated relaxation time scaled in-plane conductivities (σ_{xx} / τ) of 1~3-layer WSe_2 versus the field-effect doping density n ranging from -15×10^{13} cm^{-2} to $+15\times10^{13}$ cm^{-2} at the temperature of 300 K. As can be seen, under same levels of field-effect doping, the conductivity is higher for WSe_2 with less number of layer. In addition, for both n- and p-type doping, the σ_{xx} / τ increases nonlinearly as the doping density n increases, with the increase rate for n-type doping being faster whereas the nonlinearity for p-type doping being more pronounced, which is distinct from Figure 6-11. This nonlinearity might be induced by the factors below: (1) the deviation of the electronic bands from the pure parabolic dispersion under field-effect; (2) the occupancy of the doping charge at multiple bands at the same k point when the n-type doping is in high level (fourth column of Figure 6-17); (3) the occupancy of the doping charges at multiple valleys located at different k points observed in the p-type doping (third and fourth columns of Figure 6-18). Note that, in such case, the effective mass m^* of the WSe_2 system

cannot be defined by $m^* = \hbar$ [illegible] at one particular k point, but needs to be averaged over the entire bands of filled states instead [287].

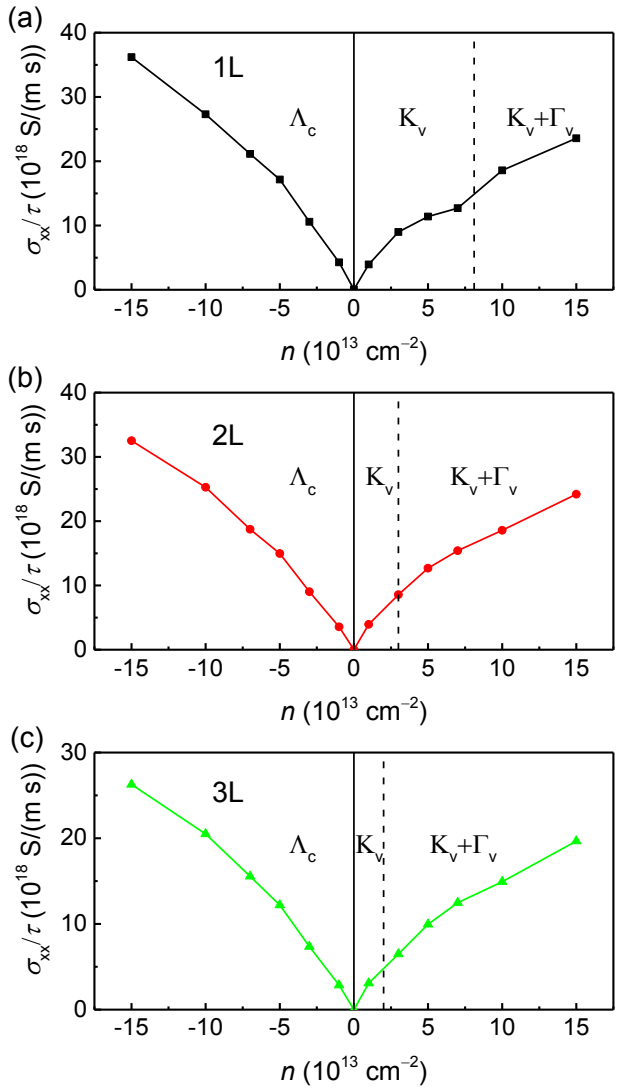

Figure 6-23. The relaxation time scaled in-plane conductivities (σ_{xx} / τ) of monolayer (1L; a), bilayer (2L; b), and trilayer (3L; c) WSe_2 at the temperature of 300 K with respect to the field-effect doping charge density n. The vertical dashed lines indicate the starting points of the doping holes occupancy at both the K and Γ valleys.

6.4 Conclusions

In this chapter, the influence of biaxial tensile strain and field-effect on the crystal structure, electronic band structure, and electrical transport property of 1~3-layer

WSe_2 has been investigated with the DFT method. The results show that 2D WSe_2 possess a relatively strong SOC effect that should not be neglected during the DFT calculation. The band energies at different k points of the Brillouin zone respond to the applied strain differently arising from the distinct atomic orbital contributions to the electronic bands at different k points. Application of biaxial tensile strain can not only result in the shrinkage of band gaps and but also relocations of the VBM and CBM of 2D WSe_2. The critical strains corresponding to the shifts of the VBM and CBM are dependent on the thickness of WSe_2. The relationship between the conductivity and tensile strain shows discrepancy for 2D WSe_2 with different types of carriers and numbers of layers. Compared to p-doped 2D WSe_2, in general, n-doped 2D WSe_2 exhibits a higher sensitivity of the conductivity to the applied tensile strain. The calculated gauge factor for n-doped 2D WSe_2 can be as high as ≈305, ≈160, and ≈105 for monolayer, bilayer, and trilayer form, respectively, which is larger than graphene and 2D MoS_2. Therefore, n-doped 2D WSe_2 is more promising for sensitive strain sensor applications.

Under the field-effect doping, although the structural parameters of WSe_2 have not undergone much change, the applied gate voltage V_{GS} can break the mirror symmetry and inversion symmetry, which modifies the spin-splitting energies of 2D WSe_2, especially for multilayer WSe_2. The field-effect doping electrons are located at the Λ valley regardless of the doping density, while the doping holes occupy the K valley under light doping but both the K and Γ valleys for heavier doping. In addition, the conductive channel thickness determined by the doping charge distribution is affected by the polarity of doping and doping density. Under a relatively strong field-effect, the conductive channel is almost narrowed to the first atomic layer (closest to the dielectric) for both n- and p-type doping. The relationship of the relaxation time scaled in-plane conductivities σ_{xx} / τ versus the field-effect doping density n exhibits distinct nonlinear behaviours depending on the type of carriers and number of WSe_2 layers.

The theoretical analysis in this chapter provides insights on the strain and field-effect modulation of 2D WSe_2, which can benefit not only further fundamental studies of WSe_2 under the effects of strain and field-effect but also future applications of 2D WSe_2 in strain sensors as well as novel field-effect devices (e.g., gate-controlled spintronics and nanogenerators).

Chapter 7 Conclusions and future work

Motivated by the promising prospect of 2D semiconducting devices, the electronic and mechanical properties of 2D WSe_2 have been studied experimentally and theoretically in this research.

Firstly, the fabrication of substrate-supported and suspended pre-patterned WSe_2 FETs have been realised for the first time with the low-cost optical lithography and vapour HF etching technology. The comparative electrical measurement of the fabricated substrate-supported and suspended WSe_2 FETs indicates that the WSe_2/dielectric interface can affect the electrical performance of 2D WSe_2 FETs negatively. Such result implies that the performance of WSe_2 FET can be improved by optimizing the quality of WSe_2/dielectric interface, such as preparing the dielectric layer with a smoother and cleaner surface and developing a residue-free transfer method of 2D WSe_2.

Further DFT theoretical studies show that the field-effect can break the mirror symmetry and inversion symmetry of 2D WSe_2, which could modify the spin-polarized carriers' population and piezoelectrical property of 2D WSe_2. In addition, the conductive channel thickness of 2D WSe_2 can be affected by both the polarity of free carriers and field-effect doping density. Under a relatively high field-effect, the conductivity of 2D WSe_2 is mainly contributed by the atomic layer closest to the dielectric. The calculated results here provide deeper understating of field-effect modulation of 2D WSe_2 for further fundamental studies and meanwhile, predict that novel gate-controlled spintronics and nanogenerators could be built from 2D WSe_2.

Moreover, this research shows that layer thinning and p-type doping of WSe_2 with the characteristics of easy scale-up, high etching selectivity, and good compatibility with CMOS fabrication technology can be realized by vapour XeF_2 exposure. By merely adjusting the XeF_2 exposure time, the thinning thickness and p-doping level of WSe_2 can be controlled easily. The thinning of WSe_2 by vapour XeF_2 features excellent smoothness of the thinned surface, which can be used for tailoring the performance of 2D WSe_2 via thickness engineering in the future. The p-doping of 2D WSe_2 with

vapour XeF_2 also benefits from good air-stability, which has been proven in the Raman, photoluminescence (PL), X-ray photoelectron spectroscopy (XPS), and electricity characterizations. This doping approach is promising for future building complex logic circuits, solar cells, and LEDs with 2D WSe_2.

For the studies of the mechanical property of 2D WSe_2, the in-plane elastic property of 2D WSe_2 has been first time experimentally characterized using nanoindentation method under an atomic force microscopy (AFM). The Young's modulus E_Y of the measured 2D WSe_2 (167.3±6.7 GPa) with the thickness of 5-, 6-, 12-, and 14-layer is statistically independent of the thickness of WSe_2, whose value is about one-sixth of graphene and two-thirds of other most investigated 2D TMDs, namely, MoS_2 and WS_2. Also, the 2D WSe_2 can withstand ≈7.3% strain without breaking or mechanical degradation. The above features make 2D WSe_2 more suitable for applications in flexible devices and nanoelectromechanical systems (NEMS) working in low resonant frequency such as acoustic sensors and loudspeakers, compared to the graphene, MoS_2, and WS_2.

DFT theoretical studies have shown that application of biaxial tensile strain can not only result in the shrinkage of the band gaps and but also relocations of the VBM and CBM of 2D WSe_2. The critical strains corresponding to the shifts of the VBM and CBM are dependent on the thickness of WSe_2. Furthermore, the evolution of the conductivity under tensile strain shows discrepant behaviours for WSe_2 with different types of carriers and numbers of layers. Compared to graphene and 2D MoS_2, n-doped 2D WSe_2 is predicted to possess a higher gauge factor (as high as ≈305, ≈160, and ≈105 for monolayer, bilayer, and trilayer form, respectively) making it more promising for sensitive strain sensor applications.

In terms of the future work, more systematic studies need to be carried out in the future to gain a deeper understanding of the mechanism of the observed WSe_2/SiO_2 interface effects, including characterizing the electrical performance of the suspended WSe_2 in different humidity and temperature environment. In addition, piezoresistive properties of 2D WSe_2 should be investigated experimentally to provide more knowledge for 2D WSe_2 strain sensor applications. Figure 7-1 proposes the setup for the measurement, in which a suspended WSe_2 FET device is indented by an AFM probe. The indentation

of the AFM probe will apply specific strains to the suspended WSe_2 channel, and meanwhile, the conductivity of the strained WSe_2 can be obtained by measuring the drain-source current I_{DS} when a drain-source bias voltage V_{DS} is applied. Furthermore, the resonant behaviour (resonant frequency and amplitude under different actuation parameters) of 2D WSe_2 should be investigated to explore the possibility of 2D WSe_2 applications in the acoustic sensors and loudspeakers.

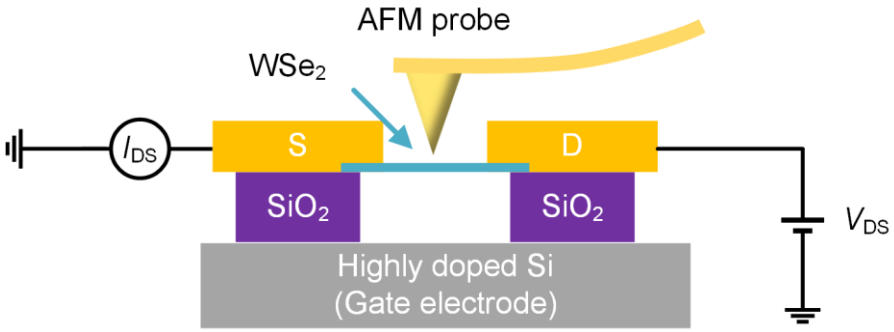

Figure 7-1. The schematic setup for measuring the piezoresistivity of 2D WSe_2.

Appendix A Raman spectra of WO_x

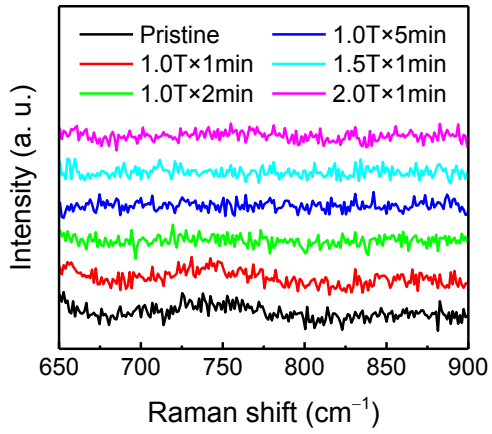

Figure A-1. Raman spectra of pristine WSe_2 and XeF_2 treated WSe_2 under various conditions in the range of 650–900 cm^{-1}. The spectra are offset vertically for clarity.

Appendix B XeF_2 doping concentration and Fermi level calculation of WSe_2

Considering an electronic system with parabolic dispersion, for a nondegenerate p-type doping ($E_F - E_V > 3kT$), the hole concentration can be extracted with the equation $n_h = N_V \exp\frac{E_V - E_F}{kT}$, where $N_V = 2\left(\frac{2\pi m_h^* kT}{h^2}\right)^{3/2}$ is the effective density of states of the valence band, m_h^* is the hole's effective mass, i.e., $0.45m_0$ for WSe_2 [288, 289], and m_0 is the electron rest mass. N_V is calculated to be 7.50×10^{18} cm^{-3} at $T = 298$K. Similarly, for nondegenerate n-type doping ($E_C - E_F > 3kT$), the electron concentration follows: $n_e = N_C \exp\frac{E_F - E_C}{kT}$, where $N_C = 2\left(\frac{2\pi m_e^* kT}{h^2}\right)^{3/2}$ is the effective density of states of the conduction band and m_e^* is the electron's effective mass of $0.34m_0$ [289, 290]. N_C is calculated to be 4.92×10^{18} cm^{-3} at $T = 298$K. Therefore, the carrier concentration at the boundary of nondegenerate and degenerate doping for p-type ($E_F - E_V = 3kT$) and n-type ($E_C - E_F = 3kT$) is estimated to be 3.73×10^{17} cm^{-3} and 2.45×10^{17} cm^{-3}, respectively.

As shown in Figure 4-16a, when $V_{GS} = 0$V, electrons are the dominant charge carriers for pristine WSe_2 FET while for XeF_2 thinned WSe_2 FET, holes are the majority carriers. The volume carrier concentrations at $V_{GS} = 0$ V, derived from the equation $n = I_{DS}L/qWd\mu V_{DS}$, are 2.11×10^{17} cm^{-3} (n_e) and 27.86×10^{17} cm^{-3} (n_h) for pristine and XeF_2 thinned WSe_2, respectively. Note that the XeF_2 treatment results in degenerate doping of WSe_2 on account of one order of magnitude higher hole concentration than the maximum carrier concentration of nondegenerate p-doping. For pristine WSe_2, the Fermi level can be estimated using the nondegenerate n-doping relation mentioned before, and $E_C - E_F$ is calculated to be ≈81 meV. For degenerately p-doped WSe_2 by vapour XeF_2, the Fermi level can be obtained by the Joyce and Dixon approximation [291]:

$\frac{E_V - E_F}{kT} \approx \ln\left(\frac{n_h}{N_V}\right) + \frac{1}{\sqrt{8}}\frac{n_h}{N_V}$, giving $E_F - E_V \approx 22$ meV.

Appendix C Publications

Chapter of book

[1] **R. Zhang**, R. Cheung, Mechanical Properties and Applications of Two-Dimensional Materials, in: P.K. Nayak (Ed.), *Two-dimensional Materials - Synthesis, Characterization and Potential Applications*, InTech, Rijeka, Croatia, 2016, pp. 219-246.

Journal articles

[1] **R. Zhang**, D. Drysdale, V. Koutsos, R. Cheung, Controlled Layer Thinning and p-Type Doping of WSe_2 by Vapor XeF_2, *Advanced Functional Materials* (2017) 1702455.

[2] **R. Zhang**, V. Koutsos, R. Cheung, Elastic properties of suspended multilayer WSe_2, *Applied Physics Letters* 108(4) (2016) 042104.

[3] **R. Zhang**, T. Chen, A. Bunting, R. Cheung, Optical lithography technique for the fabrication of devices from mechanically exfoliated two-dimensional materials, *Microelectronic Engineering* 154 (2016) 62-68.

[4] B. Sviličić, E. Mastropaolo, **R. Zhang**, R. Cheung, Tunable MEMS cantilever resonators electrothermally actuated and piezoelectrically sensed, *Microelectronic Engineering* 145(0) (2015) 38-42.

References

[1] Novoselov KS, Geim AK, Morozov SV, et al. Electric field effect in atomically thin carbon films. Science 2004;306:666-9.

[2] Song L, Ci L, Lu H, et al. Large Scale Growth and Characterization of Atomic Hexagonal Boron Nitride Layers. Nano Lett 2010;10:3209-15.

[3] Lee C, Wei X, Kysar JW, et al. Measurement of the elastic properties and intrinsic strength of monolayer graphene. Science 2008;321:385-8.

[4] Gomez-Navarro C, Burghard M, Kern K. Elastic properties of chemically derived single graphene sheets. Nano Lett 2008;8:2045-9.

[5] Song XF, Oksanen M, Sillanpaa MA, et al. Stamp Transferred Suspended Graphene Mechanical Resonators for Radio Frequency Electrical Readout. Nano Lett 2012;12:198-202.

[6] Castellanos-Gomez A, Poot M, Steele GA, et al. Elastic Properties of Freely Suspended MoS_2 Nanosheets. Adv Mater 2012;24:772-5.

[7] Bertolazzi S, Brivio J, Kis A. Stretching and breaking of ultrathin MoS_2. Acs Nano 2011;5:9703-9.

[8] Zhao X, Zhang Q, Chen D, et al. Enhanced Mechanical Properties of Graphene-Based Poly(vinyl alcohol) Composites. Macromolecules 2010;43:2357-63.

[9] Zhang Y, Tan Y-W, Stormer HL, et al. Experimental observation of the quantum Hall effect and Berry's phase in graphene. Nature 2005;438:201-4.

[10] Zhao W, Ghorannevis Z, Chu L, et al. Evolution of Electronic Structure in Atomically Thin Sheets of WS_2 and WSe_2. Acs Nano 2013;7:791-7.

[11] Wang QH, Kalantar-Zadeh K, Kis A, et al. Electronics and optoelectronics of two-dimensional transition metal dichalcogenides. Nat Nanotechnol 2012;7:699-712.

[12] Yoon J, Park W, Bae G-Y, et al. Highly Flexible and Transparent Multilayer MoS_2 Transistors with Graphene Electrodes. Small 2013;9:3295-300.

[13] Wang H, Yu LL, Lee YH, et al. Integrated Circuits Based on Bilayer MoS2 Transistors. Nano Lett 2012;12:4674-80.

[14] Bertolazzi S, Krasnozhon D, Kis A. Nonvolatile Memory Cells Based on MoS_2/Graphene Heterostructures. Acs Nano 2013;7:3246-52.

[15] Lopez-Sanchez O, Lembke D, Kayci M, et al. Ultrasensitive photodetectors based on monolayer MoS_2. Nat Nanotechnol 2013;8:497-501.

[16] Schwierz F. Graphene transistors. Nat Nanotechnol 2010;5:487-96.

[17] Radisavljevic B, Radenovic A, Brivio J, et al. Single-layer MoS_2 transistors. Nat Nanotechnol 2011;6:147-50.

[18] Ieong M, Doris B, Kedzierski J, et al. Silicon Device Scaling to the Sub-10-nm Regime. Science 2004;306:2057-60.

[19] Desai SB, Madhvapathy SR, Sachid AB, et al. MoS2 transistors with 1-nanometer gate lengths. Science 2016;354:99-102.

[20] Park M, Park YJ, Chen X, et al. MoS2-Based Tactile Sensor for Electronic Skin Applications. Adv Mater 2016;28:2556-62.

[21] Chen L, Xue F, Li X, et al. Strain-Gated Field Effect Transistor of a MoS2-ZnO 2D-1D Hybrid Structure. Acs Nano 2016;10:1546-51.

[22] Chen Y, Ke F, Ci P, et al. Pressurizing Field-Effect Transistors of Few-Layer MoS2 in a Diamond Anvil Cell. Nano Lett 2017;17:194-9.

[23] Lee K, Gatensby R, McEvoy N, et al. High-Performance Sensors Based on Molybdenum Disulfide Thin Films. Adv Mater 2013;25:6699-702.

[24] Late DJ, Huang Y-K, Liu B, et al. Sensing Behavior of Atomically Thin-Layered MoS2 Transistors. Acs Nano 2013;7:4879-91.

[25] Li H, Yin Z, He Q, et al. Fabrication of Single- and Multilayer MoS2 Film-Based Field-Effect Transistors for Sensing NO at Room Temperature. Small 2012;8:63-7.

[26] Shimazu Y, Tashiro M, Sonobe S, et al. Environmental Effects on Hysteresis of Transfer Characteristics in Molybdenum Disulfide Field-Effect Transistors. Sci Rep 2016;6:30084.

[27] Sarkar D, Liu W, Xie X, et al. MoS2 Field-Effect Transistor for Next-Generation Label-Free Biosensors. Acs Nano 2014;8:3992-4003.

[28] Zhu C, Zeng Z, Li H, et al. Single-Layer MoS2-Based Nanoprobes for Homogeneous Detection of Biomolecules. J Am Chem Soc 2013;135:5998-6001.

[29] Sun Q, Seung W, Kim BJ, et al. Active Matrix Electronic Skin Strain Sensor Based on Piezopotential-Powered Graphene Transistors. Adv Mater 2015;27:3411-7.

[30] Wu W, Wang L, Li Y, et al. Piezoelectricity of single-atomic-layer MoS_2 for energy conversion and piezotronics. Nature 2014;514:470-4.

[31] Splendiani A, Sun L, Zhang Y, et al. Emerging Photoluminescence in Monolayer MoS_2. Nano Lett 2010;10:1271-5.

[32] Yun WS, Han SW, Hong SC, et al. Thickness and strain effects on electronic structures of transition metal dichalcogenides: 2H-MX2semiconductors (M=Mo, W;X=S, Se, Te). Phys Rev B 2012;85.

[33] Ross JS, Klement P, Jones AM, et al. Electrically tunable excitonic light-emitting diodes based on monolayer WSe2 p-n junctions. Nat Nanotechnol 2014;9:268-72.

[34] Wi S, Chen M, Li D, et al. Photovoltaic response in pristine WSe2 layers modulated by metal-induced surface-charge-transfer doping. Appl Phys Lett 2015;107:062102.

[35] Lee J-U, Yoon D, Cheong H. Estimation of Young's Modulus of Graphene by Raman Spectroscopy. Nano Lett 2012;12:4444-8.

[36] Koenig SP, Boddeti NG, Dunn ML, et al. Ultrastrong adhesion of graphene membranes. Nat Nanotechnol 2011;6:543-6.

[37] Liu K, Yan QM, Chen M, et al. Elastic Properties of Chemical-Vapor-Deposited Monolayer MoS_2, WS_2, and Their Bilayer Heterostructures. Nano Lett 2014;14:5097-103.

[38] Wang J-Y, Li Y, Zhan Z-Y, et al. Elastic properties of suspended black phosphorus nanosheets. Appl Phys Lett 2016;108:013104.

[39] Tao J, Shen W, Wu S, et al. Mechanical and Electrical Anisotropy of Few-Layer Black Phosphorus. Acs Nano 2015;9:11362-70.

[40] Wong CL, Annamalai M, Wang ZQ, et al. Characterization of nanomechanical graphene drum structures. J Micromech Microeng 2010;20:115029.

[41] Bunch JS, Verbridge SS, Alden JS, et al. Impermeable Atomic Membranes from Graphene Sheets. Nano Lett 2008;8:2458-62.

[42] Li P, You Z, Haugstad G, et al. Graphene fixed-end beam arrays based on mechanical exfoliation. Appl Phys Lett 2011;98:253105.

[43] Lopez-Polin G, Gomez-Navarro C, Parente V, et al. Increasing the elastic modulus of graphene by controlled defect creation. Nat Phys 2015;11:26-31.

[44] Ruiz-Vargas CS, Zhuang HL, Huang PY, et al. Softened Elastic Response and Unzipping in Chemical Vapor Deposition Graphene Membranes. Nano Lett 2011;11:2259-63.

[45] Lee G-H, Cooper RC, An SJ, et al. High-Strength Chemical-Vapor–Deposited Graphene and Grain Boundaries. Science 2013;340:1073-6.

[46] Lin Q-Y, Jing G, Zhou Y-B, et al. Stretch-Induced Stiffness Enhancement of Graphene Grown by Chemical Vapor Deposition. Acs Nano 2013;7:1171-7.

[47] Suk JW, Piner RD, An J, et al. Mechanical Properties of Monolayer Graphene Oxide. Acs Nano 2010;4:6557-64.

[48] Castellanos-Gomez A, Poot M, Amor-Amoros A, et al. Mechanical properties of freely suspended atomically thin dielectric layers of mica. Nano Res 2012;5:550-7.

[49] Kim D-H, Ahn J-H, Choi WM, et al. Stretchable and Foldable Silicon Integrated Circuits. Science 2008;320:507-11.

[50] Conley HJ, Wang B, Ziegler JI, et al. Bandgap Engineering of Strained Monolayer and Bilayer MoS2. Nano Lett 2013;13:3626-30.

[51] Desai SB, Seol G, Kang JS, et al. Strain-Induced Indirect to Direct Bandgap Transition in Multi layer WSe2. Nano Lett 2014;14:4592-7.

[52] He K, Poole C, Mak KF, et al. Experimental Demonstration of Continuous Electronic Structure Tuning via Strain in Atomically Thin MoS2. Nano Lett 2013;13:2931-6.

[53] Zhu CR, Wang G, Liu BL, et al. Strain tuning of optical emission energy and polarization in monolayer and bilayer MoS2. Phys Rev B 2013;88.

[54] Castellanos-Gomez A, Roldan R, Cappelluti E, et al. Local Strain Engineering in Atomically Thin MoS2. Nano Lett 2013;13:5361-6.

[55] Hui YY, Liu X, Jie W, et al. Exceptional Tunability of Band Energy in a Compressively Strained Trilayer MoS2 Sheet. Acs Nano 2013;7:7126-31.

[56] Wang Y, Cong C, Yang W, et al. Strain-induced direct–indirect bandgap transition and phonon modulation in monolayer WS_2. Nano Res 2015;8:2562-72.

[57] Yang S, Wang C, Sahin H, et al. Tuning the Optical, Magnetic, and Electrical Properties of ReSe2 by Nanoscale Strain Engineering. Nano Lett 2015;15:1660-6.

[58] Island JO, Kuc A, Diependaal EH, et al. Precise and reversible band gap tuning in single-layer MoSe2 by uniaxial strain. Nanoscale 2016;8:2589-93.

[59] Lee G-H, Cui X, Kim YD, et al. Highly Stable, Dual-Gated MoS_2 Transistors Encapsulated by Hexagonal Boron Nitride with Gate-Controllable Contact, Resistance, and Threshold Voltage. Acs Nano 2015;9:7019-26.

[60] Roy T, Tosun M, Kang JS, et al. Field-Effect Transistors Built from All Two-Dimensional Material Components. Acs Nano 2014;8:6259-64.

[61] Das S, Gulotty R, Sumant AV, et al. All Two-Dimensional, Flexible, Transparent, and Thinnest Thin Film Transistor. Nano Lett 2014;14:2861-6.

[62] Dou X, Ding K, Jiang D, et al. Tuning and Identification of Interband Transitions in Monolayer and Bilayer Molybdenum Disulfide Using Hydrostatic Pressure. Acs Nano 2014;8:7458-64.

[63] Fu X-W, Liao Z-M, Zhou J-X, et al. Strain dependent resistance in chemical vapor deposition grown graphene. Appl Phys Lett 2011;99:213107.

[64] Bae S-H, Lee Y, Sharma BK, et al. Graphene-based transparent strain sensor. Carbon 2013;51:236-42.

[65] Zhu S-E, Ghatkesar MK, Zhang C, et al. Graphene based piezoresistive pressure sensor. Appl Phys Lett 2013;102:161904.

[66] Huang M, Pascal TA, Kim H, et al. Electronic-Mechanical Coupling in Graphene from in situ Nanoindentation Experiments and Multiscale Atomistic Simulations. Nano Lett 2011;11:1241-6.

[67] He X, Gao L, Tang N, et al. Shear strain induced modulation to the transport properties of graphene. Appl Phys Lett 2014;105:083108.

[68] Smith AD, Niklaus F, Paussa A, et al. Electromechanical Piezoresistive Sensing in Suspended Graphene Membranes. Nano Lett 2013;13:3237-42.

[69] Choi MK, Park I, Kim DC, et al. Thermally Controlled, Patterned Graphene Transfer Printing for Transparent and Wearable Electronic/Optoelectronic System. Adv Funct Mater 2015;25:7109-18.

[70] Manzeli S, Allain A, Ghadimi A, et al. Piezoresistivity and Strain-induced Band Gap Tuning in Atomically Thin MoS_2. Nano Lett 2015;15:5330-5.

[71] Zhao J, Wang G, Yang R, et al. Tunable Piezoresistivity of Nanographene Films for Strain Sensing. Acs Nano 2015;9:1622-9.

[72] Zhao J, He C, Yang R, et al. Ultra-sensitive strain sensors based on piezoresistive nanographene films. Appl Phys Lett 2012;101:063112.

[73] Wang Y, Wang L, Yang T, et al. Wearable and Highly Sensitive Graphene Strain Sensors for Human Motion Monitoring. Adv Funct Mater 2014;24:4666-70.

[74] Yang T, Wang Y, Li X, et al. Torsion sensors of high sensitivity and wide dynamic range based on a graphene woven structure. Nanoscale 2014;6:13053-9.

[75] Zhu H, Wang Y, Xiao J, et al. Observation of piezoelectricity in free-standing monolayer MoS_2. Nat Nanotechnol 2015;10:151-5.

[76] Chen CY, Rosenblatt S, Bolotin KI, et al. Performance of monolayer graphene nanomechanical resonators with electrical readout. Nat Nanotechnol 2009;4:861-7.

[77] Ekinci KL, Roukes ML. Nanoelectromechanical systems. Rev Sci Instrum 2005;76:061101.

[78] Chen C, Hone J. Graphene nanoelectromechanical systems. P Ieee 2013;101:1766-79.

[79] Eichler A, Moser J, Chaste J, et al. Nonlinear damping in mechanical resonators made from carbon nanotubes and graphene. Nat Nanotechnol 2011;6:339-42.

[80] Chen T, Mastropaolo E, Bunting A, et al. Observation of second flexural mode enhancement in graphene resonators. Electron Lett 2015;51:1014-6.

[81] Grady E, Mastropaolo E, Chen T, et al. Low frequency graphene resonators for acoustic sensing. Microelectron Eng 2014;119:105-8.

[82] Suk JW, Kirk K, Hao Y, et al. Thermoacoustic Sound Generation from Monolayer Graphene for Transparent and Flexible Sound Sources. Adv Mater 2012;24:6342-7.

[83] Benameur MM, Radisavljevic B, Heron JS, et al. Visibility of dichalcogenide nanolayers. Nanotechnology 2011;22:125706.

[84] Blake P, Hill EW, Castro Neto AH, et al. Making graphene visible. Appl Phys Lett 2007;91:063124.

[85] Meitl MA, Zhu ZT, Kumar V, et al. Transfer printing by kinetic control of adhesion to an elastomeric stamp. Nat Mater 2006;5:33-8.

[86] Liang X, Fu Z, Chou SY. Graphene Transistors Fabricated via Transfer-Printing In Device Active-Areas on Large Wafer. Nano Lett 2007;7:3840-4.

[87] Gardiner DJ, Introduction to Raman Scattering, in: D.J. Gardiner, P.R. Graves (Eds.) Practical Raman Spectroscopy, Springer Berlin Heidelberg, Berlin, Heidelberg, 1989, pp. 1-12.

[88] Li SL, Miyazaki H, Song H, et al. Quantitative Raman Spectrum and Reliable Thickness Identification for Atomic Layers on Insulating Substrates. Acs Nano 2012;6:7381-8.

[89] Li H, Zhang Q, Yap CCR, et al. From Bulk to Monolayer MoS_2: Evolution of Raman Scattering. Adv Funct Mater 2012;22:1385-90.

[90] Lee C, Yan H, Brus LE, et al. Anomalous Lattice Vibrations of Single- and Few-Layer MoS_2. Acs Nano 2010;4:2695-700.

[91] Chakraborty B, Bera A, Muthu DVS, et al. Symmetry-dependent phonon renormalization in monolayer MoS2 transistor. Phys Rev B 2012;85:161403.

[92] Oh HM, Jeong H, Han GH, et al. Modulating Electronic Properties of Monolayer MoS2 via Electron-Withdrawing Functional Groups of Graphene Oxide. Acs Nano 2016;10:10446-53.

[93] Zhou H, Yu F, Liu Y, et al. Thickness-dependent patterning of MoS2 sheets with well-oriented triangular pits by heating in air. Nano Res 2013;6:703-11.

[94] Yamamoto M, Einstein TL, Fuhrer MS, et al. Anisotropic Etching of Atomically Thin MoS2. J Phys Chem C 2013;117:25643-9.

[95] Kang D-H, Shim J, Jang SK, et al. Controllable Nondegenerate p-Type Doping of Tungsten Diselenide by Octadecyltrichlorosilane. Acs Nano 2015;9:1099-107.

[96] Bertolazzi S, Bonacchi S, Nan GJ, et al. Engineering Chemically Active Defects in Monolayer MoS2 Transistors via Ion-Beam Irradiation and Their Healing via Vapor Deposition of Alkanethiols. Adv Mater 2017;29.

[97] Late DJ, Shirodkar SN, Waghmare UV, et al. Thermal Expansion, Anharmonicity and Temperature-Dependent Raman Spectra of Single- and Few-Layer MoSe2 and WSe2. Chemphyschem 2014;15:1592-8.

[98] Yan R, Simpson JR, Bertolazzi S, et al. Thermal Conductivity of Monolayer Molybdenum Disulfide Obtained from Temperature-Dependent Raman Spectroscopy. Acs Nano 2013;8:986-93.

[99] Yamamoto M, Dutta S, Aikawa S, et al. Self-Limiting Layer-by-Layer Oxidation of Atomically Thin WSe2. Nano Lett 2015;15:2067-73.

[100] Chen K, Kiriya D, Hettick M, et al. Air stable n-doping of WSe2 by silicon nitride thin films with tunable fixed charge density. Apl Materials 2014;2.

[101] Tosun M, Chan L, Amani M, et al. Air-Stable n-Doping of WSe2 by Anion Vacancy Formation with Mild Plasma Treatment. Acs Nano 2016;10:6853-60.

[102] Wu ZT, Luo ZZ, Shen YT, et al. Defects as a factor limiting carrier mobility in WSe2: A spectroscopic investigation. Nano Res 2016;9:3622-31.

[103] Li H, Lu G, Wang Y, et al. Mechanical Exfoliation and Characterization of Single- and Few-Layer Nanosheets of WSe_2, TaS_2, and $TaSe_2$. Small 2013;9:1974-81.

[104] Sahin H, Tongay S, Horzum S, et al. Anomalous Raman spectra and thickness-dependent electronic properties of WSe2. Phys Rev B 2013;87:165409.

[105] 2018, Way2Science-Raman spectroscopy, http://way2science.com/raman-spectroscopy-2/

[106] Petherbridge JR. Diagnostics of microwave activated novel gas mixtures for diamond chemical vapour deposition. 2002.

[107] Huang JK, Pu J, Hsu CL, et al. Large-Area Synthesis of Highly Crystalline WSe_2 Mono layers and Device Applications. Acs Nano 2014;8:923-30.

[108] Powell CJP, Jablonski A, NIST Electron Inelastic-Mean-Free-Path Database - Version 1.2, National Institute of Standards and Technology, Gaithersburg, MD, USA, 2010.

[109] Zeng G, Duan Y, Besenbacher F, et al., Nanomechanics of Amyloid Materials Studied by Atomic Force Microscopy, Atomic Force Microscopy Investigations into Biology-From Cell to Protein, InTech, 2012.

[110] Nemes-Incze P, Osváth Z, Kamarás K, et al. Anomalies in thickness measurements of graphene and few layer graphite crystals by tapping mode atomic force microscopy. Carbon 2008;46:1435-42.

[111] Ohler B. Practical advice on the determination of cantilever spring constants. Bruker Application Note# AN94 2007;1.

[112] Parr RG. Density functional theory. Annu Rev Phys Chem 1983;34:631-56.

[113] Hohenberg P, Kohn W. Inhomogeneous electron gas. Physical review 1964;136:B864.

[114] Kohn W. W. Kohn and LJ Sham, Phys. Rev. 140, A1133 (1965). Phys. Rev. 1965;140:A1133.

[115] Giannozzi P, Andreussi O, Brumme T, et al. Advanced capabilities for materials modelling with Quantum ESPRESSO. Journal of Physics: Condensed Matter 2017;29:465901.

[116] Paolo G, Stefano B, Nicola B, et al. QUANTUM ESPRESSO: a modular and open-source software project for quantum simulations of materials. Journal of Physics: Condensed Matter 2009;21:395502.

[117] Garrity KF, Bennett JW, Rabe KM, et al. Pseudopotentials for high-throughput DFT calculations. Comp Mater Sci 2014;81:446-52.

[118] Dal Corso A. Pseudopotentials periodic table: From H to Pu. Comp Mater Sci 2014;95:337-50.

[119] Perdew JP, Burke K, Ernzerhof M. Generalized Gradient Approximation Made Simple. Phys Rev Lett 1996;77:3865-8.

[120] Grimme S, Antony J, Ehrlich S, et al. A consistent and accurate ab initio parametrization of density functional dispersion correction (DFT-D) for the 94 elements H-Pu. The Journal of Chemical Physics 2010;132:154104.

[121] Monkhorst HJ, Pack JD. Special points for Brillouin-zone integrations. Phys Rev B 1976;13:5188-92.

[122] Schutte WJ, De Boer JL, Jellinek F. Crystal structures of tungsten disulfide and diselenide. J Solid State Chem 1987;70:207-9.

[123] Tonndorf P, Schmidt R, Boettger P, et al. Photoluminescence emission and Raman response of monolayer MoS2, MoSe2, and WSe2. Opt Express 2013;21:4908-16.

[124] Novoselov KS, Geim AK, Morozov S, et al. Electric field effect in atomically thin carbon films. Science 2004;306:666-9.

[125] Coleman JN, Lotya M, O'Neill A, et al. Two-Dimensional Nanosheets Produced by Liquid Exfoliation of Layered Materials. Science 2011;331:568-71.

[126] Lee Y-H, Zhang X-Q, Zhang W, et al. Synthesis of Large-Area MoS_2 Atomic Layers with Chemical Vapor Deposition. Adv Mater 2012;24:2320-5.

[127] Lee Y, Bae S, Jang H, et al. Wafer-Scale Synthesis and Transfer of Graphene Films. Nano Lett 2010;10:490-3.

[128] Lin YC, Zhang W, Huang JK, et al. Wafer-scale MoS_2 thin layers prepared by MoO_3 sulfurization. Nanoscale 2012;4:6637-41.

[129] Tarasov A, Campbell PM, Tsai MY, et al. Highly Uniform Trilayer Molybdenum Disulfide for Wafer-Scale Device Fabrication. Adv Funct Mater 2014;24:6389-400.

[130] Teweldebrhan D, Balandin AA. Modification of graphene properties due to electron-beam irradiation. Appl Phys Lett 2009;94:013101.

[131] Zan R, Ramasse QM, Jalil R, et al. Control of Radiation Damage in MoS_2 by Graphene Encapsulation. Acs Nano 2013;7:10167-74.

[132] Garcia A, Raya AM, Mariscal MM, et al. Analysis of electron beam damage of exfoliated MoS_2 sheets and quantitative HAADF-STEM imaging. Ultramicroscopy 2014;146:33-8.

[133] Childres I, Jauregui LA, Foxe M, et al. Effect of electron-beam irradiation on graphene field effect devices. Appl Phys Lett 2010;97:173109.

[134] Durand C, Zhang X, Fowlkes J, et al. Defect-mediated transport and electronic irradiation effect in individual domains of CVD-grown monolayer MoS_2. J Vac Sci Technol B 2015;33:02B110.

[135] Bolotin KI, Sikes KJ, Jiang Z, et al. Ultrahigh electron mobility in suspended graphene. Solid State Commun 2008;146:351-5.

[136] Jin T, Kang J, Su Kim E, et al. Suspended single-layer MoS_2 devices. J Appl Phys 2013;114:164509.

[137] Velasco J, Jr., Zhao Z, Zhang H, et al. Suspension and measurement of graphene and Bi_2Se_3 thin crystals. Nanotechnology 2011;22:285305.

[138] Li H, Wu J, Huang X, et al. Rapid and Reliable Thickness Identification of Two-Dimensional Nanosheets Using Optical Microscopy. Acs Nano 2013;7:10344-53.

[139] Li H, Lu G, Yin Z, et al. Optical Identification of Single- and Few-Layer MoS_2 Sheets. Small 2012;8:682-6.

[140] Liu W, Kang J, Sarkar D, et al. Role of Metal Contacts in Designing High-Performance Monolayer n-Type WSe_2 Field Effect Transistors. Nano Lett 2013;13:1983-90.

[141] Das S, Chen HY, Penumatcha AV, et al. High Performance Multilayer MoS_2 Transistors with Scandium Contacts. Nano Lett 2013;13:100-5.

[142] McDonnell S, Azcatl A, Addou R, et al. Hole Contacts on Transition Metal Dichalcogenides: Interface Chemistry and Band Alignments. Acs Nano 2014;8:6265-72.

[143] Kang J, Liu W, Sarkar D, et al. Computational Study of Metal Contacts to Monolayer Transition-Metal Dichalcogenide Semiconductors. Physical Review X 2014;4:031005.

[144] Wan X, Chen K, Xie WG, et al. Quantitative Analysis of Scattering Mechanisms in Highly Crystalline CVD MoS2 through a Self-Limited Growth Strategy by Interface Engineering. Small 2016;12:438-45.

[145] Joo MK, Moon BH, Ji H, et al. Electron Excess Doping and Effective Schottky Barrier Reduction on the MoS2/h-BN Hetero-structure. Nano Lett 2016;16:6383-9.

[146] Peimyoo N, Shang J, Yang W, et al. Thermal conductivity determination of suspended mono- and bilayer WS2 by Raman spectroscopy. Nano Res 2015;8:1210-21.

[147] Guo Y, Wei XL, Shu JP, et al. Charge trapping at the MoS_2-SiO_2 interface and its effects on the characteristics of MoS_2 metal-oxide-semiconductor field effect transistors. Appl Phys Lett 2015;106.

[148] Cui X, Lee GH, Kim YD, et al. Multi-terminal transport measurements of MoS2 using a van der Waals heterostructure device platform. Nat Nanotechnol 2015;10:534-40.

[149] Radisavljevic B, Kis A. Mobility engineering and a metal-insulator transition in monolayer MoS_2. Nat Mater 2013;12:815-20.

[150] Joo MK, Moon BH, Ji HJ, et al. Understanding Coulomb Scattering Mechanism in Monolayer MoS2 Channel in the Presence of h-BN Buffer Layer. ACS Appl Mater Interfaces 2017;9:5006-13.

[151] Ji H, Joo MK, Yi H, et al. Tunable Mobility in Double-Gated MoTe2 Field-Effect Transistor: Effect of Coulomb Screening and Trap Sites. ACS Appl Mater Interfaces 2017;9:29185-92.

[152] McDonnell S, Addou R, Buie C, et al. Defect-Dominated Doping and Contact Resistance in MoS2. Acs Nano 2014;8:2880-8.

[153] Yu L, Zubair A, Santos EJG, et al. High-Performance WSe2 Complementary Metal Oxide Semiconductor Technology and Integrated Circuits. Nano Lett 2015;15:4928-34.

[154] Movva HCP, Rai A, Kang S, et al. High-Mobility Holes in Dual-Gated WSe2 Field-Effect Transistors. Acs Nano 2015;9:10402-10.

[155] Fang H, Chuang S, Chang TC, et al. High-Performance Single Layered WSe_2 p-FETs with Chemically Doped Contacts. Nano Lett 2012;12:3788-92.

[156] Allain A, Kis A. Electron and Hole Mobilities in Single-Layer WSe2. Acs Nano 2014;8:7180-5.

[157] Late DJ, Liu B, Matte HSSR, et al. Hysteresis in Single-Layer MoS_2 Field Effect Transistors. Acs Nano 2012;6:5635-41.

[158] Ishigami M, Chen JH, Cullen WG, et al. Atomic Structure of Graphene on SiO_2. Nano Lett 2007;7:1643-8.

[159] Nagashio K, Yamashita T, Nishimura T, et al. Electrical transport properties of graphene on SiO2 with specific surface structures. J Appl Phys 2011;110:024513.

[160] Li SL, Wakabayashi K, Xu Y, et al. Thickness-Dependent Interfacial Coulomb Scattering in Atomically Thin Field-Effect Transistors. Nano Lett 2013;13:3546-52.

[161] Li T, Du G, Zhang B, et al. Scaling behavior of hysteresis in multilayer MoS_2 field effect transistors. Appl Phys Lett 2014;105:093107.

[162] Zhou C, Zhao Y, Raju S, et al. Carrier Type Control of WSe2 Field-Effect Transistors by Thickness Modulation and MoO3 Layer Doping. Adv Funct Mater 2016;26:4223-30.

[163] Kim HC, Kim H, Lee JU, et al. Engineering Optical and Electronic Properties of WS2 by Varying the Number of Layers. Acs Nano 2015;9:6854-60.

[164] Wang YX, Xu N, Li DY, et al. Thermal Properties of Two Dimensional Layered Materials. Adv Funct Mater 2017;27:1604134.

[165] Zhang YW, Li H, Wang HM, et al. Thickness Considerations of Two-Dimensional Layered Semiconductors for Transistor Applications. Sci Rep 2016;6:29615.

[166] Prakash A, Appenzeller J. Bandgap Extraction and Device Analysis of Ionic Liquid Gated WSe2 Schottky Barrier Transistors. Acs Nano 2017;11:1626-32.

[167] Yu ZH, Ong ZY, Li SL, et al. Analyzing the Carrier Mobility in Transition-Metal Dichalcogenide MoS2 Field-Effect Transistors. Adv Funct Mater 2017;27:1604093.

[168] Mak KF, Lee C, Hone J, et al. Atomically Thin MoS_2: A New Direct-Gap Semiconductor. Phys Rev Lett 2010;105:136805.

[169] Li XL, Han WP, Wu JB, et al. Layer-Number Dependent Optical Properties of 2D Materials and Their Application for Thickness Determination. Adv Funct Mater 2017;27:1604468.

[170] Bae JJ, Jeong HY, Han GH, et al. Thickness-dependent in-plane thermal conductivity of suspended MoS2 grown by chemical vapor deposition. Nanoscale 2017;9:2541-7.

[171] Zhang R, Cheung R, Mechanical Properties and Applications of Two-Dimensional Materials, in: P.K. Nayak (Ed.) Two-dimensional Materials - Synthesis, Characterization and Potential Applications, InTech, Rijeka, Croatia, 2016, pp. 219-46.

[172] Castellanos-Gomez A, Barkelid M, Goossens AM, et al. Laser-Thinning of MoS2: On Demand Generation of a Single-Layer Semiconductor. Nano Lett 2012;12:3187-92.

[173] Wang D, Wang YQ, Chen XD, et al. Layer-by-layer thinning of two-dimensional MoS2 films by using a focused ion beam. Nanoscale 2016;8:4107-12.

[174] Wu J, Li H, Yin Z, et al. Layer Thinning and Etching of Mechanically Exfoliated MoS2 Nanosheets by Thermal Annealing in Air. Small 2013;9:3314-9.

[175] Lu X, Utama MIB, Zhang J, et al. Layer-by-layer thinning of MoS2 by thermal annealing. Nanoscale 2013;5:8904-8.

[176] Liu YL, Nan HY, Wu X, et al. Layer-by-Layer Thinning of MoS2 by Plasma. Acs Nano 2013;7:4202-9.

[177] Xiao SQ, Xiao P, Zhang XC, et al. Atomic-layer soft plasma etching of MoS2. Sci Rep 2016;6:19945.

[178] Chen M, Nam H, Wi S, et al. Multibit Data Storage States Formed in Plasma-Treated MoS2 Transistors. Acs Nano 2014;8:4023-32.

[179] Fang H, Tosun M, Seol G, et al. Degenerate n-Doping of Few-Layer Transition Metal Dichalcogenides by Potassium. Nano Lett 2013;13:1991-5.

[180] Park H-Y, Lim M-H, Jeon J, et al. Wide-Range Controllable n-Doping of Molybdenum Disulfide (MoS2) through Thermal and Optical Activation. Acs Nano 2015;9:2368-76.

[181] Nipane A, Karmakar D, Kaushik N, et al. Few-Layer MoS2 p-Type Devices Enabled by Selective Doping Using Low Energy Phosphorus Implantation. Acs Nano 2016;10:2128-37.

[182] Liu XC, Qu DS, Ryu JJ, et al. P-Type Polar Transition of Chemically Doped Multilayer MoS2 Transistor. Adv Mater 2016;28:2345-51.

[183] Azcatl A, Qin X, Prakash A, et al. Covalent Nitrogen Doping and Compressive Strain in MoS2 by Remote N-2 Plasma Exposure. Nano Lett 2016;16:5437-43.

[184] Zhao P, Kiriya D, Azcatl A, et al. Air Stable p-Doping of WSe2 by Covalent Functionalization. Acs Nano 2014;8:10808-14.

[185] Tosun M, Chuang S, Fang H, et al. High-Gain Inverters Based on WSe2 Complementary Field-Effect Transistors. Acs Nano 2014;8:4948-53.

[186] Yu J, Lee C-H, Bouilly D, et al. Patterning Superatom Dopants on Transition Metal Dichalcogenides. Nano Lett 2016;16:3385-9.

[187] Late DJ, Liu B, Matte H, et al. Rapid Characterization of Ultrathin Layers of Chalcogenides on SiO2/Si Substrates. Adv Funct Mater 2012;22:1894-905.

[188] Shim J, Oh A, Kang DH, et al. High-Performance 2D Rhenium Disulfide (ReS2) Transistors and Photodetectors by Oxygen Plasma Treatment. Adv Mater 2016;28:6985-92.

[189] Chen M, Wi S, Nam H, et al. Effects of MoS2 thickness and air humidity on transport characteristics of plasma-doped MoS2 field-effect transistors. J Vac Sci Technol B 2014;32:06FF2.

[190] 2017, Silicon Etch Processing for MEMS Devices, memsstar Ltd, http://memsstar.com/products-services/mems/xenon-difluouride-xef2-etching/

[191] Ionescu R, George A, Ruiz I, et al. Oxygen etching of thick MoS2 films. Chem Commun 2014;50:11226-9.

[192] Mead DG, Irwin JC. Long wavelength optic phonons in WSe_2. Can J Phys 1977;55:379-82.

[193] Pradhan NR, Rhodes D, Memaran S, et al. Hall and field-effect mobilities in few layered p-WSe2 field-effect transistors. Sci Rep 2015;5:8979.

[194] Luo X, Zhao Y, Zhang J, et al. Effects of lower symmetry and dimensionality on Raman spectra in two-dimensional WSe2. Phys Rev B 2013;88:195313.

[195] Yamamoto M, Nakaharai S, Ueno K, et al. Self-Limiting Oxides on WSe2 as Controlled Surface Acceptors and Low-Resistance Hole Contacts. Nano Lett 2016;16:2720-7.

[196] Jones AM, Yu H, Ghimire NJ, et al. Optical generation of excitonic valley coherence in monolayer WSe2. Nat Nanotechnol 2013;8:634-8.

[197] Mak KF, He KL, Lee C, et al. Tightly bound trions in monolayer MoS2. Nat Mater 2013;12:207-11.

[198] Yu YF, Yu YL, Xu C, et al. Engineering Substrate Interactions for High Luminescence Efficiency of Transition-Metal Dichalcogenide Monolayers. Adv Funct Mater 2016;26:4733-9.

[199] Mouri S, Miyauchi Y, Matsuda K. Tunable Photoluminescence of Monolayer MoS2 via Chemical Doping. Nano Lett 2013;13:5944-8.

[200] Nan H, Wang Z, Wang W, et al. Strong Photoluminescence Enhancement of MoS2 through Defect Engineering and Oxygen Bonding. Acs Nano 2014;8:5738-45.

[201] Kang N, Paudel HP, Leuenberger MN, et al. Photoluminescence Quenching in Single-Layer MoS2 via Oxygen Plasma Treatment. J Phys Chem C 2014;118:21258-63.

[202] Salitra G, Hodes G, Klein E, et al. Highly oriented WSe2 thin films prepared by selenization of evaporated WO3. Thin Solid Films 1994;245:180-5.

[203] Huang J, Yang L, Liu D, et al. Large-area synthesis of monolayer WSe(2) on a SiO(2)/Si substrate and its device applications. Nanoscale 2015;7:4193-8.

[204] Kojima I, Kurahashi M. Application of asymmetrical Gaussian/Lorentzian mixed function for X-ray photoelectron curve synthesis. J Electron Spectrosc Relat Phenom 1987;42:177-81.

[205] Campbell PM, Tarasov A, Joiner CA, et al. Field-effect transistors based on wafer-scale, highly uniform few-layer p-type WSe2. Nanoscale 2016;8:2268-76.

[206] Zhuiykov S, Kats E, Carey B, et al. Proton intercalated two-dimensional WO3 nano-flakes with enhanced charge-carrier mobility at room temperature. Nanoscale 2014;6:15029-36.

[207] Bestwick TD, Oehrlein GS. Tungsten etching mechanisms in CF4/O2 reactive ion etching plasmas. J Appl Phys 1989;66:5034.

[208] Peignon MC, Cardinaud C, Turban G. A Kinetic-Study of Reactive Ion Etching of Tungsten in Sf6/O2 Rf Plasmas. J Electrochem Soc 1993;140:505-12.

[209] Petri R, Henry D, Francou JM, et al. Tungsten etching in low‐pressure SF6 plasma: Influence of the surface temperature. J Appl Phys 1994;75:1171-8.

[210] Bensaoula A, Grossman E, Ignatiev A. Etching of Tungsten with XeF2: an X-Ray Photoelectron-Spectroscopy Study. J Appl Phys 1987;62:4587-90.

[211] Turban G, Coulon JF, Mutsukura N. A Mechanistic Study of SF6 Reactive Ion Etching of Tungsten. Thin Solid Films 1989;176:289-308.

[212] Mutsukura N, Turban G. Reactive Ion Etching of Tungsten in Sf6-N2 Plasma. J Electrochem Soc 1990;137:225-9.

[213] Verdonck P, Swart J, Brasseur G, et al. Analysis of the Etching Mechanisms of Tungsten in Fluorine-Containing Plasmas. J Electrochem Soc 1995;142:1971-6.

[214] Verdonck P, Brasseur G, Swart J. Reactive Ion Etching and Plasma-Etching of Tungsten. Microelectron Eng 1993;21:329-32.

[215] Marchon B, Carrazza J, Heinemann H, et al. TPD and XPS studies of O2, CO2, and H2O adsorption on clean polycrystalline graphite. Carbon 1988;26:507-14.

[216] Speight JG, Lange's handbook of chemistry, McGraw-Hill, Inc., New York, NY, USA, 2005.

[217] Haynes WM, CRC handbook of chemistry and physics, CRC press, Boca Raton, FL, USA, 2014.

[218] Tan C, Liu Y, Chou H, et al. Laser-assisted oxidation of multi-layer tungsten diselenide nanosheets. Appl Phys Lett 2016;108:083112.

[219] Li Z, Yang SS, Dhall R, et al. Layer Control of WSe2 via Selective Surface Layer Oxidation. Acs Nano 2016;10:6836-42.

[220] Wagner CD, Davis LE, Zeller MV, et al. Empirical atomic sensitivity factors for quantitative analysis by electron spectroscopy for chemical analysis. Surf Interface Anal 1981;3:211-25.

[221] Meyer J, Kröger M, Hamwi S, et al. Charge generation layers comprising transition metal-oxide/organic interfaces: Electronic structure and charge generation mechanism. Appl Phys Lett 2010;96:193302.

[222] Chen M, Nam H, Wi S, et al. Stable few-layer MoS2 rectifying diodes formed by plasma-assisted doping. Appl Phys Lett 2013;103:142110.

[223] Addou R, Colombo L, Wallace RM. Surface Defects on Natural MoS2. ACS Appl Mater Interfaces 2015;7:11921-9.

[224] Ebert P. Nano-scale properties of defects in compound semiconductor surfaces. Surf Sci Rep 1999;33:121-303.

[225] Li SL, Komatsu K, Nakaharai S, et al. Thickness Scaling Effect on Interfacial Barrier and Electrical Contact to Two-Dimensional MoS2 Layers. Acs Nano 2014;8:12836-42.

[226] Ji H, Lee G, Joo MK, et al. Thickness-dependent carrier mobility of ambipolar MoTe2: Interplay between interface trap and Coulomb scattering. Appl Phys Lett 2017;110:183501.

[227] Kwon J, Lee JY, Yu YJ, et al. Thickness-dependent Schottky barrier height of MoS2 field-effect transistors. Nanoscale 2017;9:6151-7.

[228] Zheng H, Ou JZ, Strano MS, et al. Nanostructured Tungsten Oxide – Properties, Synthesis, and Applications. Adv Funct Mater 2011;21:2175-96.

[229] Chang M-T, Chou L-J, Chueh Y-L, et al. Nitrogen-Doped Tungsten Oxide Nanowires: Low-Temperature Synthesis on Si, and Electrical, Optical, and Field-Emission Properties. Small 2007;3:658-64.

[230] Chuang S, Battaglia C, Azcatl A, et al. MoS2 P-type Transistors and Diodes Enabled by High Work Function MoOx Contacts. Nano Lett 2014;14:1337-42.

[231] Greiner MT, Chai L, Helander MG, et al. Metal/Metal-Oxide Interfaces: How Metal Contacts Affect the Work Function and Band Structure of MoO3. Adv Funct Mater 2013;23:215-26.

[232] Greiner MT, Chai L, Helander MG, et al. Transition Metal Oxide Work Functions: The Influence of Cation Oxidation State and Oxygen Vacancies. Adv Funct Mater 2012;22:4557-68.

[233] Wang S, Zhao W, Giustiniano F, et al. Effect of oxygen and ozone on p-type doping of ultra-thin WSe2 and MoSe2 field effect transistors. Phys Chem Chem Phys 2016;18:4304-9.

[234] Battaglia C, Yin X, Zheng M, et al. Hole Selective MoOx Contact for Silicon Solar Cells. Nano Lett 2014;14:967-71.

[235] Meyer J, Shu A, Kroger M, et al. Effect of contamination on the electronic structure and hole-injection properties of MoO3/organic semiconductor interfaces. Appl Phys Lett 2010;96:133308.

[236] Irfan, Ding HJ, Gao YL, et al. Energy level evolution of air and oxygen exposed molybdenum trioxide films. Appl Phys Lett 2010;96:243307.

[237] Du Y, Liu H, Neal AT, et al. Molecular Doping of Multilayer MoS2 Field-Effect Transistors: Reduction in Sheet and Contact Resistances. IEEE Electron Device Lett 2013;34:1328-30.

[238] Pei JJ, Gai X, Yang J, et al. Producing air-stable monolayers of phosphorene and their defect engineering. Nat Comms 2016;7:10450.

[239] Bunch JS, van der Zande AM, Verbridge SS, et al. Electromechanical resonators from graphene sheets. Science 2007;315:490-3.

[240] Choi K, Lee YT, Min S-W, et al. Direct imprinting of MoS_2 flakes on a patterned gate for nanosheet transistors. Journal of Materials Chemistry C 2013;1:7803-7.

[241] Castellanos-Gomez A, Buscema M, Molenaar R, et al. Deterministic transfer of two-dimensional materials by all-dry viscoelastic stamping. 2D Mater 2014;1:011002.

[242] Yang R, Zheng X, Wang Z, et al. Multilayer MoS_2 transistors enabled by a facile dry-transfer technique and thermal annealing. J Vac Sci Technol B 2014;32:061203.

[243] Li B, He Y, Lei S, et al. Scalable Transfer of Suspended Two-Dimensional Single Crystals. Nano Lett 2015;15:5089-97.

[244] Qiu D, Lee DU, Park CS, et al. Transport properties of unrestricted carriers in bridge-channel MoS_2 field-effect transistors. Nanoscale 2015;7:17556-62.

[245] van der Zande AM, Barton RA, Alden JS, et al. Large-Scale Arrays of Single-Layer Graphene Resonators. Nano Lett 2010;10:4869-73.

[246] Bao W, Liu G, Zhao Z, et al. Lithography-free fabrication of high quality substrate-supported and freestanding graphene devices. Nano Res 2010;3:98-102.

[247] Wang F, Stepanov P, Gray M, et al. Annealing and transport studies of suspended molybdenum disulfide devices. Nanotechnology 2015;26:105709.

[248] Wang F, Stepanov P, Gray M, et al. Ionic Liquid Gating of Suspended MoS_2 Field Effect Transistor Devices. Nano Lett 2015;15:5284-8.

[249] Huang Y, Sutter E, Shi NN, et al. Reliable Exfoliation of Large-Area High-Quality Flakes of Graphene and Other Two-Dimensional Materials. Acs Nano 2015;9:10612-20.

[250] Komaragiri U, Begley MR, Simmonds JG. The Mechanical Response of Freestanding Circular Elastic Films Under Point and Pressure Loads. J Appl Mech 2005;72:203-12.

[251] Begley MR, Mackin TJ. Spherical indentation of freestanding circular thin films in the membrane regime. J Mech Phys Solids 2004;52:2005-23.

[252] Kang J, Tongay S, Zhou J, et al. Band offsets and heterostructures of two-dimensional semiconductors. Appl Phys Lett 2013;102:012111.

[253] Zeng F, Zhang W-B, Tang B-Y. Electronic structures and elastic properties of monolayer and bilayer transition metal dichalcogenidesMX2(M= Mo, W;X= O, S, Se, Te): A comparative first-principles study. Chin Phys B 2015;24:097103.

[254] Kertesz M, Hoffmann R. Octahedral vs. trigonal-prismatic coordination and clustering in transition-metal dichalcogenides. J Am Chem Soc 1984;106:3453-60.

[255] Sekaric L, Parpia JM, Craighead HG, et al. Nanomechanical resonant structures in nanocrystalline diamond. Appl Phys Lett 2002;81:4455-7.

[256] Yang YT, Ekinci KL, Huang XMH, et al. Monocrystalline silicon carbide nanoelectromechanical systems. Appl Phys Lett 2001;78:162-4.

[257] Agarwal MK, Wani PA. Growth conditions and crystal structure parameters of layer compounds in the series Mo1−xWxSe2. Mater Res Bull 1979;14:825-30.

[258] Johnston ID, McCluskey DK, Tan CKL, et al. Mechanical characterization of bulk Sylgard 184 for microfluidics and microengineering. J Micromech Microeng 2014;24:035017.

[259] Bhatia NM, Nachbar W. Finite indentation of an elastic membrane by a spherical indenter. Int J Nonlin Mech 1968;3:307-24.

[260] Ando T, Sato K, Shikida M, et al. Orientation-dependent fracture strain in single-crystal silicon beams under uniaxial tensile conditions. Micromechatronics and Human Science, 1997. Proceedings of the 1997 International Symposium on 1997;55-60.

[261] Wang SW, Medina H, Hong KB, et al. Thermally Strained Band Gap Engineering of Transition-Metal Dichalcogenide Bilayers with Enhanced Light Matter Interaction toward Excellent Photodetectors. Acs Nano 2017;11:8768-76.

[262] Ahn GH, Amani M, Rasool H, et al. Strain-engineered growth of two-dimensional materials. Nat Comms 2017;8.

[263] Zhao HQ, Mao X, Zhou DH, et al. Bandgap modulation of MoS2 monolayer by thermal annealing and quick cooling. Nanoscale 2016;8:18995-9003.

[264] Zhang Q, Chang Z, Xu G, et al. Strain Relaxation of Monolayer WS2

on Plastic Substrate. Adv Funct Mater 2016;26:8707-14.

[265] Lloyd D, Liu XH, Christopher JW, et al. Band Gap Engineering with Ultralarge Biaxial Strains in Suspended Monolayer MoS2. Nano Lett 2016;16:5836-41.

[266] Tsai MY, Tarasov A, Hesabi ZR, et al. Flexible MoS2 Field-Effect Transistors for Gate-Tunable Piezoresistive Strain Sensors. ACS Appl Mater Interfaces 2015;7:12850-5.

[267] Chuang HJ, Tan XB, Ghimire NJ, et al. High Mobility WSe2 p- and n-Type Field-Effect Transistors Contacted by Highly Doped Graphene for Low-Resistance Contacts. Nano Lett 2014;14:3594-601.

[268] Das S, Dubey M, Roelofs A. High gain, low noise, fully complementary logic inverter based on bi-layer WSe2 field effect transistors. Appl Phys Lett 2014;105.

[269] Zhu ZY, Cheng YC, Schwingenschlögl U. Giant spin-orbit-induced spin splitting in two-dimensional transition-metal dichalcogenide semiconductors. Phys Rev B 2011;84:153402.

[270] Reyes-Retana JA, Cervantes-Sodi F. Spin-orbital effects in metal-dichalcogenide semiconducting monolayers. Sci Rep 2016;6:24093.

[271] Roldán R, Silva-Guillén JA, López-Sancho MP, et al. Electronic properties of single-layer and multilayer transition metal dichalcogenides MX2 (M = Mo, W and X = S, Se). Ann Phys-Berlin 2014;526:347-57.

[272] Hsu WT, Lu LS, Wang D, et al. Evidence of indirect gap in monolayer WSe2. Nat Comms 2017;8:929.

[273] Zibouche N, Kuc A, Musfeldt J, et al. Transition-metal dichalcogenides for spintronic applications. Ann Phys-Berlin 2014;526:395-401.

[274] Ataca C, Ciraci S. Functionalization of Single-Layer MoS2 Honeycomb Structures. J Phys Chem C 2011;115:13303-11.

[275] Yue Q, Kang J, Shao Z, et al. Mechanical and electronic properties of monolayer MoS2 under elastic strain. Phys Lett A 2012;376:1166-70.

[276] Fei R, Yang L. Strain-Engineering the Anisotropic Electrical Conductance of Few-Layer Black Phosphorus. Nano Lett 2014;14:2884-9.

[277] Shin BG, Han GH, Yun SJ, et al. Indirect Bandgap Puddles in Monolayer MoS2 by Substrate-Induced Local Strain. Adv Mater 2016;28:9378-+.

[278] Amin B, Kaloni TP, Schwingenschloegl U. Strain engineering of WS2, WSe2, and WTe2. Rsc Advances 2014;4:34561-5.

[279] Madsen GKH, Singh DJ. BoltzTraP. A code for calculating band-structure dependent quantities. Comput Phys Commun 2006;175:67-71.

[280] Bardeen J, Shockley W. Deformation Potentials and Mobilities in Non-Polar Crystals. Physical Review 1950;80:72-80.

[281] Yun WS, Lee JD. Two-dimensional semiconductors ZrNCl and HfNCl: Stability, electric transport, and thermoelectric properties. Sci Rep 2017;7:17330.

[282] Dimple, Jena N, De Sarkar A. Compressive strain induced enhancement in thermoelectric-power-factor in monolayer MoS2 nanosheet. J Phys Condens Matter 2017;29:225501.

[283] Zhang J, Liu X, Wen Y, et al. Titanium Trisulfide Monolayer as a Potential Thermoelectric Material: A First-Principles-Based Boltzmann Transport Study. ACS Appl Mater Interfaces 2017;9:2509-15.

[284] Cai Y, Zhang G, Zhang Y-W. Polarity-Reversed Robust Carrier Mobility in Monolayer MoS2 Nanoribbons. J Am Chem Soc 2014;136:6269-75.

[285] Xi J, Long M, Tang L, et al. First-principles prediction of charge mobility in carbon and organic nanomaterials. Nanoscale 2012;4:4348-69.

[286] Brumme T, Calandra M, Mauri F. Electrochemical doping of few-layer ZrNCl from first principles: Electronic and structural properties in field-effect configuration. Phys Rev B 2014;89:245406.

[287] Gibbs ZM, Ricci F, Li G, et al. Effective mass and Fermi surface complexity factor from ab initio band structure calculations. npj Computational Materials 2017;3.

[288] Fallahazad B, Movva HCP, Kim K, et al. Shubnikov–de Haas Oscillations of High-Mobility Holes in Monolayer and Bilayer WSe2: Landau Level Degeneracy, Effective Mass, and Negative Compressibility. Phys Rev Lett 2016;116:086601.

[289] Liu W, Cao W, Kang J, et al. (Invited) High-Performance Field-Effect-Transistors on Monolayer-WSe2. ECS Trans 2013;58:281-5.

[290] Das S, Prakash A, Salazar R, et al. Toward Low-Power Electronics: Tunneling Phenomena in Transition Metal Dichalcogenides_WSe2. Acs Nano 2014;8:1681-9.

[291] Joyce WB, Dixon RW. Analytic approximations for the Fermi energy of an ideal Fermi gas. Appl Phys Lett 1977;31:354-6.